

**SYNTHESIS AND TESTING OF TIN-OXIDE NANOWIRES FOR FLUX PINNING IN
SUPERCONDUCTORS**

A Thesis

Presented to

the Faculty of the Department of Mechanical Engineering

University of Houston

In Partial Fulfillment

of the Requirements for the Degree

Master of Science

in Mechanical Engineering

by

Rehan Mallick

May 2015

SYNTHESIS AND TESTING OF TIN-OXIDE NANOWIRES FOR FLUX PINNING IN
SUPERCONDUCTORS

Rehan Mallick

Approved:

Chair of the Committee
Venkat Selvamanickam, Professor,
Mechanical Engineering

Committee Members:

Haleh Ardebili, Assistant Professor
Mechanical Engineering

Jiming Bao, Assistant Professor
Electrical & Computer Engineering

Suresh K. Khator, Associate Dean,
Cullen College of Engineering

Pradeep Sharma, Professor and
Department Chair of Mechanical
Engineering

Acknowledgements

I would like to firstly thank Dr. Venkat Selvamanickam for giving me the opportunity to work with him and his great research staff in pioneering work within superconductivity. His support and guidance paved way for this thesis.

This research would also not be possible without the support and advice of many people within the research staff, especially Yao Yao, Xinwei Cai, Haichao Guo, Xiaofen Li, Meysam G., Louis Delgado, Dr. Eduard Galystan, and Dr. Ryu. I also thank my parents for their continual support (and food). I, especially, thank Krista Smith, my girlfriend, for her generous love and support, from start to finish.

I would like to thank my committee members Dr. Haleh Ardebili and Dr. Jiming Bao. And lastly, I would like to thank Trina Johnson, my academic counselor, who made sure I'd be graduating, at all times.

I acknowledge the funding for this research from National Science Foundation (NSF) grant # CMMI-1000162.

SYNTHESIS AND TESTING OF TIN-OXIDE NANOWIRES FOR FLUX PINNING IN
SUPERCONDUCTORS

An Abstract
of a
Thesis

Presented to

the Faculty of the Department of Mechanical Engineering

University of Houston

In Partial Fulfillment

of the Requirements for the Degree

Master of Science

in Mechanical Engineering

by

Rehan Mallick

May 2015

Abstract

In this work, we explore the application of pre-fabricated nanowires in order to pin magnetic flux lines in superconducting films. We have synthesized SnO₂ nanowires in a chemical vapor deposition (CVD) process using Au colloids and sputter coating on flexible CeO₂ substrates. Several growth methods are explored in order to attain full control over nanowire arrays and reduce surface defects. For microstructure modification, we employed ion bombardment which can straighten nanowires as well as remove surface defects. With the optimized growth processes, the results show reductions in surface defects and increases in uniformity and repeatability. Superconducting films were grown on the nanowire-embedded substrates using trifluoroacetate-based metal-organic deposition (TFA-MOD) and metal-organic chemical vapor deposition (MOCVD) systems. Several optimizations were performed on the TFA-MOD growth process. After deposition of the films, decent critical current (I_c) values were attained from samples with pre-fabricated nanowires in the $B \parallel c$ field direction, strongly indicating flux pinning.

Table of Contents

Acknowledgements	iv
Abstract	vi
Table of Contents	vii
List of Figures	x
List of Tables	xvi
Chapter 1: Introduction	1
1.1 Applications of Metal-Oxide Nanowires	1
1.1.1 Gas Sensors	2
1.1.2 Solar Cells	4
1.1.3 Light Emitting Diodes	7
1.2 Flux Pinning in 2 nd Generation Superconducting Tapes.....	8
1.2.1 2 nd Generation High Temperature Superconductors.....	8
1.2.2 Flux Pinning Fundamentals	10
1.2.3 Recent Advances in Flux Pinning.....	14
1.2.4 Research Objective	18
1.3 Chemical Vapor Deposition.....	19
1.3.1 Synthesis of Nanowires by Vapor-Liquid-Solid Mechanism in CVD	23
1.4 Synthesis of REBCO Films.....	26
1.4.1 Trifluoroacetate-based Metal-organic Deposition	26
Chapter 2: Experimental Procedure	30
2.1 Nanowire Synthesis.....	30
2.1.1 Buffer Creation.....	30
2.1.2 Samples Preparation by Colloids.....	30
2.1.3 Samples Preparation by Sputter Coating	32
2.1.4 Chemical Vapor Deposition System	33
2.1.5 Annealing	36
2.2 Ion Bombardment for Nanowire Modification	37
2.3 Metal-organic Deposition	38
2.3.1 Precursor Preparation.....	41
2.3.1.1 Refluxing	42

2.3.1.2	Evaporation.....	42
2.3.2	Coating.....	43
2.3.3	Calcination.....	43
2.3.4	Crystallization.....	44
2.4	Metal-organic Chemical Vapor Deposition.....	46
2.5	Sample Characterization.....	46
2.5.1	Measurement of Superconducting Properties.....	46
2.6	ImageJ.....	49
Chapter 3: Results and Discussion.....		51
3.1	Tin-Oxide Nanowire Fabrication.....	51
3.1.1	Growth Mechanism.....	51
3.2	Colloidal Growth Factors.....	53
3.2.1	Buffer Type.....	53
3.2.2	Temperature.....	54
3.2.3	System Pressure.....	55
3.2.4	Growth Time.....	56
3.3	Defect Reduction Methods.....	58
3.3.1	Venting Gas Flow Rate.....	60
3.3.2	Colloidal Bath.....	61
3.3.3	Spin Coated Colloid Application.....	63
3.3.4	Stirred Colloid Application.....	65
3.3.5	Substrate Annealing.....	66
3.3.6	Carrier Gas Flow Direction and Rate.....	67
3.3.7	Substrate Quenching.....	70
3.4	Colloidal Nanowire Array Uniformity and Repeatability.....	72
3.5	Sputter Coated Nanowire Growth Factors.....	74
3.5.1	Sputtering Time.....	74
3.5.2	Sputter Coat System Pressure.....	76
3.5.3	Growth Time.....	78
3.6	Structure Modification by Ion Bombardment.....	80
3.6.1	Beam Energy.....	81
3.6.2	Tape Speed.....	83

3.6.3	Microstructure Variance between Sputter-Coated & Colloidal-grown Nanowires after Ion Bombardment	86
3.7	TFA-MOD YBCO Thin Film Synthesis	89
3.7.1	Precursor Synthesis.....	89
3.7.2	TFA-MOD YBCO Growth Mechanism.....	90
3.7.3	Growth Factors	94
3.8	Superconducting Properties of YBCO Films with Tin-Oxide Nanowires	105
3.8.1	TFA-MOD Films Embedded with Nanowires.....	105
3.8.2	MOCVD Films Embedded with Nanowires.....	110
Chapter 4: Summary and Future Work.....		116
4.1	Summary	116
4.2	Future Work.....	119
References.....		120

List of Figures

Figure 1: Characteristic Lengths of Mesoscopic Phenomena [1].	1
Figure 2: (left) Crystal Structure of ZnO, (right) Rutile unit cell of SnO ₂ [3] [5]	2
Figure 3: Schematic of Gas Sensors based on NW anodes and Cu cathodes [6] [7]	3
Figure 4: (a) Gas Responses of various diameter ZnO nanowire based sensors. (b) Responsivity of SnO ₂ sensors to CO gas	4
Figure 5: A dye-sensitized solar cell with a coated nanowire array in an electrolyte bath	5
Figure 6: Open circuit voltage values for ZnO nanowire DSCs compared to traditional DSCS.	6
Figure 7: (a) Vertically-aligned ZnO NWs capped with ZnO thin films (b) IV curves of NW device with the additional enhanced IV (dotted-line) due to UV light emission (c) Illuminated equally spaced vertical ZnO nanowires].	8
Figure 8: Comparison of the architectures of the two major 2G HTS tape processing methods: (a) IBAD (b) RABiTS	10
Figure 9: (a) Diagram of pinning sites within a superconducting film [20], (b) Cross-sectional image of various types of pinning sites in YBCO.	13
Figure 10: BZO self-assembled nanorods in columnar formations in (a) plane-view (b) cross-sectional view.	14
Figure 11: J _c values versus applied field for YBCO samples doped with BZO nanorods with the field at (a) H c (b) H ab. (c) The angular dependence of J _c of BZO-doped YBCO thin films compared to pure YBCO.	15
Figure 12: (a) Cross-section of Zr-doped MOCVD-YBCO with BZO nanorods (b) J _c versus applied field values for Zr-doped YBCO compared with pure YBCO.	16
Figure 13: Ideal case for 2G HTS materials.	17
Figure 14: A Schematic of a Low-Pressure Chemical Vapor Deposition System.	21
Figure 15: A schematic diagram of the process steps in a chemical vapor deposition system in the reaction zone.	22

Figure 16: Schematic of the VLS growth of Si nanowires where (a) the liquid alloy of Au and Si is formed above the eutectic temperature. Oversaturation due to continual feeding of Si into the liquid alloy results in nucleation (b) binary phase diagram of the VLS growth.24

Figure 17: Schematic of the intermediate molten zone between the solid phase and liquid phase of a VLS growth nanowire.....25

Figure 18: Standard calcination profile for forming precursor film ranging from 6 hours to over 60 hours.28

Figure 19: Illustration of YBCO growth process during crystallization with SEM cross-sectional images of the various nucleation stages in a TFA-MOD process.....29

Figure 20: A scheme for temperature controlled colloidal seeding process.....32

Figure 21: Photograph of sputter coating system from Hummer™33

Figure 22: Schematic of the NW CVD Growth system with (A) the complete furnace schematic, (B) gas flow within the glass chamber and (C) sample holder design.35

Figure 23: (a) A custom IBAD system used to ion bombard SnO₂ nanowires for re-alignment (b) nanowire substrates prepared with side stripping to protect the surface from any damage after spooling in the reel-to-reel system37

Figure 24: Schematic diagram of the TFA-MOD system.....39

Figure 25: (A) The custom sample holder for MOD 2 and (B) custom sample holder for MOD 1.....40

Figure 26: The IKA rotary evaporator and heated water bath system.....41

Figure 27: Typical spin coating profile for precursor solution during MOD process43

Figure 28: Typical temperature profile for calcination.....44

Figure 29: Typical temperature profile for crystallization including gas environments.....45

Figure 30: (A) Critical temperature testing probe, (B) Critical current testing probe.47

Figure 31: Custom in-field measurement system to measure angular and field dependence of critical current48

Figure 32: (Top-left) Original NW SEM image, (top-right) ImageJ post processing and (center) area analysis on nanowires. (Bottom-left) Original microstructure SEM and (bottom-right) ImageJ image data that has processed the nanoparticle count and area50

Figure 33: SEM images of (left) a completed optimized VLS growth for tin-oxide nanowires with 40 nm colloids on CeO₂ buffer displaying their ‘beak-like’ Au tips, and (right) an unoptimized growth displaying large densities of ‘snake-like’ in-plane nanowires52

Figure 34: Comparison of VLS growth of tin-oxide nanowires on (left) LMO and (right) CeO₂ buffers53

Figure 35: Comparison of nanowire samples grown at (top-left) 550 °C, (top-right) 575 °C, (bottom-left) 630 °C, and (bottom-right) 675 °C.54

Figure 36: Comparison of nanowire growth in pressures of (top-left) 0.40 Torr, (top-right) 0.50 Torr, (bottom-left) 0.53 Torr, and (bottom-right) 0.70 Torr).....56

Figure 37: Comparison of NWs grown for (top-left) 10 min, (top-right) 20 min, and (bottom) 40 min.....57

Figure 38: SEM images highlighting the (top) conglomerated nanoparticles that lead to (center) nanowire clumping defects. (Bottom) The initial seeding procedure resulted in large conglomerations that compromised nanowire array growth59

Figure 39: (Top) Excess tin powder of the substrate after nanowire growth due to gas flow rate and direction. (Bottom) Large density of in-plane nanowires on the substrate surface60

Figure 40: Comparison of nanowires in processes where the system was vented with a gas flow rate of (top-left) 2000 sccm, (top-right) 4000 sccm, and (bottom) 6000 sccm61

Figure 41: Results of heated sonication at 120°F with samples sonicated for (top left) 5 min, (top right) 30 min, (bottom left) 60 min62

Figure 43: Plot of the average and standard deviation of nanoparticle sizes after processing in heated ultrasonic bath63

Figure 43: Results of spin coating with a ramp up time of 15 seconds at (left) 70 RPM, (center) 170 RPM, (right) 300 RPM.64

Figure 44: Results of magnetically stirring the colloidal solution for (top-left) 1 min, (top-right) 5 min, (bottom) 25 min.65

Figure 45: Results of annealing samples after gold colloid deposition at 630°C for 10, 20, and 30 min66

Figure 46: SEM images of the nanowire sample grown in forward gas flow direction showing wide variance in the (top-left) right edge, (top-right) center, and (bottom-left) left edge. (Bottom-right) Excess tin powders were also found near the center of the sample.	68
Figure 47: Results of various reverse gas flow rates with (top-left) 10 sccm, (top-right) 20 sccm, and (bottom) 40 sccm.	69
Figure 48: Comparison of various densities of nanowires (left) with and (right) without air quenching. (Top) 25% NW density, (center) 35% NW density and (bottom) 5% NW density.....	71
Figure 49: Results from optimized conditions versus initial where (top) optimal conditions show improved reliability and repeatability when targeting NW densities around 30-35% as well as (bottom) reduced growth deviations	73
Figure 50: Plot of the effective nanowire density due to colloidal solution amount at various colloid sizes. The optimal conditions allowed for reliable and predictable nanowire growths	74
Figure 51: Plot of the densities of nanowire growths at various sputtering lengths	75
Figure 52: Results of nanowire growth with sputtering times of (top-left) 2 s, (top-right) 4 s, (bottom-left) 6 s, and (bottom-right) 10 s.	76
Figure 53: Results of nanowire growths in samples gold sputter coated at pressures of (top-left) 60 mTorr, (top-right) 80 mTorr, and (bottom) 100 mTorr.....	77
Figure 54: Results of nanowire growth from sputter-coated catalysts at 60 mTorr and 80 mTorr and different growth durations	79
Figure 55: Effective nanowire densities before and after ion-bombardment showing high level of reliability	80
Figure 56: Results from ion-bombardment of samples with nanowires using a forward beam energy of (top-left) 30 W, (top-right) 40 W, and (bottom) 50 W.....	81
Figure 57: A root-like nanowire formation due to ion-bombardment.....	82
Figure 58: XRD scan of (200) CeO ₂ peak showing intensity reduction due to ion-bombardment.....	83
Figure 59: Results of differing nanowire morphologies speeds in colloidal and sputter coated samples after ion bombardment at various tape speeds	84

Figure 60: XRD scans of the (200) CeO ₂ peak of nanowire samples ion bombardment at 40 W showing material damage at various tape speeds	86
Figure 61: Results of ion bombardment at 40 W on sputter coated and colloidal samples at the same starting densities.....	87
Figure 62: Surface cracking due to thick YBCO films caused by lowering the methanol content in the final precursor solution.....	90
Figure 63: Diagram of (left) proper calcination duration leading to no CuO grains in the final crystallized film and (right) over-calcinated film lead to precipitation of large isolated CuO particles [43]. ...	92
Figure 64: SEM image of a crystallized YBCO films on CeO ₂ buffer tapes showing proper c-axis grain growth	93
Figure 65: Critical temperature (T _c) measurements on MOD samples made with differing barium content in the precursor solution where a sample designated with R and L refer to the right and left positions, respectively, on the MOD 2 sample holder	95
Figure 66: Integrated GADDS results obtained from MOD samples with various barium content.....	96
Figure 67: Integrated GADDS and T _c results from MOD samples with differing crystallization times along with a current-voltage curve from the 150 min crystallization duration sample	98
Figure 68: SEM results for MOD samples crystallized for (top-left) 150 min, (top-right) 180 min, (bottom-left) 210 min, and (bottom-right) 270 min.....	99
Figure 69: T _c and transport I _c performance of MOD films processed at various crystallization temperatures. The 755 °C samples consistently yield the best performance	100
Figure 70: SEM scans of samples prepared at crystallization temperatures of (top-left) 750 °C, (top-right) 755 °C, (bottom-left) 765 °C, and (bottom-right) 770 °C	101
Figure 71: (Left) Example plot of humidity sensor measurements from the sample position. (Right) SEM image of cracked sample surface due to insufficient humidity content in the furnace system. .	102
Figure 72: Results of varied humid condition durations of (top-left) 210 min, (top-right) 150 min, and (bottom) 90 min in crystallization of MOD films in MOD 1 at a 750 °C crystallization temperature and 4.2% relative humidity.	103

Figure 73: Scanning hall probe results showing the location of high performing superconducting material in (left) a 4 x 1.2 cm long sample and (right) 1.2 x 1.2 cm square samples.	104
Figure 74: SEM microstructure of (left) calcinated thin film with visible embedded nanowires and (right) crystallized film with visible NWs in the gaps	105
Figure 75: Integrated GADDs results revealing poor YBCO growth on moderately dense nanowire samples in the TFA-MOD process	106
Figure 76: TFA-MOD nanowire embedded YBCO thin film samples compared to reference sample in (top) T_c and (bottom) I_c measurements.....	107
Figure 77: Angular dependence of I_c at 77K of NW and references samples at 1 and 3T (top) and magnetic field dependence of I_c at 77K along the c-axis of NW and references samples (bottom)	108
Figure 78: Angular dependence of I_c at 65K of NW and reference samples at 1 and 3 T.....	109
Figure 79: Magnetic field dependence of I_c along the c-axis of NW and reference samples at 65K.....	110
Figure 80: T_c optimization for bare CeO_2 buffers prior to nanowire testing	111
Figure 81: (Top) GADDs and (bottom) T_c results for moderately dense nanowires samples made by MOCVD compared to the reference indicating degradation in epitaxial YBCO.....	112
Figure 82: T_c and I_c results from low density nanowire samples made MOCVD compared to the	113
Figure 83: Angular and field dependence measurements from nanowire and references samples at 77K	114
Figure 84: Angular and field dependence measurements from nanowire and reference samples at 65K.	115

List of Tables

Table 1: Calcination Gas Flow and Temperature Settings	44
Table 2: Crystallization Gas Flow and Temperature Settings	45
Table 3: Barium Content in TFA-MOD Precursor.....	93

Chapter 1: Introduction

1.1 Applications of Metal-Oxide Nanowires

In recent years, metal-oxide nanowires (NWs) have enjoyed significant scientific interest, enabling numerous technological advances due to their superior functional properties and high surface-to-volume ratios. One-dimensional (1-D) nanostructures exhibit a high level of crystallinity and often have mechanical strength, stiffness and toughness values near the theoretical limits of perfect crystals due to the massive reduction in defects typically found in bulk materials [1]. This enhanced property is attractive for applications in composites and nanoelectromechanical actuators. Additionally, their impressively-small size allows for interaction with several mesoscopic phenomena. Nanowires with diameters 1-100 nm are in the same characteristic lengths of phenomena such as the exciton Bohr radius and Debye screening path (Figure 1) , which are the fundamental drivers of semiconductors and sensors, respectively [1]. Thus, these characteristics of nanowires allow researchers to develop a rich plethora of innovations in applications from solar cells to gas sensors.

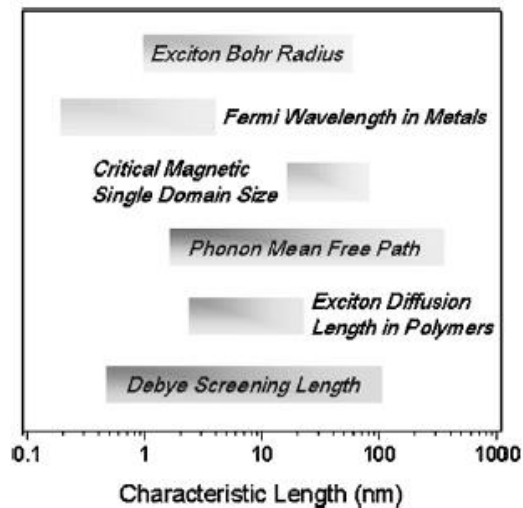


Figure 1: Characteristic Lengths of Mesoscopic Phenomena [1].

1.1.1 Gas Sensors

Among various metal-oxide nanomaterials, zinc oxide (ZnO) and tin oxide (SnO₂) nanowires have generated the greatest deal of attention due to their wide band gaps, thermal stability and processing ease [2]. Zinc oxide has a band gap of 3.37 eV with an exciton binding energy of 60 meV that allows for efficient excitonic emissions at room temperature conditions. The material most commonly grows in a hexagonal non-central symmetric structure with alternating stacking planes of O²⁻ and Zn²⁺ ions along the c-axis with tetrahedral coordination and with lattice parameters of $a = 0.3296$ nm and $c = 0.5206$ nm (Figure 2) [3]. This tetrahedral coordination leads to unique properties such as piezoelectricity and pyroelectricity. Tin oxide is grown in a rutile tetragonal structure with lattice parameters of $a = 0.480$ nm and $c = 0.308$ nm (Figure 2) [3]. The material acts as an n-type semiconductor with a wide band gap of 3.6 eV and has unique properties, including variations in valence energy states and oxygen vacancies, that make it useful in gas sensor, catalyst and electrode material applications [4].

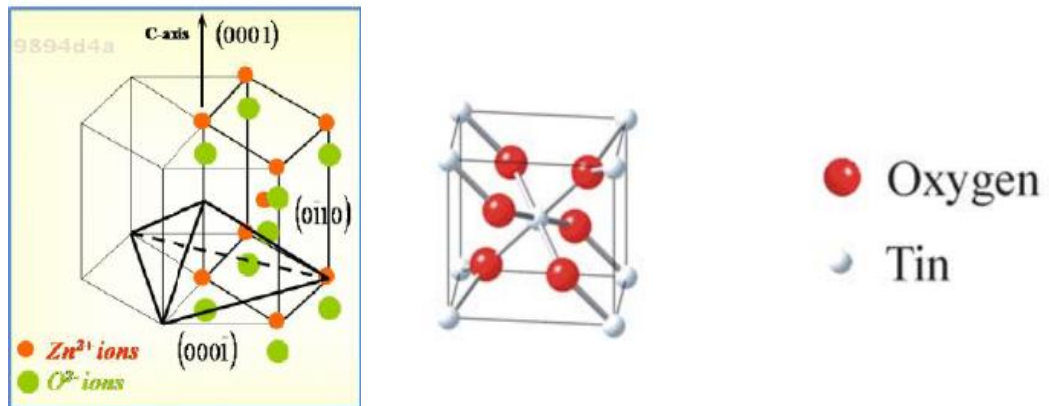


Figure 2: (left) Crystal Structure of ZnO, (right) Rutile unit cell of SnO₂ [3] [5]

Indeed, the most common use of nanowires for the past 20 years is in gas sensing. The thin 1-D nanostructures have excellent surface-to-volume ratios that allow for stronger interaction between ambient gases and the material [3], leading to an inherently high sensitivity

and short response times [1]. The nanowires are designed to trap electrons from absorbed molecules, which in turn, results in a change in conductivity due to band bending by the charged molecules [5]. Figure 3a shows a recent design for fabrication of gas sensors with the nanowires acting as an anode coupled with a copper (Cu) plate cathode [6] [7]. Another common design is

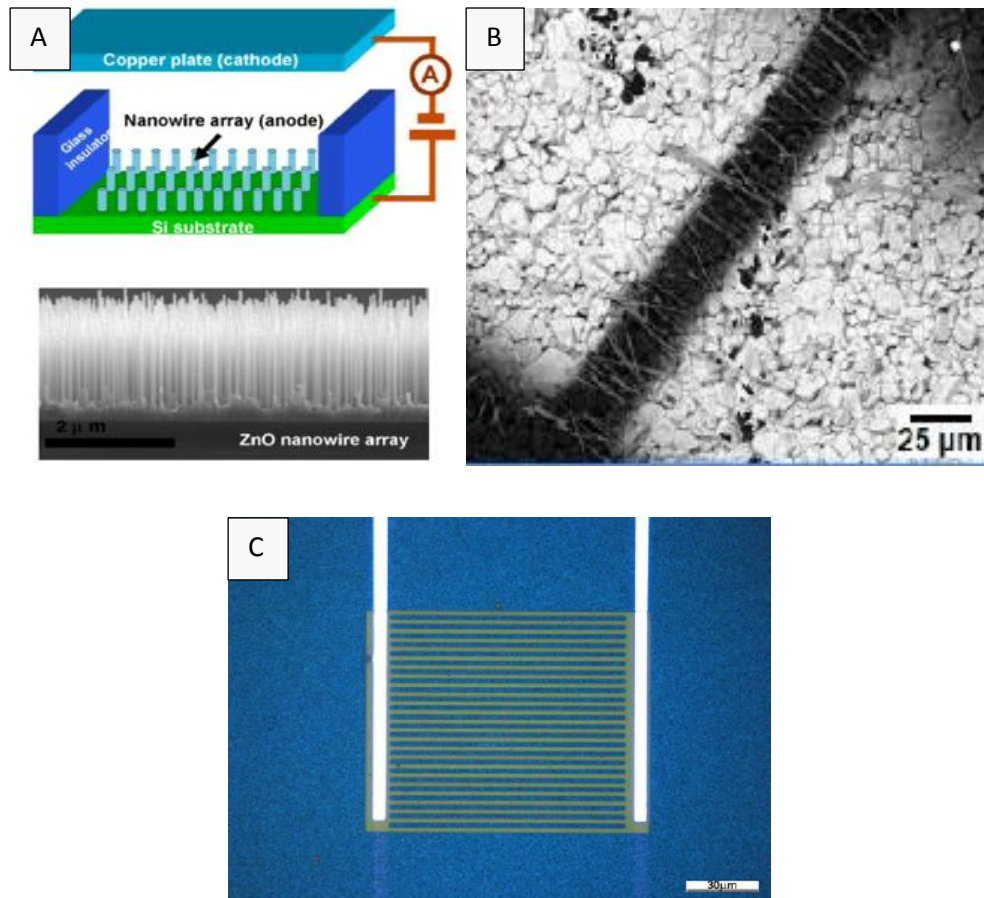


Figure 3: Schematic of Gas Sensors based on NW anodes and Cu cathodes [6] [7]

seen in Fig. 3b: aligned tin oxide nanowires embedded between gold electrodes on silver substrates. The fully fabricated sensor element is shown in Fig. 3c. These nanowire-based gas sensors have proven to be quite effective, showing superiority in both sensitivity and responsivity compared to conventional 2D thin film sensors on the market [7]. Researchers reported creating ZnO sensors with ultra-high gas sensitivities, such as with H₂ at a variety of

temperatures with a detection limit of 20 ppm [8]. Metal-oxide nanowires allow for a wide range of gas detection including NH_3 , isobutene, and CH_4 [8]. Figure 4a shows a the relation of several gasses and the respective sensitivities to those gasses with nanowires of differing sizes.

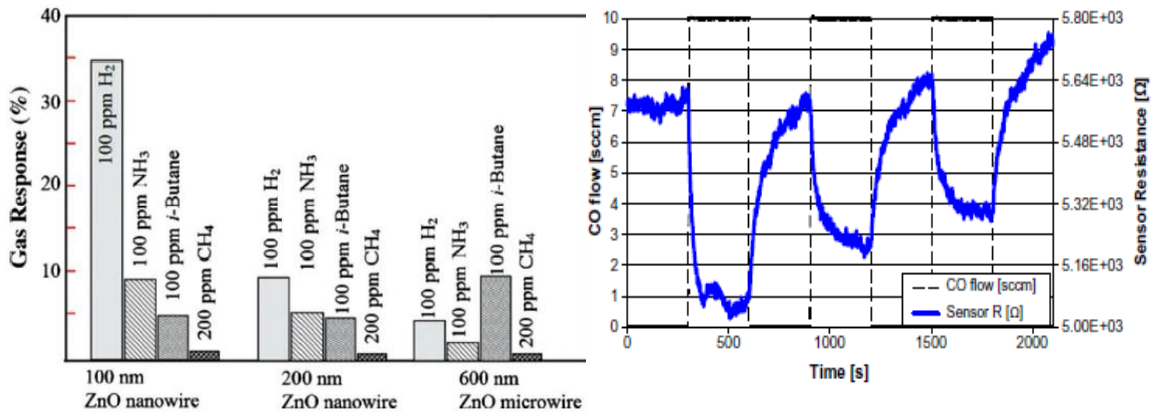


Figure 4: (a) Gas Responses of various diameter ZnO nanowire based sensors. (b) Responsivity of SnO_2 sensors to CO gas [8] [7]

Tin oxide nanowire-based sensors have been created to detect harmful gasses such as CO_x and H_2S with fast responsivity at ultra-low concentrations, while benefiting from the material's resilience in a humid environment [9]. As reported by *Tischner et al.* [7], the fabricated sensors detected CO gas at 4ppm and CH_4 at 3 ppm with excellent response times while operating in humid conditions. *Kuang et al.* [9] report detecting NO_x at 0.5 ppm at 85% relative humidity conditions by using a single SnO_2 nanowire sensor. Figure 4b shows the fast response of the SnO_2 sensors to a pulsed CO flow.

1.1.2 Solar Cells

Though relatively young compared to gas sensors, solar cells are another application where nanowires have played a significant role. Silicon nanowires (Si NWs) are the most widely used in solar cells [10]. *Misra et al.* [10] report creating solar cells by coating randomly-oriented Si NWs acting as p-type semiconductors with an n-type SiH_4 & indium-tin oxide (ITO) layer using plasma enhanced chemical vapor deposition. The solar cells were found to have impressive

short circuit current densities (J_{sc}) of 16.1 mA/cm², and open circuit voltages (V_{oc}) of 0.80V, leading to a fill-factor (FF) of 62.8%. The Si NWs cells achieved high efficiencies of 8.14%, while only using a 100 nm n-type layer [10].

In recent years, nanowires have also found applications within dye-sensitized solar cells (DSCs). DSCs are a unique form of low-cost organic solar cells that employ a mesoporous layer of metal-oxides between conducting glass layers [11]. The metal-oxide layer is chemisorbed by a ruthenium-based dye that acts as a light sensitizer and is sealed within an electrolyte bath, typically iodide. For typical operation under sunlight (AM1.5), the dye enters an excited state, emitting an electron that travels to the anode to complete the circuit. The iodide electrolyte replenishes the dye with an electron to prevent decomposition of the dye [12]. Nanowires are attractive for use in DSCs because they offer faster electron mobilities by several orders of magnitude as compared to the traditional spherical nanoparticles used in DSCs [13]. They also offer superior surface areas for better dye loading. Figure 5 shows a typical DSC design with the dye-coated nanowires embedded between a fluorine-doped tin-oxide (FTO) glass and a Pt counter electrode [11].

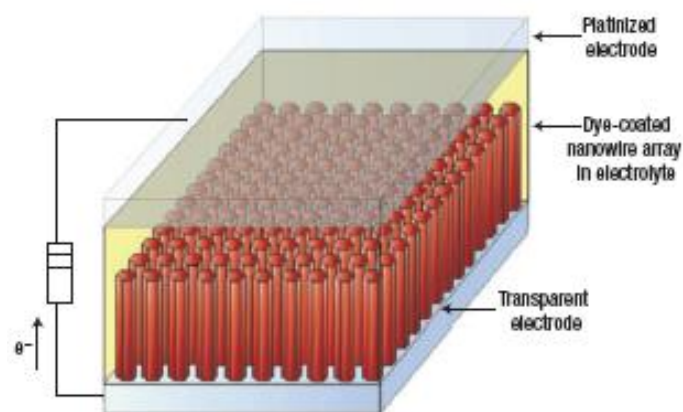


Figure 5: A dye-sensitized solar cell with a coated nanowire array in an electrolyte bath [11]

The nanowire DSCs designs were far more effective in than traditional nanoparticle DSCs. They offer higher J_{sc} and V_{oc} values due to higher carrier/electron lifetimes and improved surface area network structure [11]. For example, *Sreekumaran et al.* [12] report creating a DSC device with SnO_2 nanowires that improves efficiency from 5.7% to 8.6% compared to traditional DSCs with similar thicknesses [12]. Additionally, *Law et al.'s* [11] results reproduced in Fig. 6 shows the improved V_{oc} values for ZnO nanowire DSCs as compared to other metal oxide nanoparticle DSCs. Titanium dioxide (TiO_2) nanowires have been used in double-layer formations to achieve efficiencies up to 9.9% [14]. *Mor et al.* [15] report using TiO_2 in the same ordered design as in Figure 5 to achieve at $J_{sc} = 21.04 \text{ mA/cm}^2$, $V_{oc} = 0.770 \text{ V}$, a fill-factor of 68.4% and an overall efficiency of 11.09%. The same design using traditional nanoparticles achieved an overall efficiency of 6.12%, meaning the nanowire design nearly doubled the efficiency.

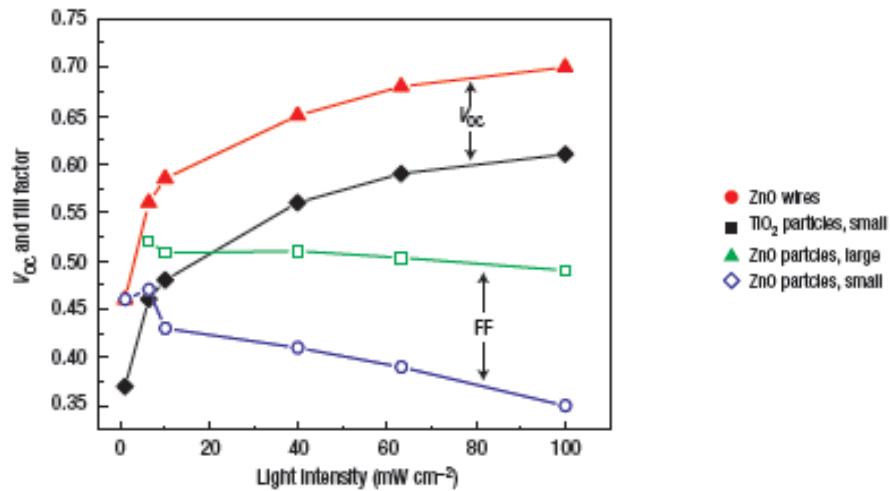


Figure 6: Open circuit voltage values for ZnO nanowire DSCs compared to traditional DSCS [11].

1.1.3 Light Emitting Diodes

Light emitting diodes (LEDs) are another avenue for nanowire applications in recent years. LEDs are similar p-n junction devices compared to solar cells, and generate visible light with the application of electrical power. They function due to excited electrons in the conduction band recombining with holes within the valence band resulting in an emitted energy seen as visible light [16]. Many types of 1D nanostructures have been explored for LED applications including NiO and Ta₂O₅ [16]. Nevertheless, ZnO and SnO₂ remain the most commonly-used NWs due to their wide band gaps (as discussed previously), as well as their ease of synthesis and ability to operate at room temperature [16].

Figure 7a shows a typical NW LED using vertically-aligned n-type ZnO nanowire arrays capped with a ZnO thin film on an Al₂O₃ substrate with p-type GaN interlayers [17]. In this design, the excited electrons originate in the n-type nanowires and are injected into the p-type GaN layer during forward bias [16]. The NWs create good ohmic contacts between n-p interfaces, leading to no current delays. The result is a highly intense blue light in the wavelengths 440nm to 600nm. Examining the IV curves (Figure 7b), the ZnO NW design is also sensitive to UV light emission, where under UV, the current is enhanced, demonstrating their additional usefulness as UV sensors as well. Notably, a similar design using an ordered and equal spaced array of ZnO nanowires at 30 nm diameters was able to achieve nano-LED luminescence [18]. Figure 7c shows the optical image of the ordered ZnO illuminated under a 10V load.

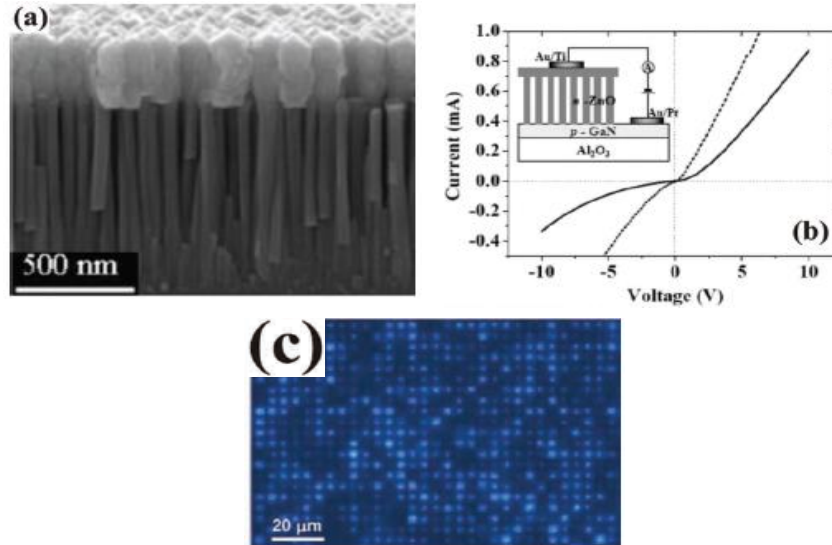


Figure 7: (a) Vertically-aligned ZnO NWs capped with ZnO thin films (b) IV curves of NW device with the additional enhanced IV (dotted-line) due to UV light emission (c) Illuminated equally spaced vertical ZnO nanowires [17, 18].

1.2 Flux Pinning in 2nd Generation Superconducting Tapes

The objective for this research is to develop pioneering work on applying metal-oxide nanowires to 2nd generation high temperature superconductors (2G HTS). While there has been a wealth of exploration in applications of NWs within devices such as semiconductors, nanowire applications in superconductivity is still emerging and relatively scarce. Nevertheless, there is a high potential for applications of pre-fabricated NWs to improve performances of 2G HTS materials due to the phenomena of flux pinning.

1.2.1 2nd Generation High Temperature Superconductors

For nearly two decades, 1st generation high temperature superconductors (1G HTS) i.e. Bi-Sr-Ca-Cu-O (BSCCO) were used in applications such as power cables and motors. However, 1G HTS suffers from high material production costs due to heavy silver use, making it expensive for viable commercial applications. Furthermore, it exhibits poor performance in magnetic

fields, especially losing its supercurrent ability in magnetic fields at liquid nitrogen temperatures [19]. For this reason, an alternative 2G HTS design was developed by epitaxial growth of superconducting films on flexible thin metal substrates. These new materials require significantly less silver [19] and employ $\text{YBa}_2\text{Cu}_3\text{O}_{7-x}$ (YBCO) or other similar cuprate oxides. The standard chemical formula for 2G HTS superconductors is $(\text{RE})\text{Ba}_2\text{Cu}_3\text{O}_{7-x}$ where RE is a rare earth or rare-earth mixture such as Y, Gd, Sm, Dy, etc [20]. Moreover, the (RE)BCO based superconductors offer the advantage of superior current-carrying ability in a magnetic field [19].

Currently, 2G HTS wires are developed using two major technologies: rolling assisted biaxially textured substrates (RABiTS) and ion-beam assisted deposition (IBAD) [20]. The development of these two major technologies ushered in the manufacturing of hundreds of meters long superconducting tapes that remarkably approach single-crystalline substrate performance with the added benefit of flexibility [19]. Figure 8 shows the architecture of the two methods. In RABiTS, a cube texture is formed in the substrate through a sequence of rolling and heat treatment steps. (RE)BCO film is deposited by a solution-based method such as metal-organic deposition (MOD). In IBAD, a commercial alloy is used for the substrate with a crystalline texture created by IBAD MgO. The (RE)BCO film is typically deposited on to the surface using a top-down process such as metal-organic chemical vapor deposition (MOCVD), pulsed laser deposition (PLD) or co-evaporation as well as MOD. In both cases of RABiTS and IBAD, a buffer stack is created between the superconducting film and the substrate to prevent diffusion of substrate elements and impart biaxial texture to the superconductor. Additionally, both are covered with silver for protection and electrical contacts and then copper for cryostability.

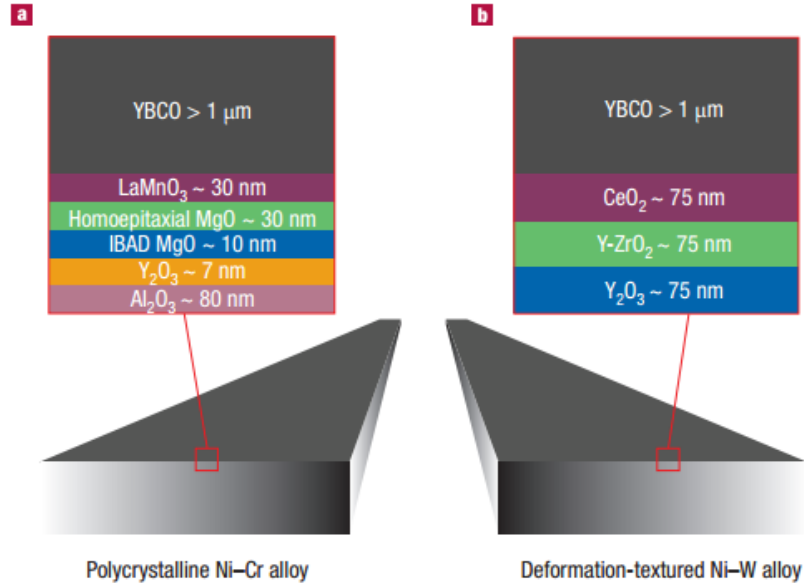


Figure 8: Comparison of the architectures of the two major 2G HTS tape processing methods: (a) IBAD (b) RABiTS [19]

1.2.2 Flux Pinning Fundamentals

Vast improvements have been made in 2G HTS materials in the past two decades; however, the cost - performance metric still needs further improvement. Originally, there was a drastic decrease of current-carrying performance due to the existence of increased misorientations between adjacent superconducting grains in the polycrystalline material. This weak-link effect has been nearly eliminated by technologies such as IBAD and RABiTS, which enables epitaxial growth in near single-crystalline thin films. With the weak-link effects significantly mitigated, the primary objective of present-day research is to increase the current-carrying ability of the superconductors while reducing degradation in magnetic fields that is present in several applications.

Flux creep is a thermally-activated movement of magnetic flux lines that destroy the superconducting state within Type II superconductors, such as YBCO. In Type I superconductors, which are purely metallic low-temperature superconductors, there are two surface energy

states: superconducting and normal. The formation of normal regions within Type I superconductors is unfavorable since it increases the already positive surface energy. Therefore, all superconductivity is destroyed when the applied field increases to a critical field H_c value. However, in Type II superconductors the surface energy is negative, making the formation of the normal state more favorable [20]. With no applied current or external field, there is no magnetic field in the superconductor. Applying a current in Type II superconductors generates a self-magnetic field, whereupon reaching a lower critical field value H_{c1} , the superconductor is penetrated by tubular structures called flux lines or vortices. Each flux line carries a single unit of magnetic flux, or the flux quantum ϕ_0 [20]. With an increased applied field, the superconductor reaches the upper critical field value H_{c2} , where superconductivity is destroyed. Between H_{c1} and H_{c2} , the superconductor exists in a mixed state in which the vortices start to form tubular normal-state cores due to the flux lines that repel each other to form an array of fluxons. In the mixed state, the superconducting state and the small normal state co-exist. The application of the current and magnetic field generates a lateral Lorentz force ($J \times \phi_0$) on the flux lines, causing them to move. This moving vortex tends to dissipate energy and causes the superconducting material to enter a normal state. This will limit the maximum sustainable current value before the material reaches the upper critical field H_{c2} , leading to a poorer performing superconductor.

Luckily, due to specific defects found within the superconductor, there also exists a 'pinning' force that counteracts the Lorentz force. A flux line will have a lower free energy when it is located in the energy well of a defect as compared to the superconducting material [20]. This energy difference acts as an affixing force that 'pins' the movement of the flux line. Nevertheless, when the current is increased in the Type II superconductor, the Lorentz force also increases and eventually overtakes the pinning force at a critical current (I_c). (Note that critical current density (J_c) is simply the I_c value over the cross sectional area). Above this J_c (or I_c) value,

the vortices begin to move and dissipate the material's superconducting state. Thus, in order for the Type II superconductor to sustain a higher critical current, the material needs to exhibit numerous strong pinning forces to counteract the Lorentz forces and pin the magnetic fluxes from the current self-field and an externally applied field.

There are number of defects that can act as pinning centers. One such type of pinning center is the 0-Dimensional point defect which can be an agglomeration of atomic-scale disruptions, as well as voids or interstitials such as impurity atoms. However, single point defects can only interact with one flux line at a time. Another type of pinning center is the 1-D line defect containing columnar defects such as nanorods. They also include misfit dislocations that result when relieving the stress caused by elastic strain from the mismatch between the substrate and (Re)BCO film. They can also be threading dislocations that typically occur throughout the entire film [19]. Line defects have the benefit of interacting with several flux lines depending on the angle of orientation. A third type of pinning center is the 2D planar defects such as stacking faults of extra copper oxide layers in the YBCO layer structure, or twin boundaries at the interfaces of a- and b-axis domains. A planar defect can interact with several flux lines when it is parallel to those lines. Lastly, there are 3D volume pinning centers that include large precipitates and impurity grains. Since volume pinning centers are significantly larger than the flux line's diameter, they can interact with several flux lines at all angles. Figure 9a illustrates the several types of pinning centers and Figure 9b shows a cross-sectional image of pinning sites within YBCO.

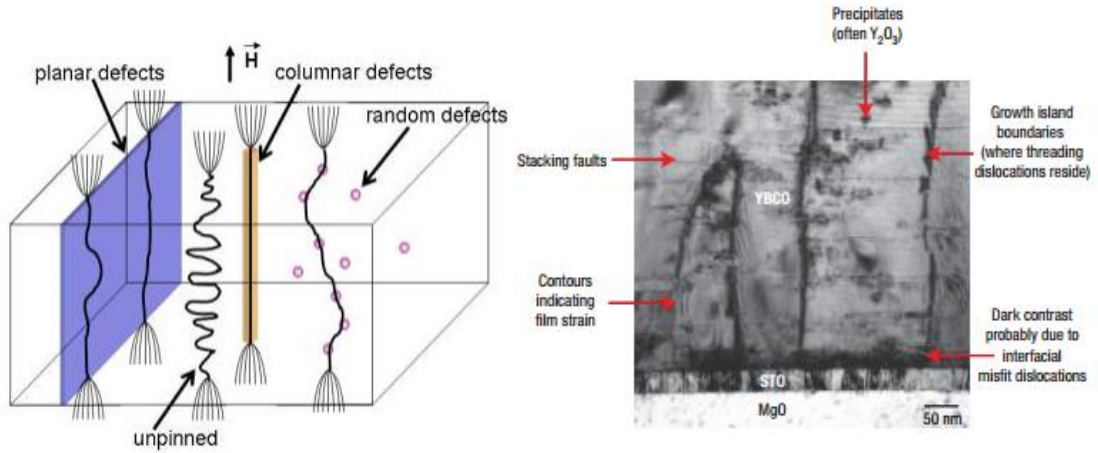


Figure 9: (a) Diagram of pinning sites within a superconducting film [20], (b) Cross-sectional image of various types of pinning sites in YBCO [19].

The bulk of flux pinning research is focused on introducing impurity structures called artificial pinning centers (APCs) into the superconducting film in order to reduce flux-creep. However, the most effective pinning sites are those whose sizes correspond to the vortex's normal core diameter 2ξ , where ξ is the coherence length of the superconductor. The coherence length is described as the distance between the electrons in a Cooper pair, where ξ_0 is the coherence length at absolute zero temperature, as given here,

$$\xi(T) = \xi_0 \frac{1}{\sqrt{1 - \frac{T}{T_c}}}. \quad Eq. 1$$

At an operating condition of 77K, the typical size of the vortex's core is 2-3 nm. In this size range, nanoscale structures are the most efficient current-day solution to optimizing flux pinning. Since they do not consume unnecessary volume fractions within superconductors, nanostructures allow for improved flux pinning, without sacrificing superconducting material density.

1.2.3 Recent Advances in Flux Pinning

Significant improvements in introducing pinning centers for 2G HTS have been made in the past decade. In particular, the incorporation of randomly-distributed BaZrO₃ nanoparticles and heteroepitaxial BaZrO₃ nanorods have led to over 5-fold enhancements in J_c values even with an applied field [21]. The BZO nanostructures have a diameter of ~5-6 nm, making them a strong candidate as a pinning center in YBCO at 77K. Additionally, due to the mismatch between BZO and YBCO, the strain generates additional misfit dislocations along the crystallographic c -direction of YBCO [22]. Typically, these nanorods are self-assembled during (RE)BCO pulse-laser deposition (PLD) or MOCVD processes [20] [21]. In *Kang et al.* [21], BZO nanorods for flux pinning were grown by PLD using a YBCO + BZO target created from cold-pressing and sintering the YBCO and BZO powders. Figure 10 shows the plane and cross-sectional view of aligned columnar self-assembled BZO nanostructures in YBCO. The samples were grown to 200 nm thick on a RABiTS buffer.

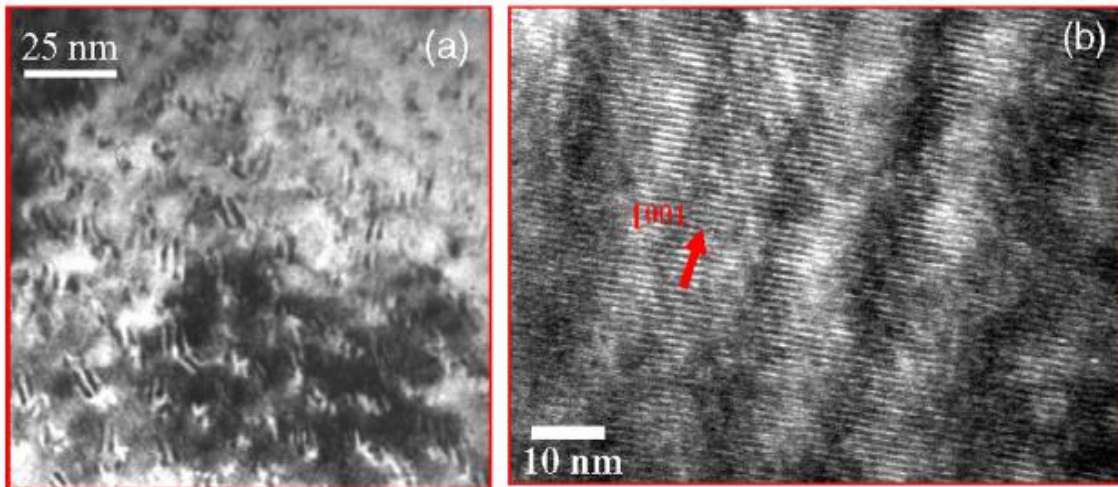


Figure 10: BZO self-assembled nanorods in columnar formations in (a) plane-view (b) cross-sectional view [21].

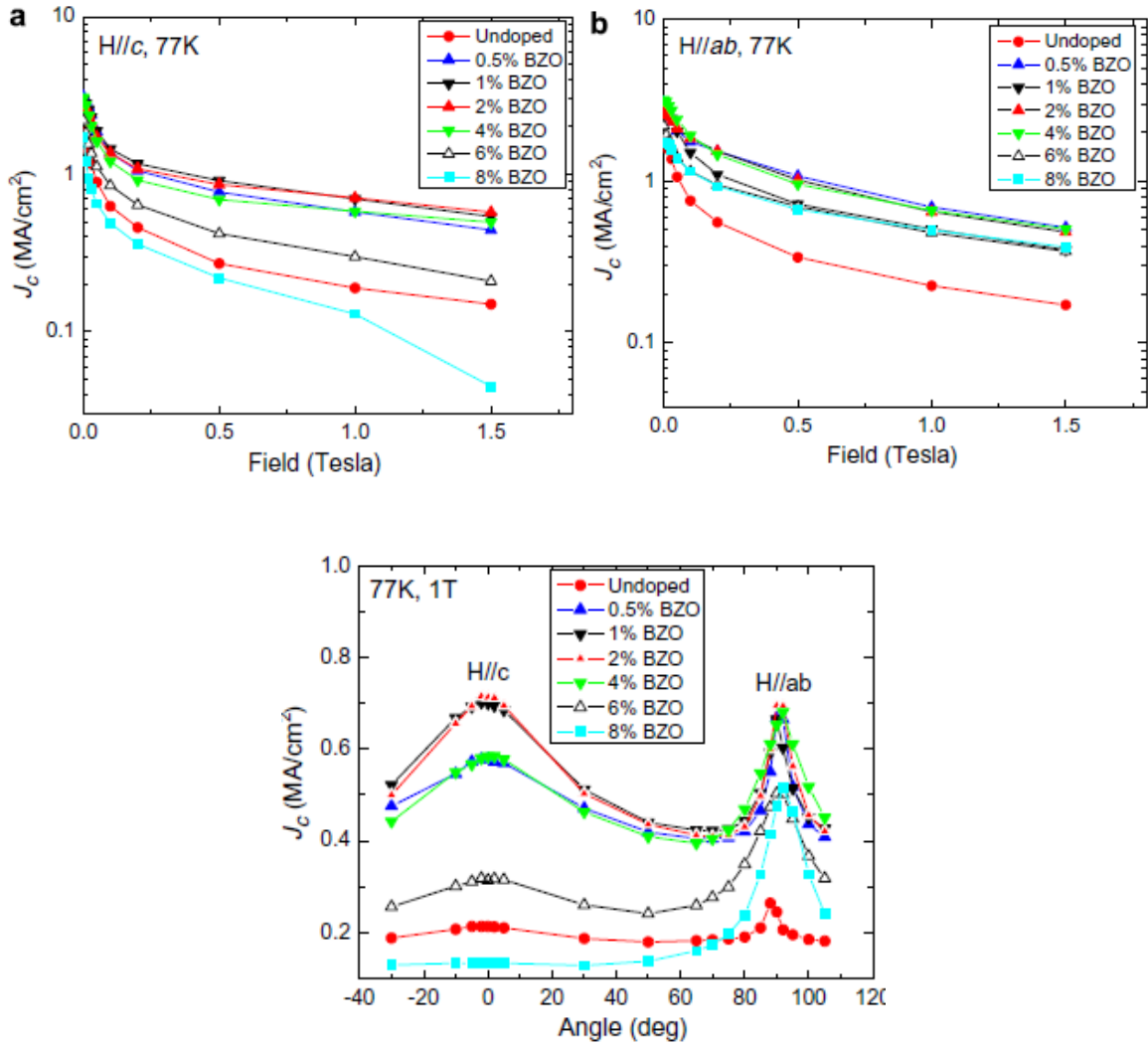


Figure 11: J_c values versus applied field for YBCO samples doped with BZO nanorods with the field at (a) H||c (b) H||ab. (c) The angular dependence of J_c of BZO-doped YBCO thin films compared to pure YBCO [22].

Figure 11a-b shows the J_c values of the BZO nanorods versus an applied field at 77K with applied fields at H||c-axis (0° deg.) and H||a-b axis (90° deg.), respectively. Even in self-field measurements (no applied field), the BZO nanorods resulted in a strong J_c enhancement with a 58% increase compared to pure YBCO. With an applied field of 1.5 T, the J_c enhancement is nearly five-fold compared to the pure YBCO, with the maximum value reached at an density of 2% vol. BZO. The 8% vol. BZO doped sample was the only sample to show degraded J_c , likely due to the reduced pure YBCO volume-fraction and increased lattice disorder [23]. Figure 11c shows

the angular dependence of J_c of the BZO-doped YBCO compared to pure YBCO; note the especially strong c-axis pinning enhancement.

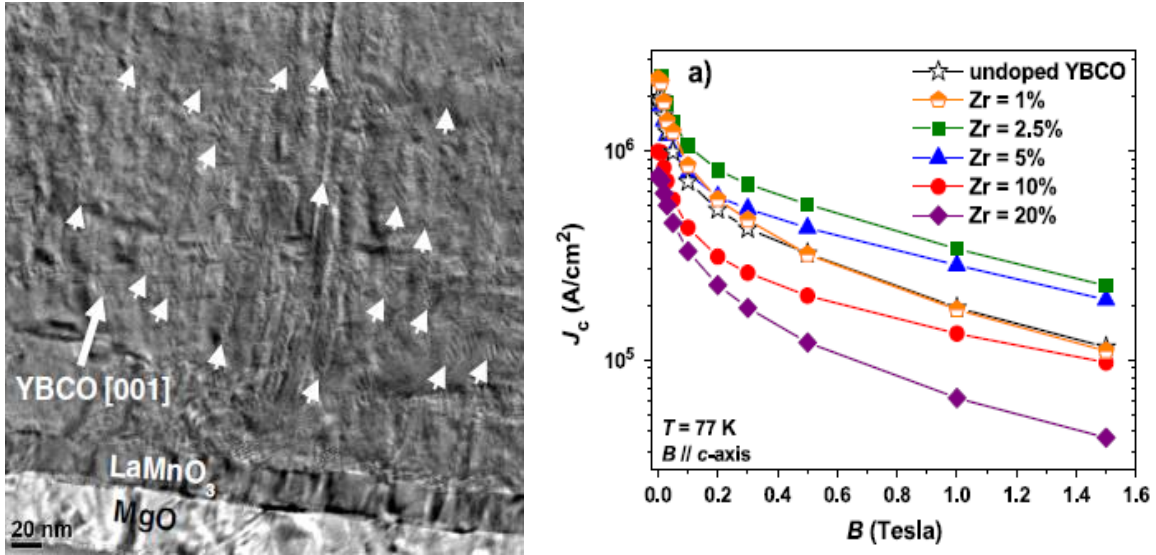


Figure 12: (a) Cross-section of Zr-doped MOCVD-YBCO with BZO nanorods (b) J_c versus applied field values for Zr-doped YBCO compared with pure YBCO [26].

BZO nanorods have been effective in other (RE)BCO superconductors as well. In *Haruta et al.* [24], BZO was grown using PLD with BZO-doped targets in $\text{ErBa}_2\text{Cu}_3\text{O}_y$ (ErBCO) thin films and the J_c was 10 times the pure ErBCO's value. Similarly, in *Ozaki et al.* [25], BZO was grown in $\text{SmBa}_2\text{Cu}_3\text{O}_y$ (SmBCO) thin films resulting in a five-fold increase in J_c . Another method for BZO growth is through Zr precursor doping in a MOCVD [25]. In *Aytug et al.* [26], Zr ranging from 1-20 mol% was added to the precursor solution in an MOCVD process on IBAD-based substrates (LMO/IBAD-MgO). Figure 12a shows the resulting near-aligned columnar self-assembled BZO nanorods in 900 nm thick YBCO films. The Zr-doped YBCO films showed strong pinning enhancements, as well. With a 2.5 mol% of Zr, the J_c was enhanced by over 50% at a field of 1.5T on H || c-axis over the pure YBCO sample. In *Selvamanickam et al.* [27], BZO nanorods in Gd,Y)BCO thin films made by a MOCVD process resulted in a significant increase in I_c by a factor of 2.5 values at 77K at 1T along the c-axis, and similar enhancements persisted to fields up to 8T.

Lately, other types of self-assembled nanorods have also been successfully grown in (RE)BCO films. Tin (Sn), and Niobium (Nb) have been used in PLD to create BaSnO_3 and Ba_2NbO_6 nanorod columns respectively and Titanium (Ti) has been used in MOD precursors to create BaTiO_3 nanorods with reports of similarly enhanced J_c values [28] [29] [30].

Pre-fabricated Metal-Oxide Nanowires for Flux Pinning

It is clear that introducing artificial pinning centers into (RE)BCO film has yielded profoundly significant J_c enhancements in low and high magnetic fields, but further improvements are still needed to fully realize the potential of superconductors. As seen earlier, 2G HTS superconductors have a strong performance dependence on the angle of the applied field with the highest improvement by the pinning centers seen in fields applied along the c-axis. This indicates strong pinning effects due to the c-axis aligned columnar nanorods. However, in several applications, the performance of the superconductor can be limited by the minimum J_c value found between 0° and 90° degrees. Ideally, the (RE)BCO material will exhibit no angular dependence in its performance, as shown in Fig. 13.

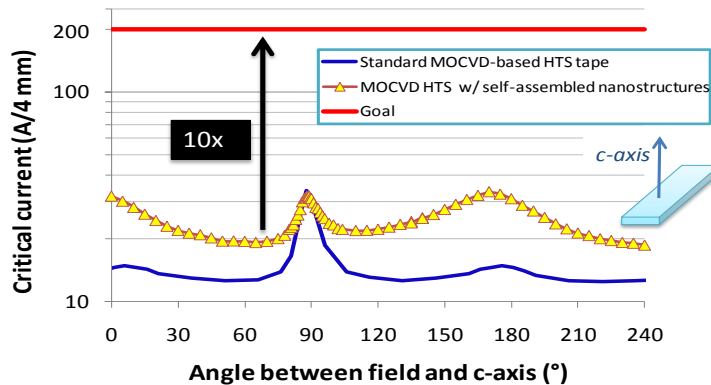


Figure 13: Ideal case for 2G HTS materials [31].

1.2.4 Research Objective

The objective of this project is to conduct exploratory research on creating pre-fabricated metal-oxide nanowires for purposes of flux pinning in YBCO HTS thin films. Metal-oxide NWs bring several potential advantages over typical APCs such as the self-assembled nanorods. Firstly, it is possible to directly control the size, distribution, and growth rate of pre-fabricated NWs, whereas self-assembled nanorods nucleate simultaneously with the REBCO film, and are therefore difficult to control. Furthermore, nanowires can grow in random orientations which should significantly reduce J_c dependence on the angle. Typically, self-assembled nanorods are aligned along the c-axis leading to strong anisotropic pinning along the c-axis. However, since NWs can have a wide angular splay, J_c values should be enhanced at all angles from the c to a/b-axis [32].

In previous work, a variety metal oxide nanowires (ZnO , SnO_2 , TiO_2) have been synthesized on LMO and STO substrates. However, due to chemical instabilities and large lattice mismatches with the substrates, the performance of the superconductors had been largely poor [31]. The NWs grown on the LMO and STO substrates were overwhelmed with undesirable in-plane defects and poor repeatability. For this project, tin-oxide nanowires were chosen to be synthesized with chemical vapor deposition (CVD) mainly on epitaxial cerium-oxide (CeO_2) on IBAD buffered flexible tapes. SnO_2 has a minimum lattice mismatch of roughly 11% with CeO_2 , but has a 21% lattice mismatch with previously researched substrates like LMO, indicating preferable epitaxial relationship with CeO_2 . Additionally, it can withstand temperatures up to 1500°C before breaking down into SnO and O , and has been shown to be chemically inert within the aggressive metal-organic environment of a MOCVD process. It is non-toxic, making it easy to process in normal lab conditions. A variety of parameters in the CVD technique will be optimized to control the size, distribution, density, and repeatability of nanowire synthesis. These

parameters include the temperature, reactive gas partial pressures, source amount, flow rate, and deposition to explore tin-oxide nanowire growth on CeO₂. Post-synthesis methods, such as an ion-bombardment, will be employed to modify the nanostructures.

Two different processes, MOD and MOCVD, will be used to deposit epitaxial HTS YBCO thin films on the NW-based samples, which are discussed further in detail later. The main focus of this project will be the MOD method as it has the advantage of being a solution-based process, where the growth precursor solution is deposited and crystallized on the substrate surface in a 'bottom-up' process. Previous research in MOCVD deposition processes indicated NWs were destroyed or damaged due its 'top-down' vapor process where the precursor vapor reaches the substrate from the top to the bottom [31]. Still, the MOCVD method will be used on the NWs samples with further optimized growing conditions, such as process temperatures and deposition rate, compared to previous work in order to deposit YBCO and reduce NW destruction. The MOCVD method has the advantage of creating thicker and higher critical current samples, with a large area of deposition and significantly higher deposition rates.

1.3 Chemical Vapor Deposition

Chemical vapor deposition (CVD) is an atomistic surface modification technique where solids such as thin coatings or arrays are deposited on a heated substrate via chemical reactions from a gas/vapor phase. There are various types of CVD methods that exist depending on the processing conditions and chemical reactions [33]. The most common methods for conventional thermal activation system include low-pressure CVD (LPCVD), atmospheric pressure (APCVD), ultra-high vacuum (UHCVD), and metal-organic CVD (MOCVD). In the past two decades, CVD processes have evolved to include more complex activation systems such as plasma-enhanced CVD (PECVD) and photochemical-assisted CVD (PACVD). The configuration of a CVD system may take on various forms depending on specific application and desired purity; however, the overall

CVD system design can be segmented into three general components: the reactant input, reaction zone, and reaction by-product removal.

The reactant input system delivers the gaseous reactants to the substrate in the reaction zone. Ambient condition vapor phase reactants are stored in compressed gas cylinders, and reactants that are in liquid or solid state compositions are introduced into the system by heating above their specific boiling or sublimation point [33]. The source temperature and carrier gas flow rate, in principle, control the evaporation rate of the reactants.

The reactor is the central component of all CVD systems with the input of thermal energy as the driving force for most CVD processes [34]. Several reactor types exist, including hot-walled and cold-walled reactors. In a 'hot-wall' reactor, the substrate is housed typically in a quartz tube surrounded by a heating source, such as a tube furnace, where the walls are maintained in an isothermal environment [33]. There is substantial risk in this setup of secondary depositions to occur on the reactor walls, which might break loose and contaminate the growth surface of the substrate. Thus, the reactor walls have to be frequently cleaned. In a cold-wall system, the walls of the reactors are not heated, so negligible deposition occurs on the walls. The substrate is the only part of the system heated up, typically through resistive heating or optical techniques such as tungsten filament lamps [34]. The exhaust system typically involves a vacuum pump for LPCVD processes and scrubbers to neutralize the by-product vapors. The vapors are the unused reactants and by-products from the reaction zone that are exhausted out of the system. Figure 14 shows a schematic of a common LPCVD system.

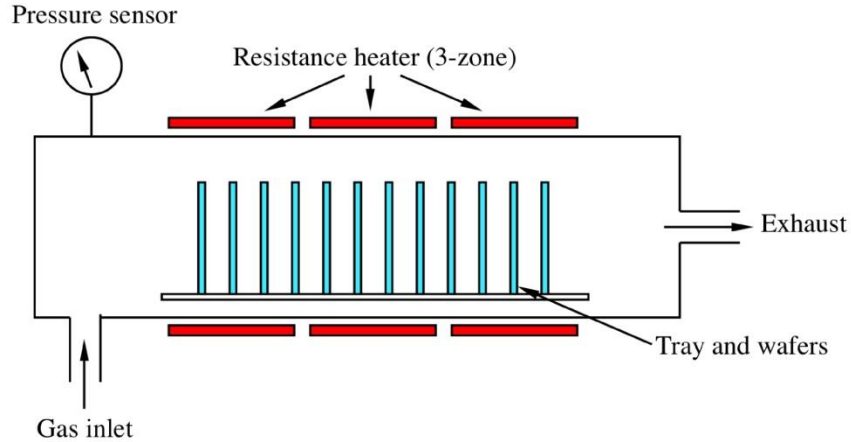
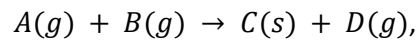


Figure 14: A Schematic of a Low-Pressure Chemical Vapor Deposition System [33].

In a CVD process, deposition occurs via a reaction on the substrate interface,



where $A(g)$ and $B(g)$ are the vapor phase reactants, $C(s)$ is the deposited solid and $D(g)$ is the gaseous by-product. The vapor deposition process occurs as follows [35]: 1-2) The vapor phases generated in the inlet system are transported into the reaction chamber by the carrier gas, 3) diffusion of the reactant gasses occurs through a gaseous boundary layer above the substrate, 4) adsorption of the reactants onto the substrate, 5) single or multi-step heterogeneous chemical reactions occur at the surface of the substrate, 6) lattice incorporation as the deposits further diffuse, and crystallization occurs, 7) desorption of the product gasses from the substrate surface and diffusion away from the surface through any boundary layer that exists, and 8) forced transport of the product gasses from the system. Figure 15 shows a schematic diagram of the steps that occur during the CVD process.

The chemical vapor deposition process is governed by thermodynamics and growth kinetics. For this model, the CVD growth process can be subdivided into two parts: mass transport phenomena and surface reactions [36]. A CVD process is considered to be under mass transport control if the initial or final steps (1 or 8) are the rate limiting or slow steps.

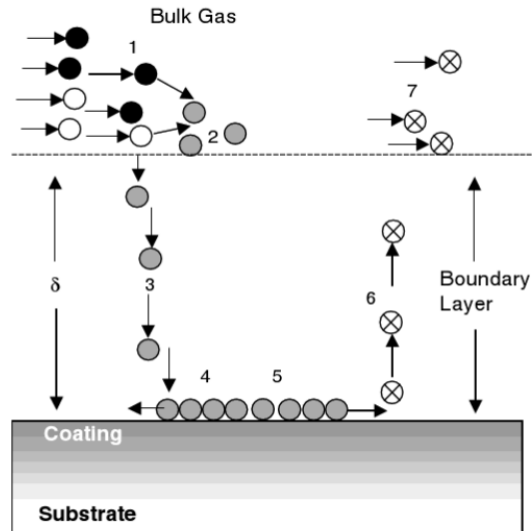


Figure 15: A schematic diagram of the process steps in a chemical vapor deposition system in the reaction zone [35].

The growth reaction would occur faster if the reactant gasses or the by-products were flown into and out of the system at a higher rate. The process is otherwise considered under surface reaction control, which can be further partitioned into diffusion controlled or kinetic controlled. The CVD process is under diffusion control if the diffusion steps of the growth process are rate-limiting or slower. For example, an ample amount of reactant gas is carried into the reaction zone, however, the diffusion of the reactant through the boundary layer is significantly slower. The CVD process is kinetic surface reaction controlled if the adsorption/desorption steps of the growth process are rate-limiting or slower. Generally, at lower temperatures, the deposition rate is controlled by surface reactions. As the temperature is increased, surface reaction dynamics rise exponentially; thus, the mass transport phenomena tend to be a rate-limiting process [33]. The control type of a CVD growth process can typically be determined by experimentally examining the effects of various deposition parameters on the deposition rate of the film. Such parameters include substrate temperature, reactant gas partial pressures, crystallographic orientations, gas flow rates, and surface area.

The CVD method has a number of advantages as a mechanism for deposition and growth [35]. One of the primary advantages is that the growth tends to be quite conformal, which allows films to be grown on elaborately-shaped substrates. In contrast, methods like physical vapor deposition (PVD), such as sputtering, need a line-of-sight to the surface to be coated. CVD also allows for relatively high deposition rates. PVD processes typically also require higher vacuum, whereas CVD normally operates at lower vacuum level. Other advantages include the ability to deposit high-purity films with a wide variety of materials. These advantages have resulted in CVD to become the primary method of synthesizing nanowires.

1.3.1 Synthesis of Nanowires by Vapor-Liquid-Solid Mechanism in CVD

In the past decade, CVD has become the primary method of synthesizing nanowires due to its well-understood growth procedure and reliability. Introduced briefly above, this section explores in detail the growth dynamics of the nanowires on the surface of the substrate. Discovered by Wagner and Ellis in 1965 with the unidirectional growth of semiconductor nanowhiskers, the vapor-liquid-solid (VLS) growth mechanism is perhaps the most widely-applied growth route for 1D nanostructures. Its popularity arises mainly from its ability to successfully synthesize large quantities of nanowires. Other vapor phase growth routes for NWs include vapor-solid (VS), solid-liquid-solid (SLS) and oxide-assisted growth (OAG). The fundamental characteristic of VLS and VLS-based growth is the use of a metal nanocatalyst as a seed for the synthesis of the nanowires. In this process, the metal nanocatalyst is applied to the substrate and heated to above the eutectic temperature of the metal-source system in the presence of a vapor-phase of the desired source material such as Sn, Ge, Ti, etc. Figure 16 shows an example schematic of a VLS process using an Au catalyst and Si source material with the reactions occurring above the eutectic temperature of 363°C.

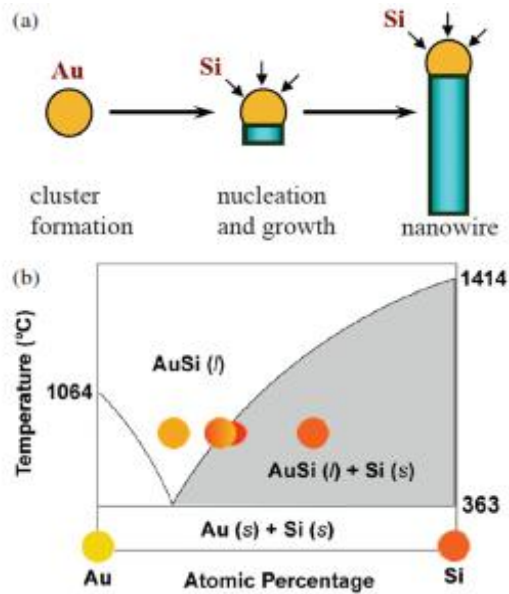


Figure 16: Schematic of the VLS growth of Si nanowires where (a) the liquid alloy of Au and Si is formed above the eutectic temperature. Oversaturation due to continual feeding of Si into the liquid alloy results in nucleation (b) binary phase diagram of the VLS growth [38].

The incoming vapor-phase source materials act as solutes that dissolve into the preferential nucleation site of the metal nanocatalyst, forming a metal-source alloy (such as Au-Si) until the composition reaches the liquidus line for the system [16]. However, if the local concentration of the source material surrounding the particle is thermodynamically higher relative to the content within the nanocatalyst, tiny amounts of vapor-phase source material will continue to dissolve into the alloy. As the reactive vapor is continuously fed into the system, the liquid alloy eventually enters a supersaturated state. This leads to the nucleation of crystalline solid phases on the outside of the liquid alloy, usually on the substrate where it is easiest. There are two competing interfaces during the nanowire growth: the interface between the liquid alloy and the nanowire and the interface between the reactive gas and the exposed nanowire surface [37]. The solid-liquid interface forms the growth interface that allows for continued bonded incorporation into the substrate lattice. Nucleation in this first interface results in axial

VLS growth and elongation since the supersaturated liquid alloy droplet will precipitate the source material in order to retain a stable composition for the binary liquid alloy. As seen in Figure 18a, as the nanowire continues growing, the alloy droplet rises up on top. The axial growth direction from the substrate is dominated by lattice matching between the substrate and the crystalline solid. For common cubic semiconductor nanowires, several types of growth directions have been observed, such as $\langle 110 \rangle$ [38] [39], $\langle 111 \rangle$ [38], and $\langle 112 \rangle$ [40] [37]. However, near the tip, the nanowire itself can shift in growth direction due to presence of a semi-molten zone within the nanowire. Between the solid phase and liquid alloy interface exists a terminal growth zone on the order of several monolayers of atoms in a semi-molten state. Atoms at the solid phase section are capable of moving within the lattice sites, drastically changing the growth direction of the nanowire. For example, in a Si-Al system with a face-centered cubic (FCC) structure, studies indicate that there were several layers of atoms in the quasi-crystalline zone exhibiting a significant amount of atomic movement within lattice sites [41]. Within this certain region, atoms are able to rearrange themselves so that the nanowire may shift in growth direction. In *Howe et al.* [41], the Si-Al nanowire system showed a shift in growth direction from $[111]$ to $[100]$ in the terminal zone with a thickness of 1.9 nm, as shown in Figure 17. The quasi-molten zone is dependent on several factors such as growth temperature, catalyst size and reactive gas pressures.

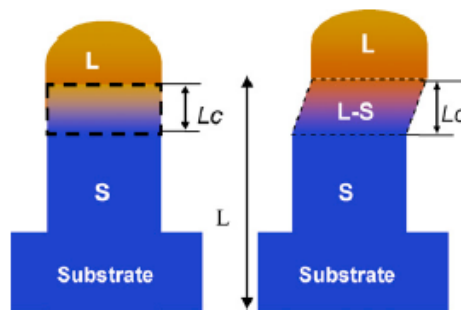


Figure 17: Schematic of the intermediate molten zone between the solid phase and liquid phase of a VLS growth nanowire [40].

In the second interface between the reactive gas and the exposed nanowire surface, dissociative adsorption results in a vapor-solid growth and thickening of the radius of the nanowire. During growth, either mechanism can dominate depending on the growth conditions such as the inert gas flow rate, reactant species, temperature, and pressure. For example, in the Au-Si nanowire system, the use of hydrogen as the inert gas is found to mitigate the radial growth through suppression of adsorption by reactants at the Si surface [37].

1.4 Synthesis of REBCO Films

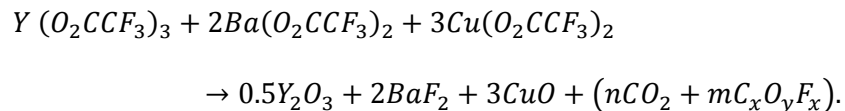
1.4.1 Trifluoroacetate-based Metal-organic Deposition

Metal-organic deposition (MOD) is a solution-based deposition method that has been investigated extensively as a process for YBCO growth due to its many advantages. Specifically, it has lower startup costs compared to alternative processes such as pulsed laser deposition (PLD) systems that require a cost high power UV laser and vacuum system. However, typical MOD chemistries rarely result in high critical current densities (over 1 MA/cm²) because the YBCO growth often suffers from random orientations during the crystallization process as well as degradation in uniformity due to the processes' inability to properly decompose the precursor [42]. With the advent of using trifluoroacetates (TFA) in the precursor, first reported by *Gupta et al.*, in recent years, TFA-based MOD growth has resulted in a much higher critical current density and uniformity compared to a normal MOD process. The TFA-MOD system is fairly simple consisting of an isothermal hot-wall heater, such as a tube furnace, that houses the reaction zone with a gas inlet and outlet. Since the TFA-MOD process requires moist gas, humidifiers such as bubblers are often attached to the inlet. Mass flow meters are used to properly control and maintain specific gas flow rates. The outlet/removal system exhausts the unused reactants and co-products and typically involves scrubbers or bubblers to neutralize any

harmful by-products. The TFA-MOD process itself can be categorized into three fundamental steps: 1) precursor preparation, 2) calcination, and 3) crystallization.

Perhaps the most important of all steps is the initial step of preparing the precursor. Typically, for the preparation of the TFA-MOD coating solution, highly purified (99.99%) raw powders of yttrium acetate, barium acetate, and copper acetate are mixed respectively in a stoichiometric composition ratio of 1:2:3 and dissolved in a mixture of TFA and water [43]. The trifluoroacetic acid helps break down the metal acetates and create fluorinated metals and acetic acid by-product. The mixture is dried by refluxing to a viscous state where it typically takes on a light blue color due to the separated copper cations. However, there are significant amounts of impurities of water and acetic acid due to the TFA. Evaporation and the addition of methanol further refine the solution and remove the impurities. For a highly-purified coating solution, the impurity content is around 0.20-0.40 wt% water and 0.50-1.80 wt% acetic acid; a high purity precursor can lead to higher-performing YBCO thin films [44]. The final pure coating solution is a mixture of fluorinated-based metalorganic salts (Y, Ba, Cu) and methanol that is coated on a substrate.

In the reaction zone, the coated substrate is calcinated in a precursor pyrolysis process that thermally decomposes the metalorganic salts to create a Y-Ba-O-F amorphous matrix with CuO nanocrystallites [45] as seen here,



Generally, the process is executed in an oxidized moist gas environment at temperatures lower than 600°C where the decomposition reduces the thickness of the coated film by up to 50%. Figure 18 shows a typical calcination temperature profile. The long chemical reactions

essential for decomposition are characteristic of organic chemical reactions that break covalent bonds. During the process, the Cu atoms only bind with the free oxygen atoms, while the Y and Ba preferentially form a matrix with the oxygen or fluorine atoms [46]. Carbon content is normally expelled from the film and any remaining carbon molecules are impurities. Under-calcination leads to incomplete decomposition; however, over-calcination results in an over-precipitation of CuO nanocrystallites that degrade YBCO performance after crystallization [43].

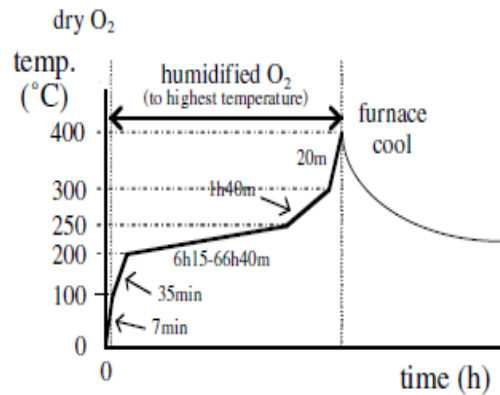
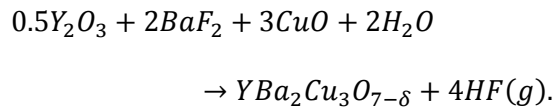


Figure 18: Standard calcination profile for forming precursor film ranging from 6 hours to over 60 hours [45].

The final step is a crystallization process that leads to the nucleation and growth of YBCO, where the calcinated material is re-heated and annealed. The conversion process from the decomposed precursor film to YBCO thin film occurs according to the chemical formula, as seen here,



The initial stage involves reaching temperatures above 650 °C, where the calcinated thin film will form a quasi-liquid interface [46]. The fluorine atoms in BaF₂ molecules will freely attach to the flowing humidified gas in the boundary layer where this reaction will result in hydrogen fluoride (HF) gas. At surface of the substrate, the quasi-liquid interface will begin to

nucleate $YBa_2Cu_3O_{7-\delta}$ which will continue to grow from bottom to top. This growth process, along with a typical growth curve, is seen in Figure 19. Precise control of factors that determine reaction rates is required to nucleate epitaxial YBCO on an oxide buffer and subsequently, the growth of highly textured YBCO. Such factors include ramping rates, temperature duration, gas flow rates, and relative humidity.

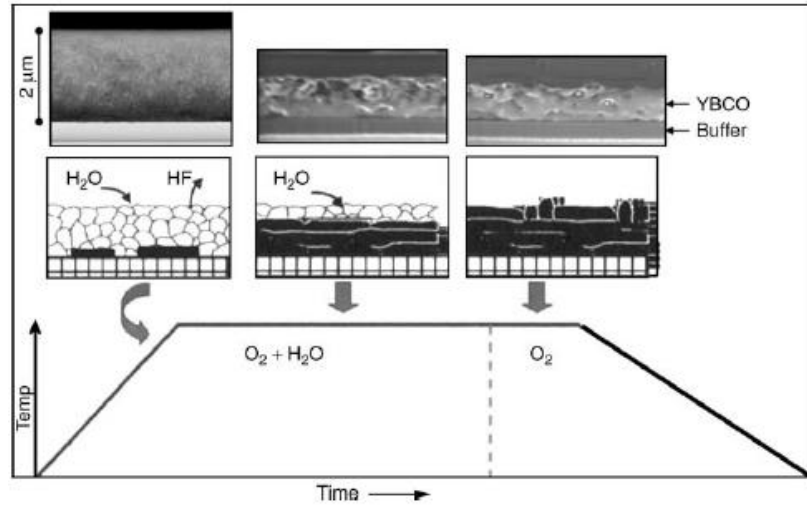


Figure 19: Illustration of YBCO growth process during crystallization with SEM cross-sectional images of the various nucleation stages in a TFA-MOD process [42].

Chapter 2: Experimental Procedure

This chapter explores in detail the experimental procedures performed to synthesize nanowires by chemical vapor deposition, for structural modification by ion-bombardment, YBCO thin film deposition via MOD, and measurement of superconducting properties. Several characterization methods such as scanning electron microscopy (SEM) and x-ray diffraction (XRD) are then used to investigate the properties of the nanowires and YBCO thin films.

2.1 Nanowire Synthesis

2.1.1 Buffer Creation

The flexible IBAD-MgO tape substrates for nanowire synthesis and YBCO deposition were provided by *SuperPower Inc.* The heteroepitaxial layers of LMO and CeO₂ layers were deposited on top of the MgO using a magnetron sputter system by collaborators within our group. The buffer tapes were cut in to 7 cm x1.2 cm sizes to fit into the CVD and MOD systems. Two types of catalyst deposition methods were used to prepare the substrates: colloidal catalyst deposition and sputter coated catalyst deposition.

2.1.2 Samples Preparation by Colloids

One of the methods for depositing catalysts onto the flexible substrates is through gold colloidal solutions. To attach the gold on the substrate, a positively-charged electrolyte layer was coated on the substrate to attract the negatively-charged gold colloids. The electrolyte layer used was a 0.1% concentration poly-L-lysine solution from Ted Pella. Approximately, 0.20 mL of poly-L-lysine solution was evenly deposited on to the substrate using a pipette for 60 seconds and the washed off with deionized (DI) water. Inert gas such as argon was used to immediately blow dry the surface. After the substrate was fully dried, gold colloidal solution was evenly applied to the substrate and left to settle for 5 minutes. After 5 minutes, the substrate was again washed in DI water and blow dried with argon gas. The final step of this method involves

incubating the sample on a hot-plate (PC-400, *Corning Inc.*) at approximately 60 °C for one hour so as to remove any excess water molecules and to let the colloids assume a stable configuration on the substrate. Note, differing amounts of colloidal solution from 0.10 mL to 0.50 mL were added to the substrate in order to achieve differing nanowire densities. Additionally, varying sizes of colloids from 20nm to 50nm diameters were also used to examine the effects of nanowire morphologies. These details are further discussed in the results of Chapter 3.

In order to reduce conglomeration of the colloids on the surface of the substrate, several alternative methods were explored. One such method was a simple modification of stirring the colloidal solution with a magnetic stirrer for 5, 15, and 25 minutes and then depositing on the substrate surface using a pipette for 5 minutes. An additional method for colloidal deposition was via a colloidal bath. Others have successfully seeded nanoparticles by submerging substrates in a heated colloidal bath after ultrasonication as seen in Figure 20 [47]. The increased temperature and ultrasonication proved beneficial in drastically reducing conglomeration of colloids. Our work used a modified system in which the colloidal solution was prepared in a heated water-bath ultrasonicator using a capped centrifuge tube as a container. After coating the substrate with poly-L-lysine as discussed above, a substrate was inserted into a centrifuge tube for 5, 30, and 60 min in a water-bath temperature of 50 °C. The sample was then washed with DI water, blow dried with argon, and incubated on a hot-plate for an hour.

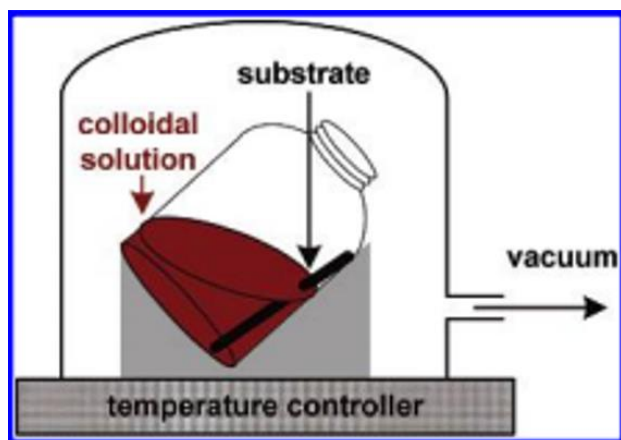


Figure 20: A scheme for temperature controlled colloidal seeding process [47].

A more standard approach was also taken by spin coating the colloidal solution on to the substrates at varying RPM levels in order to investigate any improvements in conglomeration densities. After depositing poly-L-lysine, the substrate was spin-coated (SCS 6800, *Specialty Coating systems, Inc.*) with speeds ranging from 70 to 500 RPM and 0.15 mL of colloidal solution. The resulting sample was again washed, dried and then incubated on a hot-plate.

2.1.3 Samples Preparation by Sputter Coating

The second method for catalyst deposition on a substrate is through sputter coating. A sputtering system (Hummer™ 6.2, *Anatech Ltd.*) with a gold-palladium (Au/Pd) target was used to coat the substrate with varying densities and sizes of nanocatalysts. Figure 21 shows a photograph of the sputter system. To operate, the substrate was placed on the stage inside the glass deposition chamber, and the chamber was pumped down by a vacuum pump. After reaching vacuum inside the chamber, argon gas was delivered into the system with a leak valve at. To coat the surface, a high voltage was applied between the target and stage using the control panel. At above 10A, the applied current induces plasma where the accelerated Ar ions hit the Au/Pd target atoms. These atoms after knocked off from the target are deposited as a film on the substrate. To obtain Au/Pd nanoparticles on the substrate, a deposition time of less

than 20s is necessary. It has been experimentally shown that below 20s only nanoparticles form on the surface of the substrate, but above which, thin films are deposited [31]. Other factors such as chamber pressure and voltage value can be adjusted to control the size and density of the Au/Pd nanodots. Generally, higher voltage values produce more Ar ions thereby increasing the sputter rate, whereas adjusting the chamber pressure leads to different nanoparticle diameters. These results are discussed further in Chapter 3.

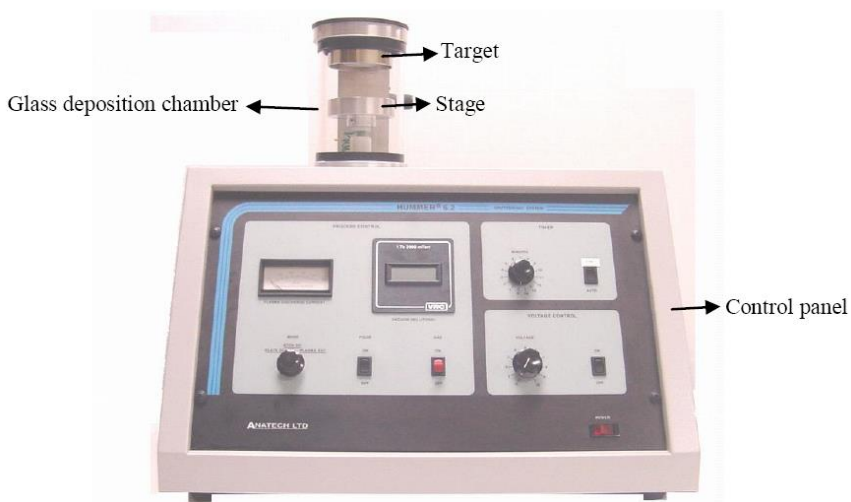


Figure 21: Photograph of sputter coating system from Hummer™.

2.1.4 Chemical Vapor Deposition System

The seeded flexible substrates underwent nanowire growth in a hot-wall CVD system. Figure 22a shows a schematic of the CVD system used to perform all nanowire experiments. The system includes a three-zone tube furnace (STF-55346, Lindberg) with a specially designed quartz tube. The quartz tube had an outer diameter of 2.54 cm, while the inner tube chamber had a 7.62 cm diameter over a 12 cm length. Prior researchers in the group showed if a substrate was forced to lie horizontally, the region of the substrate closest to the source experienced more deposition creating a non-uniform array of nanowires [31]. The specifically designed reactor tube geometry allows the substrate holder to stand up vertically with a 7 cm

substrate, instead of laying horizontally. Additionally, the transitional glass geometry from the 2.54 cm to 7.62 cm chamber was designed so as to allow for the formation of a uniformly parallel reaction gas flow as it entered the chamber. Figure 22b shows a diagram of the glass flow due to the chamber design.

The sample holder design allows it to fold into a vertical position in the chamber and down to less than 2.54 cm during insertion and removal. Figure 22c shows the mobility of substrate holder. The holder is made entirely out of hastelloy to withstand the high temperatures in the tube furnace. At the opposite end of the quartz tube is the source boat made out of a simple alumina crucible which houses the tin powder (99.8%) source material. Both the substrate holder and source boat are attached to 0.3 cm diameter hastelloy rods. These rods are sealed with ultra-Torr vacuum fittings (Swagelok) that allow for horizontal motion under vacuum. The source boat is positioned in the Zone 1 of the furnace, and approximately 20.32 cm in front of the substrate holder. The sample holder is positioned in Zone 2.

During operation, Zone 1 is a higher temperature zone for melting the source powder, while Zones 2 and 3 are held at lower temperatures for proper deposition. The system has two types of gas tanks attached: an Ar gas (carrier gas) tank and a 90% Ar and 10% O₂ mixed gas (venting gas) tank. Both tanks were monitored by mass flow controllers (*MC, Alicat Scientific Inc.*). To control the direction of the gas flow, butterfly valves (*Kurt J. Lesker*) were attached to vacuum fittings on both ends of the tubes.

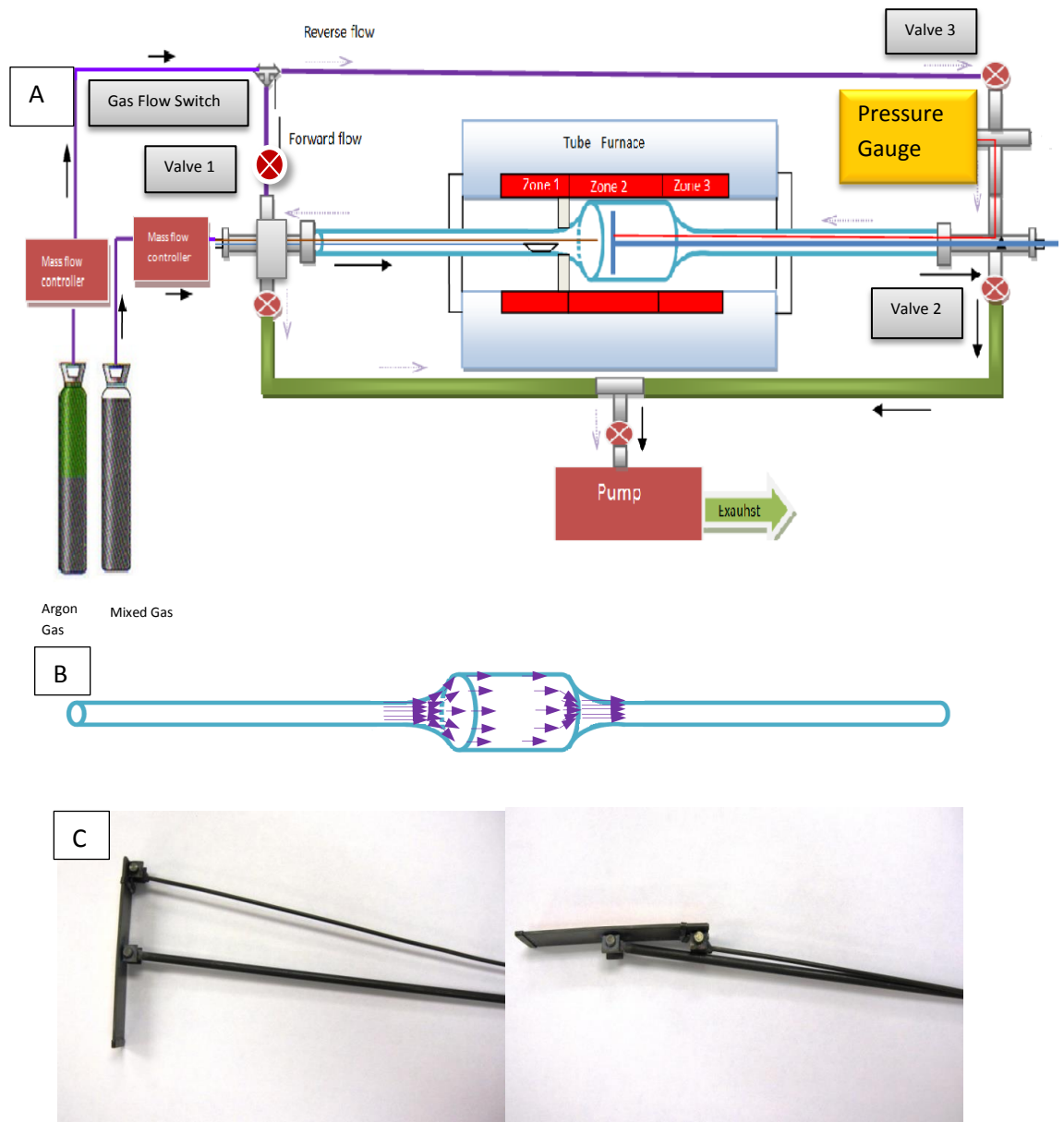


Figure 22: Schematic of the NW CVD Growth system with (A) the complete furnace schematic, (B) gas flow within the glass chamber and (C) sample holder design [31].

As seen in Figure 26a, for forward flow, the carrier gas was flow towards the front of the substrate by turning the gas flow switch towards Valve 1 and opening Valve 1 and Valve 2, but closing Valve 3. For reverse flow, the carrier gas hits the back of the substrate holder by turning the gas flow switch towards Valve 3 opening Valve 1 and Valve 3 but closing Valve 2. A rotary pump (TRIVAC NT, *Oerlikon Leybold Vacuum USA, Inc.*) was used to pump the system down to

vacuum conditions and exhaust out by-products. An additional butterfly valve was used to adjust the pressure down to 8 mTorr where the pressure was read by a digital pressure gauge (KJL275807, Kurt J. Lesker Company).

To synthesize nanowires in the CVD system, the following procedure was carried out:

1. A seeded substrate was carefully mounted on the substrate holder and loaded into the quartz tube. The substrate holder is made sure to be positioned vertically into Zone 2 of the furnace.
2. The alumina boat was filled with tin-oxide powder and positioned in the quartz tube, outside the furnace. This was done to prevent any source material melting before reaching the set point temperature in Zone 1 of the furnace.
3. All connections were sealed and the system was pumped down to 8 mTorr using the butterfly valve. Argon gas was then flown in a reverse direction.
4. The furnace was turned on and adjusted to reach the temperature set points.
5. After the set point temperatures had been reached, the pressure, argon carrier gas flow rate, gas flow direction were adjusted to fit the growth parameters. The alumina boat was then positioned into Zone 1 of the furnace to begin deposition.
6. After deposition time is complete, the pump, carrier gas and furnace were turned off. The system was vented using the mixed venting gas, and the sample holder was unloaded. After the sample holder cooled down, the sample was removed and stored.

2.1.5 Annealing

Prior to deposition, seeded substrates may also undergo an annealing process. In prior experiments and reports [31] [48], annealing has been proven to alleviate conglomeration of gold colloids by melting nearby-packed colloids to form a single large colloid. To anneal

samples, the substrate was loaded onto the sample holder and inserted into the CVD system and annealed at the set point temperature under vacuum conditions. After reaching the annealing time, the system was vented using the venting gas and quenched to room temperature air.

2.2 Ion Bombardment for Nanowire Modification

After deposition and growth of nanowires, modification of the nanowire structures was studied in an ion bombardment system. The main advantage of ion bombardment is that it re-aligns out-of-plane nanowires in the direction of the ion beam which allows for easier deposition of thin films [32]. Secondly, it removes any undesirable in-plane nanowire defects which can block the deposition of thin films. Prior experiments in our group have revealed that irradiating SnO_2 within a focused-ion beam (FIB) system (235, FEI Company) resulted in re-aligned nanowires. However, the FIB area of focus consisted of only a few square micrometers.

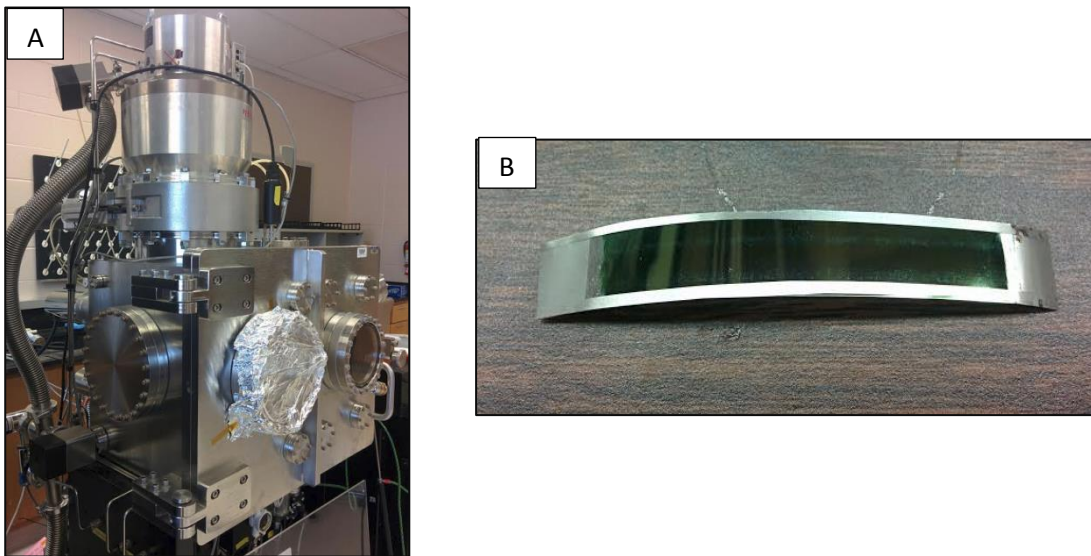


Figure 23: (a) A custom IBAD system used to ion bombard SnO_2 nanowires for re-alignment (b) nanowire substrates prepared with side stripping to protect the surface from any damage after spooling in the reel-to-reel system

A custom reel-to-reel ion-beam assisted deposition (IBAD) system was used to process 7 cm by 1.2 cm substrates. Figure 23a shows a photograph of the IBAD system. The system contained a 7.6 cm Kaufmann ion source aligned at approximately 45° degrees to the substrate surface. The substrates were prepared for the ion bombardment by first side-stripping the substrates with thin hastelloy tape strips using a spot welder. Side-stripping prevent the nanowires from being damaged when spooled onto a reel. The substrates were spot-welded together with more hastelloy tapes and then spooled onto two reels. Figure 23b shows a side-stripped batch of substrates before ion-beam bombardment. The spooled samples were inserted directly into the IBAD system and processed.

Varying specific IBAD system parameters allowed control over the nanowire re-alignment. These parameters include reel speed, ion-beam deposition time, and beam energy. Results of ion beam modification are discussed further in Chapter 3.

2.3 Metal-organic Deposition

As discussed earlier, superconducting thin films of YBCO were deposited using a TFA-MOD process. Figure 24 shows a schematic of the TFA-MOD system. Two separate MOD systems were constructed under the same system design: MOD-1 and MOD-2. MOD-1 used a 2.54 cm diameter quartz tube in which one sample was processed at a time while MOD 2 used a 5.08 cm diameter quartz tube where two samples were processed at a time.

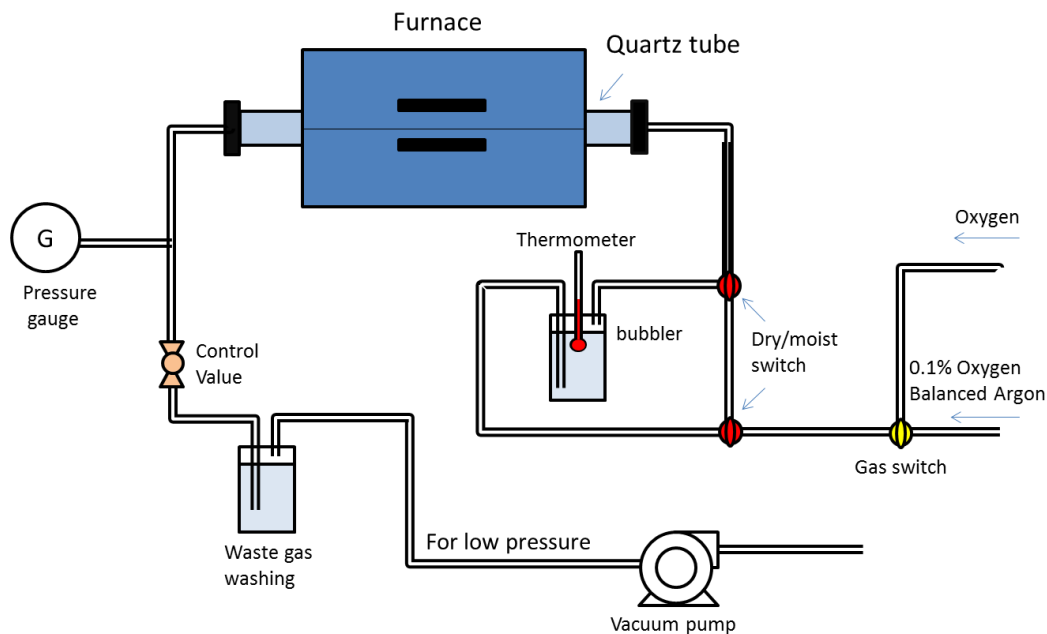


Figure 24: Schematic diagram of the TFA-MOD system.

MOD 1 used a single-zone tube furnace (55322-3, *Lindberg*) with a temperature controller (58114-P, *Lindberg*). The inlet system consisted of two gas tanks, pure oxygen and mixed argon/oxygen gas, that were attached to a gas switch with 0.635 cm diameter tubes. Using similar tubes, the gas switch was attached to a bubbler system and additional gas switches that fed into the inlet of the quartz tube. The bubbler system consisted of a bubbler filled with DI water on a hotplate and a thermometer to monitor the temperature. The bubbler was necessary because it allowed the oxygen and mixed gas to be humidified during calcination and crystallization of the YBCO thin film, as discussed previously in Chapter 1. Multiple gas switches were also implemented to bypass the bubbler system for dry gas conditions. For the reaction system, a sample holder was set in the center of the furnace and the quartz tube was sealed with vacuum fittings (*Swagelok*). Seen in Figure 25a, a custom sample holder was built out of Inconel to withstand high temperatures and harsh chemical environments. In the exhaust system, a 0.635 cm diameter tube was attached to a second bubbler system. This secondary

bubbler system was simply a bubbler filled with DI water that was fed to the exhaust and was used to wash out any toxic by-products in the TFA-MOD process such as HF gas.

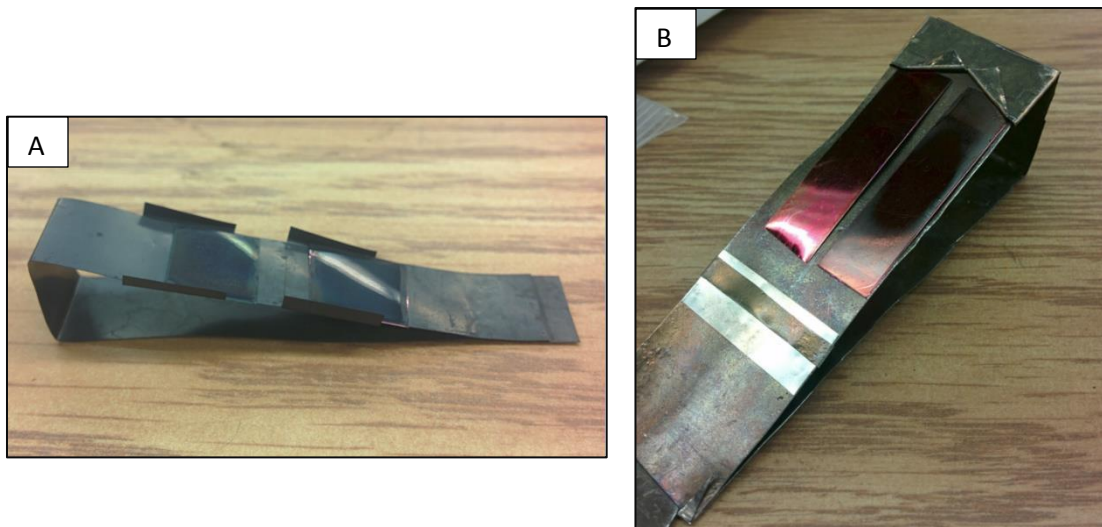


Figure 25: (A) The custom sample holder for MOD 2 and (B) custom sample holder for MOD 1.

MOD 2 used a larger single-zone tube furnace (55342-4, *Lindberg*) to house the bigger 5.08 cm quartz tube with the same temperature controller used in MOD 1. A different sample holder was created to accommodate more substrates into the system. Figure 25b shows the sample holder for MOD 2. All other equipment remained the same.

To examine the humidity content within each of the MOD systems, a temperature and humidity sensor (Si7013, *Silicon Labs*) was used. To capture humidity data, the sensor was placed inside the bubbler, while carefully avoiding the sensor from getting wet. The sensor was also placed at the exact location of the sample holders within the MOD systems with the humidity gas flow activated and furnace turned off to measure the humidity levels exposed to the samples.

2.3.1 Precursor Preparation

To create YBCO thin films with the MOD-TFA process, a properly stable blue precursor solution is necessary. Prior experiments with solutions mixed inside beakers on hot plates proved to create unreliable precursors from batch to batch. Therefore, a low pressure rotary evaporator (RV-8, *Ika*) was used to reflux and synthesize the solution. Figure 26 shows a diagram of the rotary evaporator system.

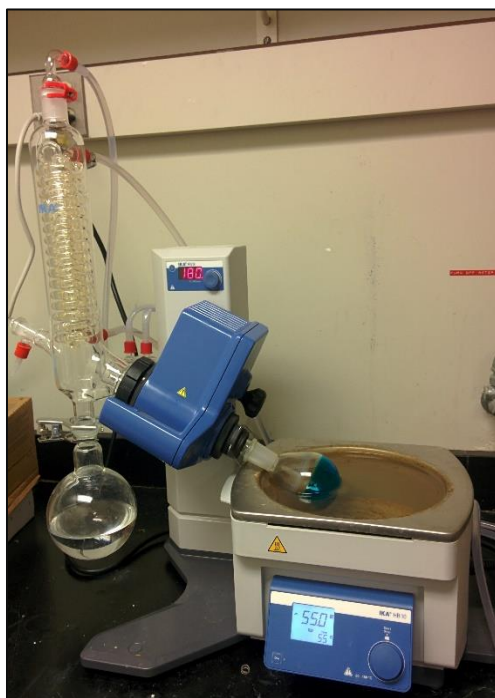


Figure 26: The IKA rotary evaporator and heated water bath system

The rotary evaporator consists of three connected systems: a synthesizing flask with a heated water bath (HB-10, *Ika*), a condenser and evaporate capture flask, and the exhaust port. In the water bath and flask system, the synthesizing flask contained the precursor solution that rotated at a set speed while heated with the water bath. The heated water bath allowed for uniform heating of the flask that was fixed to a set point temperature using the control panel. The flask was connected to the condenser and evaporate capture flask. Cold water was fed into

the condenser system in order to ensure that the evaporate cooled rapidly and dripped into the capture flask. Lastly, a low-pressure pump and digital pressure gauge were attached to the exhaust to attain pressures down to 75 Torr in the rotary evaporator.

2.3.1.1 Refluxing

The precursor synthesis was outlined in *Araki et al.* [44]; it is the fundamental basis of most TFA-MOD precursor synthesis procedures, including that of our group. As discussed in Chapter 1, the creation of the precursor solution begins with Y:Ba:Cu at a stoichiometric mixture of 1:2:3. Powders of yttrium acetate (99.9%, *Sigma Aldrich*), barium acetate hydrate (99.9%, *Sigma Aldrich*), and copper acetate monohydrate (98%, *Sigma Aldrich*) were the sources for the Y, Ba, and Cu. The powder mixture was then added to trifluoroacetic acid at a 1:1 ratio inside the synthesizing flask. The flask was then attached to the rotary evaporator and spun at 180 RPM over a hot water bath at a temperature of 80 °C. Vacuum conditions were used as well to speed up the chemical reactions. At this stage, the solution is refluxed to form a solution of metal-trifluoroacetates, with acetic acid and water impurities. After 4 hours of refluxing, a viscous blue gel was formed.

2.3.1.2 Evaporation

Methanol was added to the viscous blue gel inside the synthesizing flask to bond to and evaporate the impurities. The flask was spun and the water was set to a lower temperature of 50 °C. After evaporating the solution, a slightly lighter blue viscous solution formed. The initial evaporation step took approximately 2 hours with 30 mL of starting solution. This evaporation step was repeated twice more with a total of three evaporation passes on the precursor solution. The time till a viscous gel forms reduced with each evaporation step, with the last pass typically taking 20 minutes with 30 mL of starting solution. With the final viscous gel, a set

amount of methanol was added in order to reduce viscosity, and then, stored in sealed containers.

2.3.2 Coating

The precursor solution was coated on the CeO₂ buffered-tapes using a spin coater (6800, SCS) to create a gel thin film. Figure 27 shows a typical spin coating process for an MOD process. A normal spin coating process was done at 4000 RPM with 180 second duration and 15 second ramp up time.

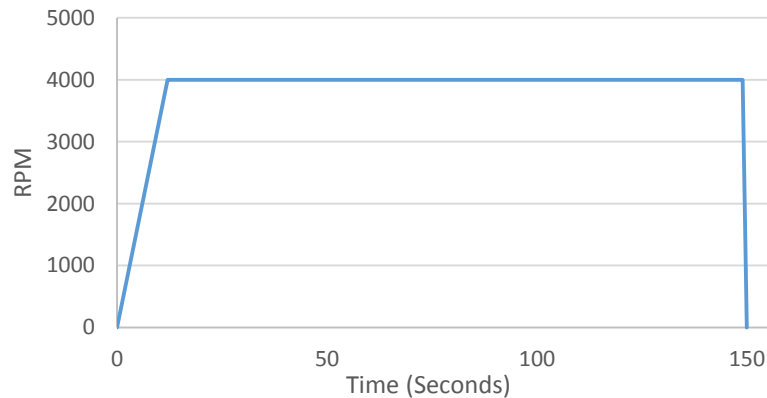


Figure 27: Typical spin coating profile for precursor solution during MOD process

2.3.3 Calcination

The first of the two heat treatment processes is the calcination phase that transforms the gel film into a Y-Ba-O-F amorphous matrix with CuO nanocrystallites. The calcination also removes the organic components within the film. The coated samples were inserted to the center of the quartz tube of the TFA-MOD system and sealed. The sample was then heat treated at different gas environments for approximately 1,200 minutes. Table 1 shows an example of the calcination process which was modified from the standard TFA-MOD procedure outlined in *Araki et al.* [43]. Figure 28 is a schematic of the temperature profile in the calcination step.

Several variations in the growth process were studied, including changes in calcination duration, max temperature, and gas flow rate.

Table 1. Calcination Gas Flow and Temperature Settings

Time (min)	Temperature(°C)	Gas switch
0	20	Flow oxygen
0-72	20-200	Switch to moist oxygen at 200°C (72min)
72-872	280-400	
872-992	400-20	Switch to dry oxygen at 400°C (992min)
992-1182	20	

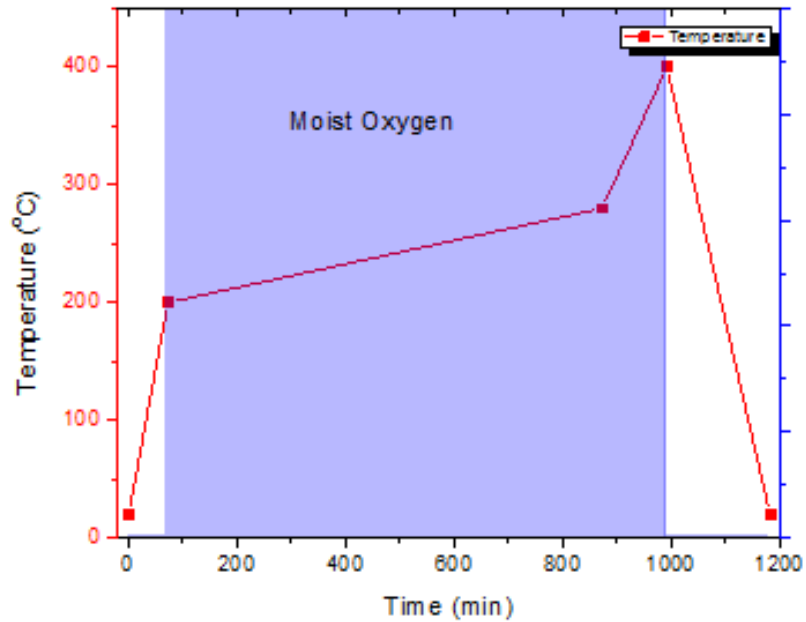


Figure 28: Typical temperature profile for calcination.

2.3.4 Crystallization

The second heat treatment is the crystallization step. The sample is again heat treated at different gas environments to from epitaxial thin film YBCO. Table 2 shows an example of a

crystallization procedure that was modified from *Araki et al.* [43]. Figure 29 shows a schematic of the temperature profile in the crystallization step. Several variations were also made to the crystallization process in order to optimize YBCO growth, including mixed gas content, relative humidity, and max crystallization temperature.

Table 2. Crystallization Gas Flow and Temperature Settings

Time (min)	Temperature(°C)	Notice
0	25	Flow Ag/Oxygen mixture.
0-29	25-750	Switch to moist gas at 200°C (7min)
29-299	750	Switch to dry gas 30min before the gas ramp down. (269min)
449-479	450	Ramp to room temperature afterwards

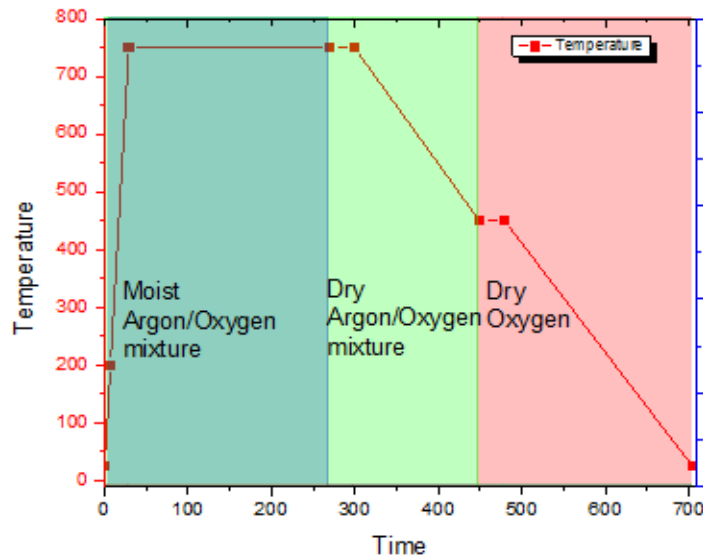


Figure 29: Typical temperature profile for crystallization including gas environments

2.4 Metal-organic Chemical Vapor Deposition

The YBCO film was also deposited using an MOCVD system on the CeO₂ buffers. As in the ion bombardment process, the samples were spot welded together on to leader tapes with side-stripping and then wound in spools. YBCO was deposited on the spooled samples in a cold-walled reel-to-reel MOCVD system.

2.5 Sample Characterization

The nanostructures and superconducting films were imaged using scanning electron microscopy (LEO-1525). Phase content and crystal orientations were analyzed using an x-ray diffractometer (D5000, *Siemens*) and a general area detector diffraction system (GADDS Version 4, *Bruker AXS*).

2.5.1 Measurement of Superconducting Properties

After deposition of the superconducting films, a layer of silver was sputtered onto the film in order to protect surface of the material as well as to provide electrical contacts for critical current measurements. Using a silver sputtering system at 150W, a 1 μm thick silver layer was deposited. Additionally, the silver-sputtered samples were oxygenated in order to introduce adequate oxygen in the lattices of the REBCO films. The sputtered samples were loaded into a furnace and oxygenated with 50 sccm of oxygen gas flow at 500 °C for 2.5 hours.

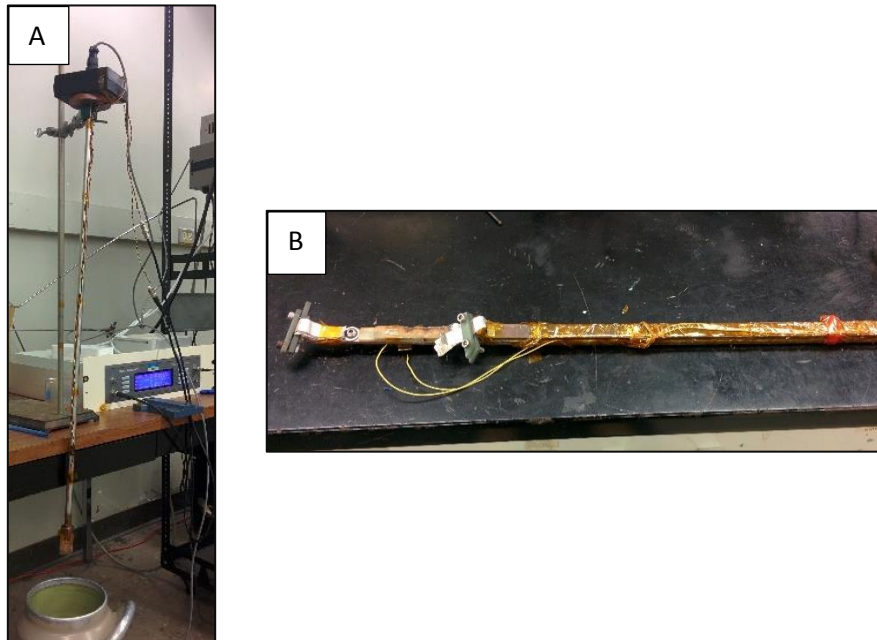


Figure 30: (A) Critical temperature testing probe, (B) Critical current testing probe.

After oxygenation, several superconducting properties were measured. The transition temperature (T_c) was measured using an inductive method with a custom-built probe seen in Figure 30a. During operation, the sample was securely placed between the excitation and pickup coils and then cooled down to 77K using liquid nitrogen. An input current was applied to the excitation coil to generate a magnetic field resulting in an induced current in the pickup coil. A lock-in amplifier (SR530, *Stanford Research Center*) was used to analyze the signal. The sample was then slowly warmed up and the temperature was monitored using a silicon diode temperature sensor (DT-470, *Lake Shore Crytronics*). When below the T_c , the sample remained superconducting, expelling all flux lines. As the sample's temperature increases, the sample becomes non-superconducting, leading to a rapid increase in the induced signal. The temperature at which the initial induced signal is located is the lower-bound T_c and the temperature where the induced signal crosses the transition is the upper-bound T_c . The midpoint of the upper- and lower-bound T_c values is determined to be the T_c of the sample.

The self-field I_c measurements were completed using a conventional four-probe system; the probe used in this system seen in Figure 30b. Voltage taps from the probe were soldered to the substrate on its silver surface. The two voltage probes were connected to a dual-channel nanovoltmeter (2128A, *Keithley*). The sample was then soldered on to silver tapes on each end and attached to current leads. During operation, the sample was submerged in liquid nitrogen and transport current was supplied to the current leads from a power supply (GEN-3300W 600A, *Lambda*). A nanovoltmeter recorded the voltage difference between the two voltage probes versus the current. In-field I_c measurements were conducted using a 9 T magnet that applied external magnetic fields onto the samples. Figure 31 shows a schematic of the in-field measurement system. During operation, a stepper motor rotates the sample around the axis parallel to the current direction while an external magnetic field is applied perpendicular to the current. A hall probe located on the sample holder measured the applied field versus the angle of the sample. Current and voltage measurements were done as in the critical current measurement system explained above. These measurements were used to obtain angular and field dependent critical current values.

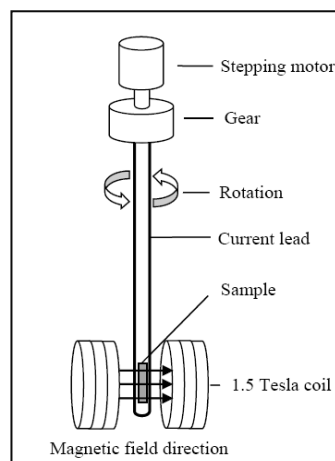


Figure 31: Custom in-field measurement system to measure angular and field dependence of critical current

2.6 ImageJ

The scientific imaging tool ImageJ was used to easily analyze and quantify nanostructures. With thousands of nanostructures in a single high-magnification SEM image, ImageJ's object processing allowed for quantification and analysis of nanowire densities and nanoparticle dimensions. To obtain a nanowire density, a top-down image at a set magnification was processed with the threshold and edge tools to select only the desired nanostructures. Then, the image was analyzed by measuring the area effectively occupied by the nanostructures relative to the total area of the substrate. This area percentage is labeled the Effective Nanostructure Density and it allows for a simple and rapid approximation of the area unavailable to the superconducting thin films due to the nanowires. A set magnification in the images was used so as to always examine the exact amount of area in all density-studied samples. Density analysis was also performed on samples before and after ion bombardment to analyze the amount of nanowire removal. To count nanoparticles, the image was similarly adjusted like above and processed using the 'analyze particles' tool. The particle size threshold was adjusted so as to properly select all desired nanoparticles. The 'analyze particle' tool evaluates the area of each particle as well as the number of nanoparticles. Figure 32 shows example ImageJ processing data.

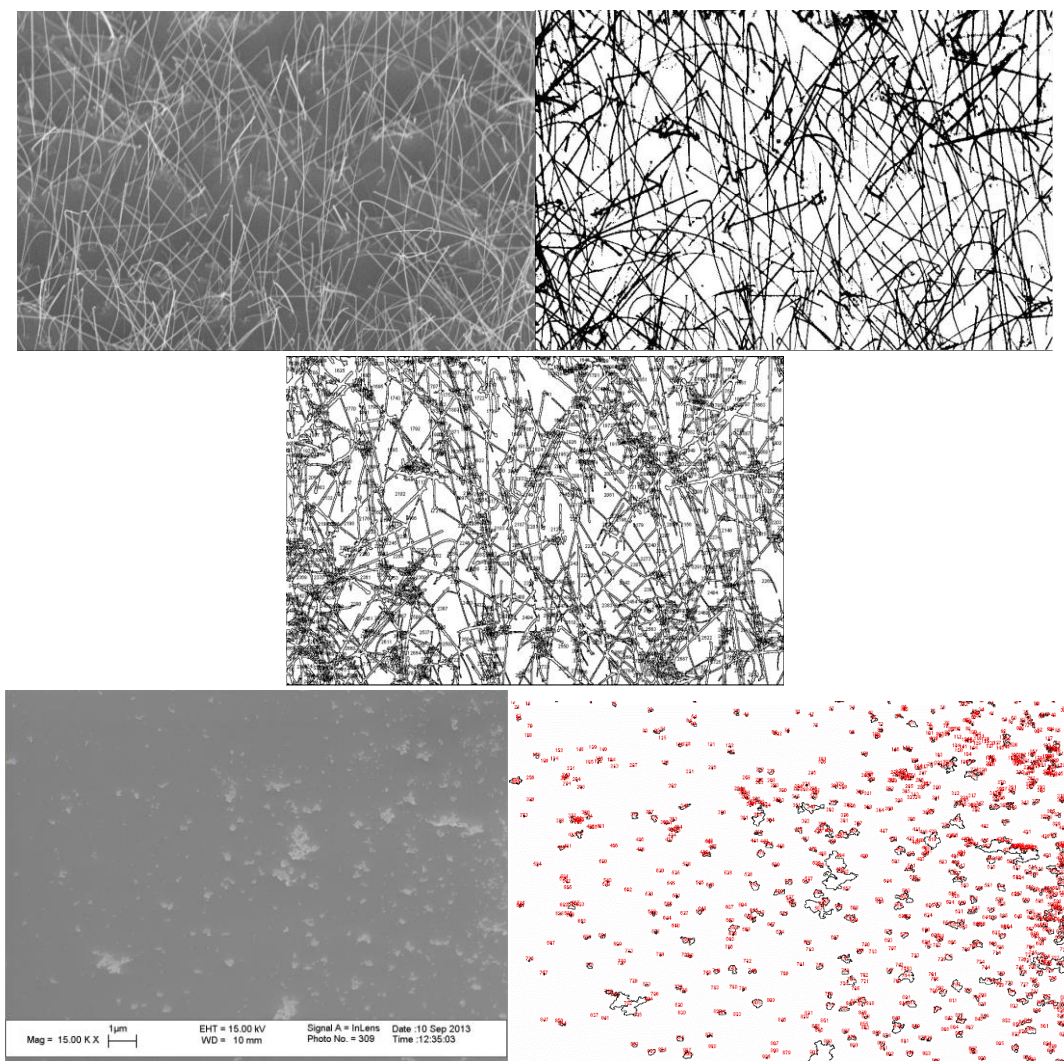


Figure 32: (Top-left) Original NW SEM image, (top-right) ImageJ post processing and (center) area analysis on nanowires. (Bottom-left) Original microstructure SEM and (bottom-right) ImageJ image data that has processed the nanoparticle count and area

Chapter 3: Results and Discussion

3.1 Tin-Oxide Nanowire Fabrication

Tin-oxide nanowires were successfully fabricated under the VLS mechanism using the CVD system. Numerous types of nanowire morphologies were explored on the CeO₂ buffer tapes. Additionally, various system optimizations had to be investigated in order to create a repeatable and uniform nanowire array for thin film applications.

3.1.1 Growth Mechanism

As discussed earlier, the growth of nanowires through the VLS mechanism requires metal catalysts as seeds for the synthesis of 1D crystalline nanowires. In this work, the bare CeO₂ buffer tapes were seeded by either colloidal solution or sputter coating nanocatalysts. In the first step of the growth process, the evaporated tin powders were transported by the Ar carrier gas to the Au catalysts to form Sn-Au eutectic liquid alloys at temperatures above 400 °C. The Sn atoms act as solutes, diffusing into the Au metals and eventually forming a saturated alloy. At the growth temperature (600-700 °C), the Sn-Au alloys absorb the available oxygen in the reaction zone. It is important to note that no additional oxygen was added into the CVD system. As demonstrated in prior work, the remnant oxygen atoms in a system at 0.10-0.530 Torr pressure range was sufficient to form crystalline nanowires [31]. Experiments with added oxygen in the carrier gas (up to 8% O₂) resulted in stunted nanowire growths due to oxidization of evaporated Sn powders prior to reaching the Au catalyst.

With oxygen, the metal alloys form SnO₂-Au liquid droplets. At the growth temperatures, the SnO₂ precipitates out of the saturated alloy onto the buffer surface to form 1D crystalline nanowires. At the solid-liquid interface, further crystalline SnO₂ is precipitated as more incoming evaporated Sn atoms diffuse into the liquid alloy and sustains the growth of the

nanowire while the Au catalyst rises to the tip. After the growth is completed, the Au metal tip cools forming a 'beak-like' solid. Figure 33 shows an optimized nanowire array after a completed CVD growth process with multi-direction nanowires displaying their gold tip in their 'beak-like' structures. The out-of-plane nanowires had a crystallographic growth direction of [110] [31] and their diameter was primarily determined by the diameter of the start gold nanoparticles. Thus, with larger gold nanoparticles, the nanowire diameter increased.

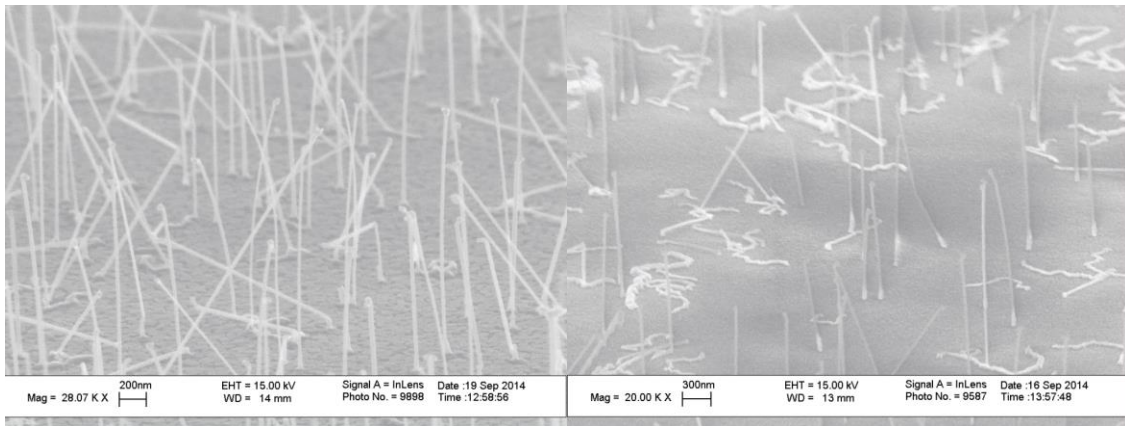


Figure 33: SEM images of (left) a completed optimized VLS growth for tin-oxide nanowires with 40 nm colloids on CeO₂ buffer displaying their 'beak-like' Au tips, and (right) an unoptimized growth displaying large densities of 'snake-like' in-plane nanowires

Along with out-of-plane nanowires, surface defects such as in-plane nanowires were also created. Seen in Figure 33, these in-plane nanowires are hypothesized to be caused primarily by the mobility of the gold catalyst on the buffer surface. Reduction of in-plane nanowires was imperative since they can easily impede the deposition of superconductor thin film on the substrate surface. In the following sections, various growth factors for VLS nanowire growth are explored, including methods that led to optimized growths and reduction in surface defects such as in-plane nanowires.

3.2 Colloidal Growth Factors

3.2.1 Buffer Type

Two different buffer types were initially explored for SnO₂ nanowire growth: LaMnO₃ (LMO) and CeO₂. Extensive work done previously showed unfavorable growth on MgO, SrTiO₃, and (111) silicon wafer substrates due to large lattice mismatches [31]. Focus was shifted to LMO and CeO₂ buffers since they are routinely used for the superconductor growth by MOCVD and MOD respectively. Figure 34 shows representative results of SnO₂ nanowires growths performed at 630 °C and 0.530 Torr with 40 nm gold colloids for 20 minutes.

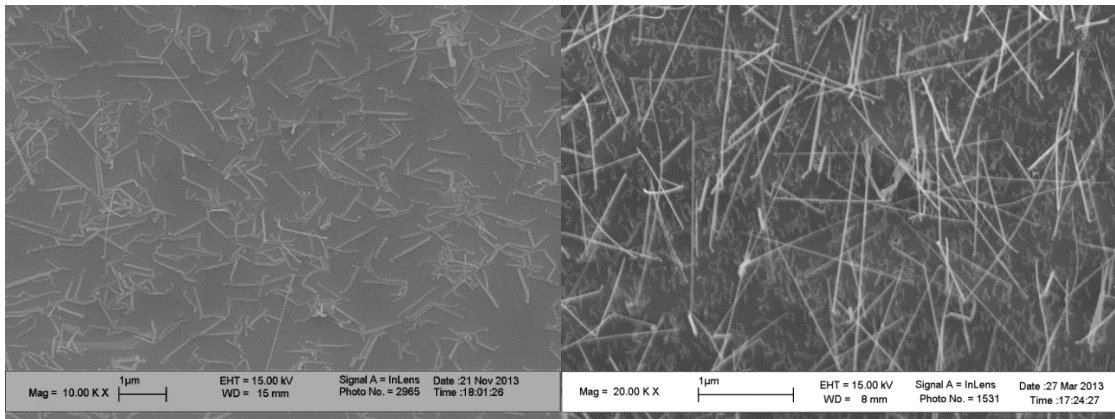


Figure 34: Comparison of VLS growth of tin-oxide nanowires on (left) LMO and (right) CeO₂ buffers

As seen in Figure 34, nanowires grown on LMO buffers showed a higher density of in-plane nanowires when compared to those on CeO₂ buffers. The latter showed a mix of out-of-plane growths and in-plane growths. In fact, after repeated testing, it was found that use of LMO buffers resulted in a significant reduction in the desired out-of-plane nanowires, and an increase in in-plane nanowires. The samples grown on CeO₂ buffers also displayed significant in-plane growth, but, had improved out-of-plane nanowire densities.

3.2.2 Temperature

As substrate temperature being one of the primary factors for CVD growth, its influence on the nanowire growth was investigated. The nanowire growths were tested from temperatures between 550°C and 675°C. The temperature was monitored using a thermocouple attached to the substrate base. Figure 35 shows the surface microstructure of the samples. The samples were grown with 40 nm gold colloids for 20 minutes under 0.530 Torr system pressure.

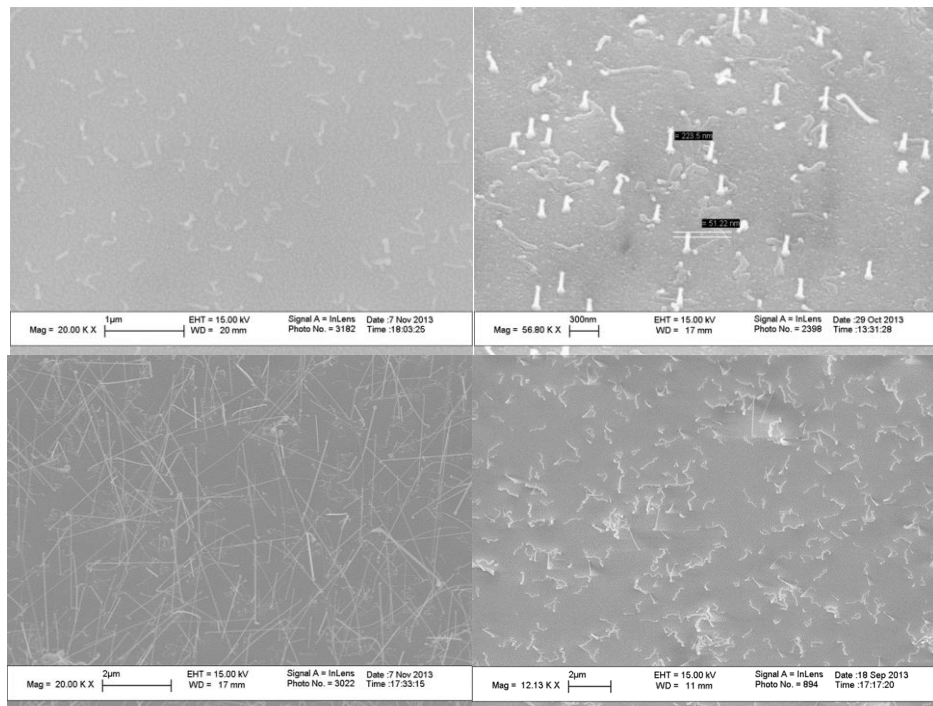


Figure 35: Comparison of nanowire samples grown at (top-left) 550 °C, (top-right) 575 °C, (bottom-left) 630 °C, and (bottom-right) 675 °C.

Samples grown at 550 °C showed short and thick in-plane nanowires with no proper out-of-plane nanowire growth. Increasing the temperature to 575 °C showed results similar comparable to the 550 °C sample, but also included some short, and thick out-of-plane nanorods with 80 nm wide columns. No changes were seen even with increased growth time. At 630 °C, the samples showed proper vertical nanowires, but with significant amount of in-plane nanowire growth. At the last temperature of 675 °C, the vertical nanowire density was again

drastically reduced. The long and thin in-plane nanowire growths also returned, making this growth temperature high undesirable. It is believed that at lower temperatures, there is insufficient vaporization of the Sn metals stunting the nanowire growth. At higher temperatures, the cessation of growth is possibly due to rapid oxidation of Sn metal powders, hindering their continued evaporation [49]. Additionally, the diffusion rates of the Sn-Au droplets are likely increased at higher temperatures allowing the in-plane nanowires to grow fast at increased temperatures.

3.2.3 System Pressure

Another primary factor in CVD growth is the system pressure at which the material is grown. The effects of system pressure on the growth rate of the SnO₂ nanowires have been previously investigated [1] [16]. In this work, system pressure during growth was varied between 0.40 and 0.70 Torr at 630 °C in order to investigate nanowire array growth enhancement. Figure 36 shows the SEM images of the samples fabricated at these conditions.

All the samples were grown for 20 min at a carrier gas flow rate of 20 sccm with 40nm colloids, and annealed with no quenching. At 0.40 Torr, the samples showed long nanowires that had grown much faster than the rest of the batch. Increasing the pressure to 0.50 Torr, the nanowires showed a uniform height of around 1 μm, with a significant reduction of in-plane nanowires. Slightly increasing the pressure to 0.530 Torr, the nanowires again showed an increase in in-plane growths, but additionally, had a significant density of out-of-plane nanowires. At the highest pressure of 0.70 Torr, the majority of the growth was dominated by in-plane wires with stagnated growth of out-of-plane nanowires.

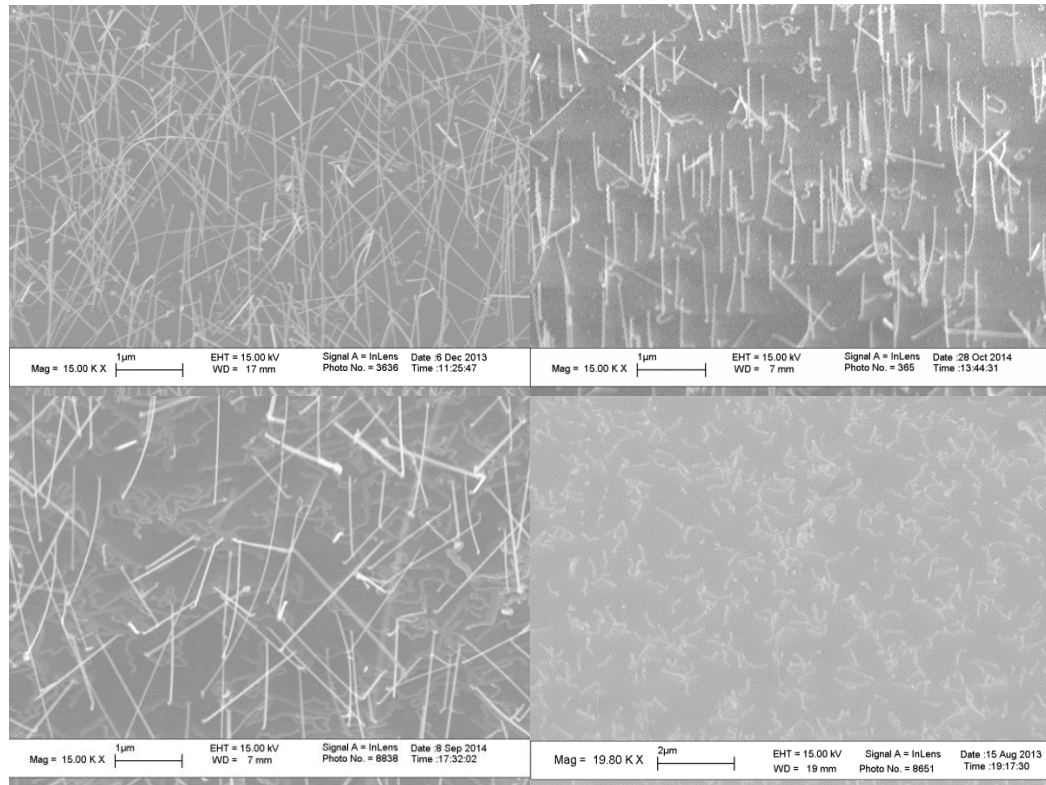


Figure 36: Comparison of nanowire growth in pressures of (top-left) 0.40 Torr, (top-right) 0.50 Torr, (bottom-left) 0.53 Torr, and (bottom-right) 0.70 Torr

One reason for the results might be the effect the pressure on oxygen content. High oxygen partial pressures are known to stagnate nanowire growth [49]. Decreasing the system pressure resulted in lowering the oxygen content and allowing the Sn metals to vaporize before oxidation. Increasing the system pressure leads to an increase in the oxygen content. At high oxygen content, the Sn metals are oxidized before evaporation leading to reduced vertical nanowire growth.

3.2.4 Growth Time

The nanowire growth times were investigated to determine their influence on the nanowire lengths. The samples were grown with annealed 40 nm colloids under 20 sccm carrier gas flow rate at 630 °C, and 0.50 Torr system pressure. Figure 37 shows the expected results. While increasing the growth times, more Sn source was evaporated and thereby, the nanowire

lengths are increased. At 10 minutes of growth, the nanowires were around 800 nm in length. At 20 minutes, the length increased to approximately 1.5 μm . Doubling the time to 40 minutes showed extremely long nanowires, with some nanowires over 4 μm in length. At this growth length, it was evident that certain nanowires experienced growth direction switches, which is common in nanowires above 1.9 μm in length. This growth switch is due to build-up of atomic layer defects in the intermediate molten zone in the Sn-Au interface [40], as detailed earlier in Chapter 2.

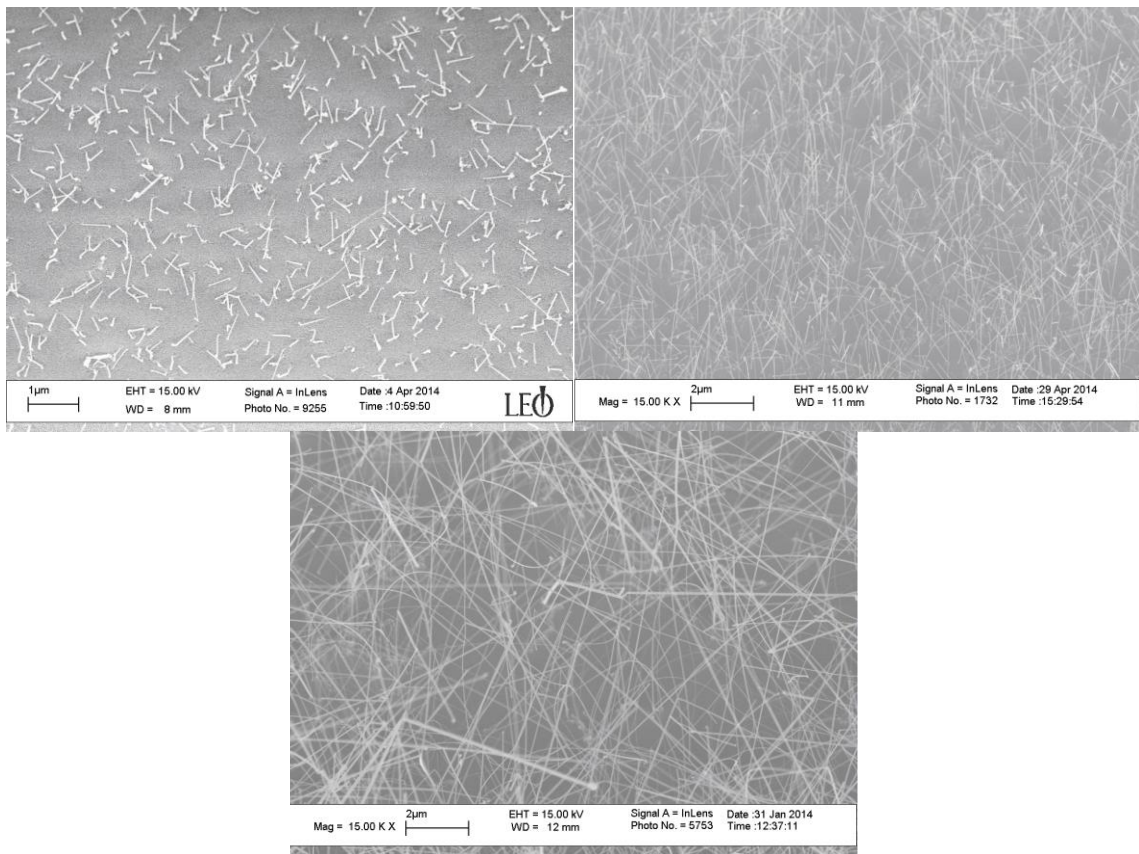


Figure 37: Comparison of NWs grown for (top-left) 10 min, (top-right) 20 min, and (bottom) 40 min

3.3 Defect Reduction Methods

In order to create a uniform bed of nanowires in the CVD process for subsequent superconductor deposition, several growth defects had to be addressed. The preliminary experiments involved creating reliability and repeatability in the growth of nanowire arrays. The initial growths showed lack of repeatability between CVD runs, in which the effective nanowire densities could vary up to 28% from the desired target and 25% between the sample edges and center. As discussed further below, optimization of process parameters such as gas flow direction and substrate annealing significantly improved the repeatability and reliability.

In the second set of experiments, surface defects such as conglomerations, in-plane nanowires, and excess tin powder were explored. Figure 38 shows the Au colloids conglomerating before and after CVD growth. The nanoparticles stabilized into large conglomerations during the seeding process and created patches of nanowires along the substrate surface during growth.

Figure 39 shows the excess tin powder, and in-plane nanowire defects on the sample surface. Several types of experiments were performed including colloidal baths, annealing and additional heat treatment methods in order to reduce the colloid conglomerations, excess tin powder and in-plane nanowires. The following sections discuss the results.

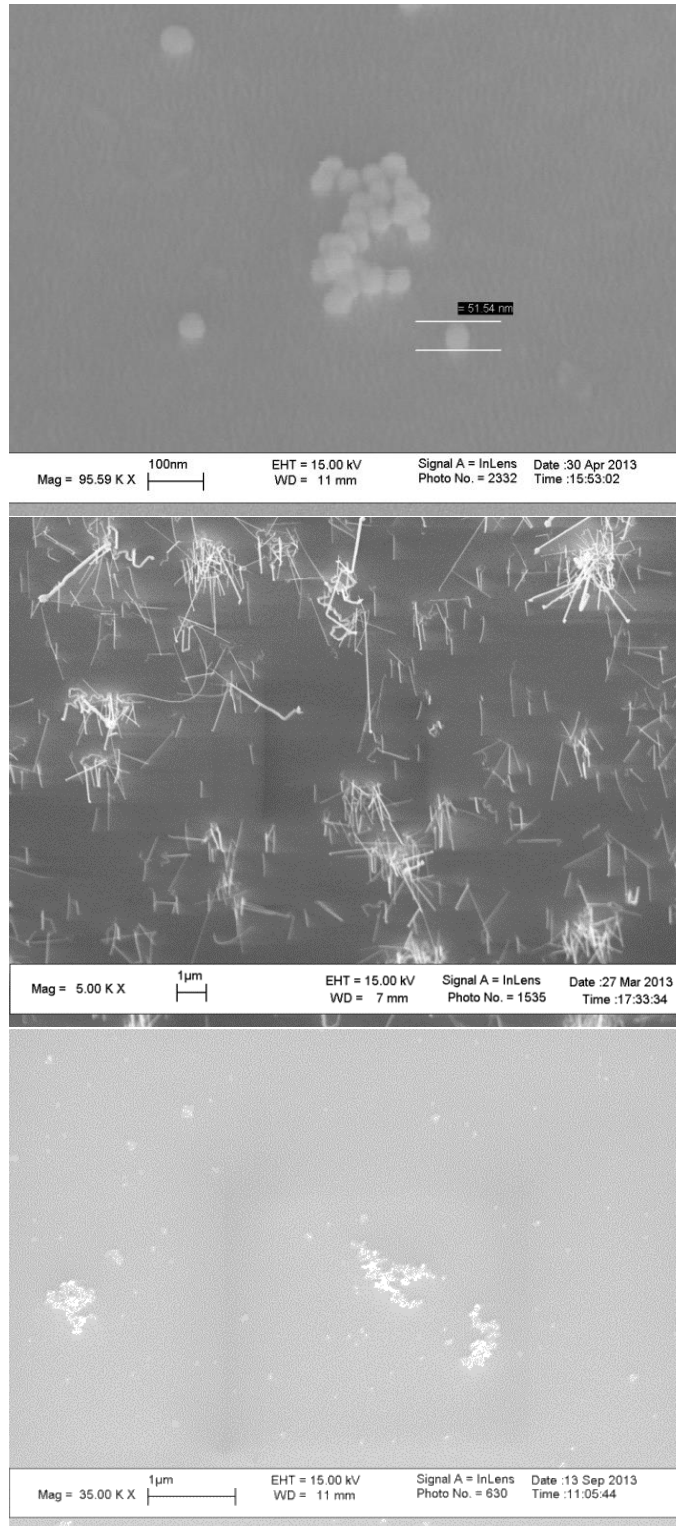


Figure 38: SEM images highlighting the (top) conglomerated nanoparticles that lead to (center) nanowire clumping defects. (Bottom) The initial seeding procedure resulted in large conglomerations that compromised nanowire array growth

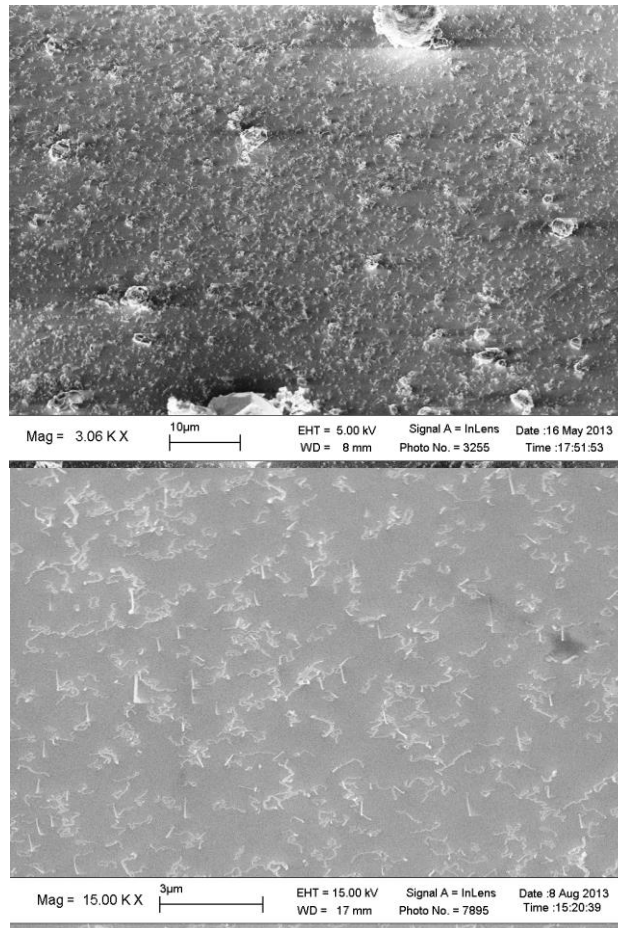


Figure 39: (Top) Excess tin powder of the substrate after nanowire growth due to gas flow rate and direction. (Bottom) Large density of in-plane nanowires on the substrate surface

3.3.1 Venting Gas Flow Rate

Perhaps the easiest defect to fix was to eliminate tin powder landing on the substrate surface while venting the system from vacuum. Various venting gas flow rates were tested in order to find an adequately fast venting rate while keeping the surface clean. Figure 40 shows the SEM image results.

At above 4000 sccm, it is clear that the high gas flow rate disturbs the system under vacuum far more than that at the other two flow rates. This turbulence at the high vent flow rates allows excess evaporated tin powders to reach and attach to the substrate. At 4000 sccm

and below, there were no noticeable tin powder defects found all along the surface. The venting rate of 4000 sccm was selected so as to vent the system fast while keeping the sample clear of tin powders.

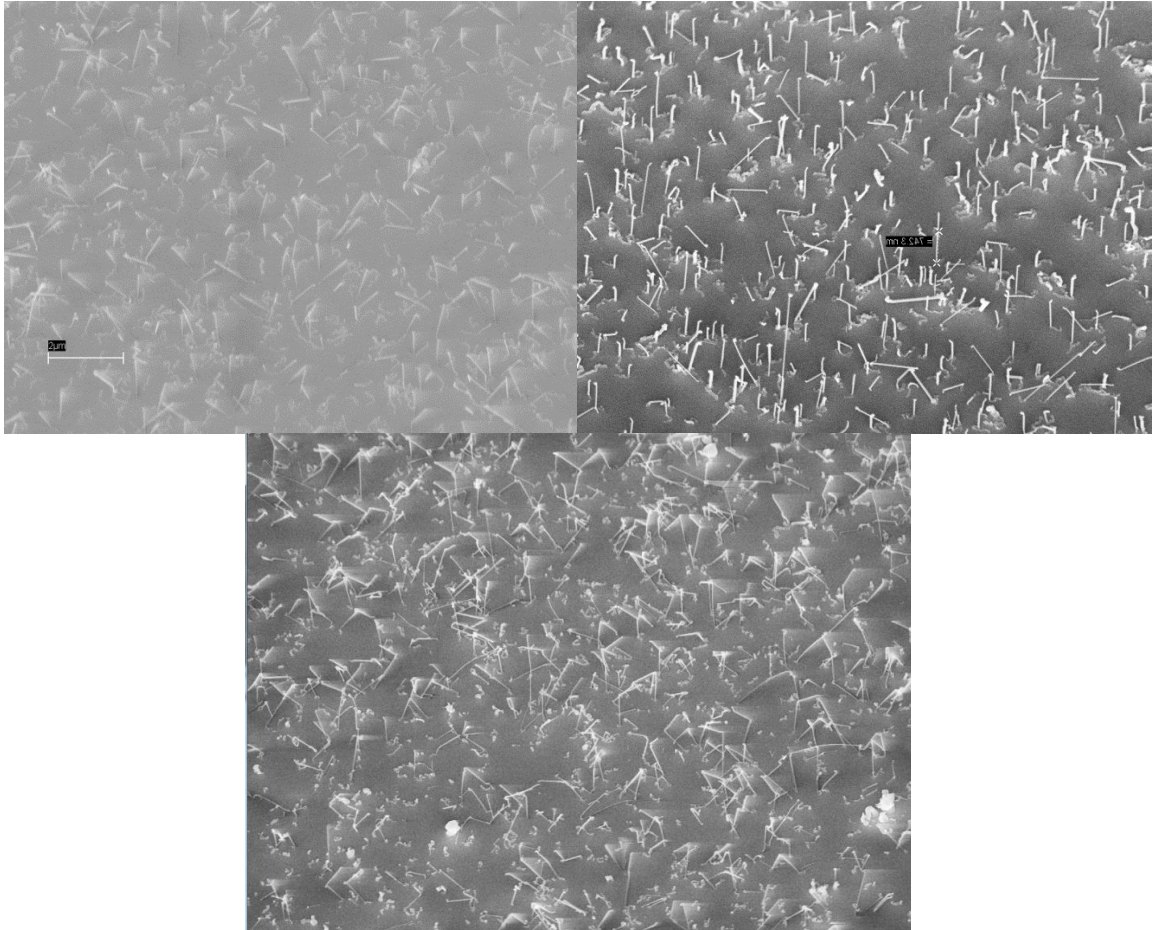


Figure 40: Comparison of nanowires in processes where the system was vented with a gas flow rate of (top-left) 2000 sccm, (top-right) 4000 sccm, and (bottom) 6000 sccm

3.3.2 Colloidal Bath

As mentioned in Chapter 2, heated ultrasonic baths have been shown to reduce nanoparticle conglomeration. Our work used a modified system in which the colloidal solution was prepared in a heated ultrasonicator using a capped centrifuge tube as a container. The SEM images of the results are shown in Figure 41.

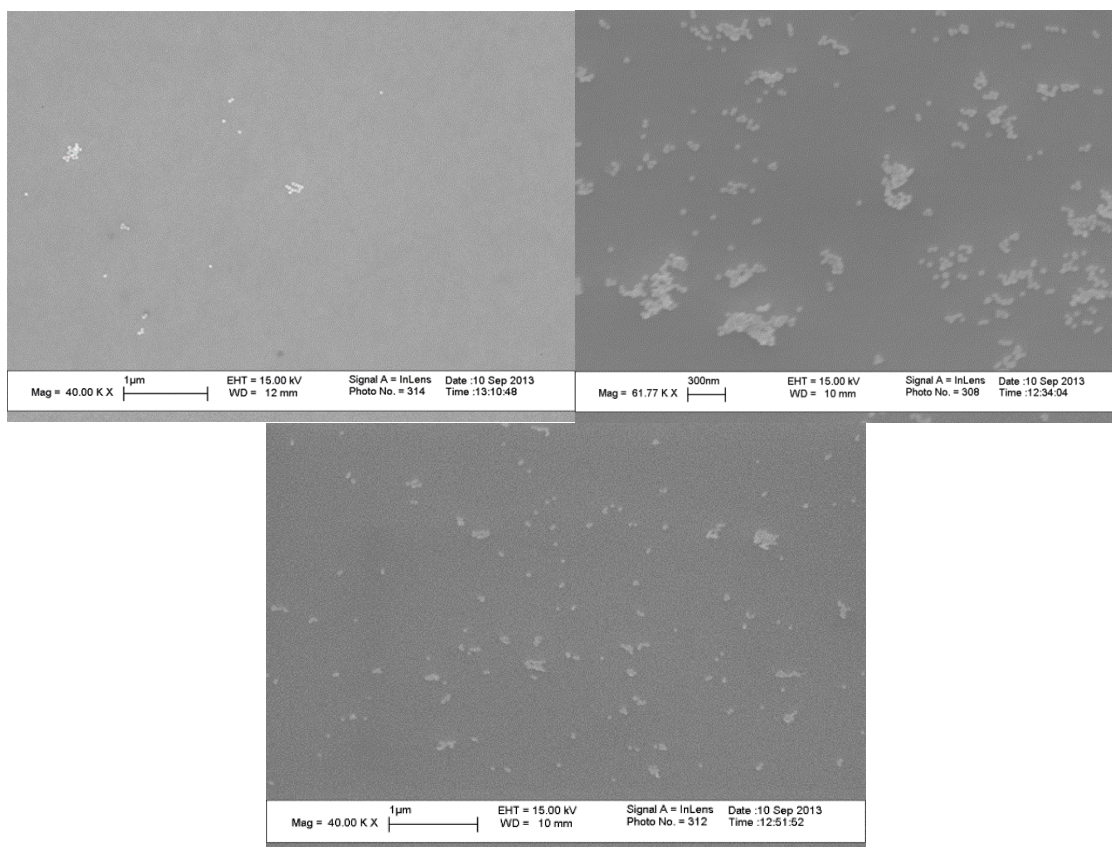


Figure 41: Results of heated sonication at 120°F with samples sonicated for (top left) 5 min, (top right) 30 min, (bottom left) 60 min

Figure 41 reveals that there is a definite improvement at 5 minutes of heated sonication but a huge increase in conglomeration at 30 minutes and 60 minutes. A possible reason for this result might be that at a certain critical ultrasonication time, there is an increased likelihood of gold nanoparticles reaching other gold particles, thus, stabilizing and forming conglomerations. However, the initial 5 minutes is short enough of a time for the initial conglomerated particles to be separated from their weak bonds. Figure 43 shows the average nanoparticle size and standard deviation as analyzed through ImageJ's particle size tool, after processing in ultrasonic bath.

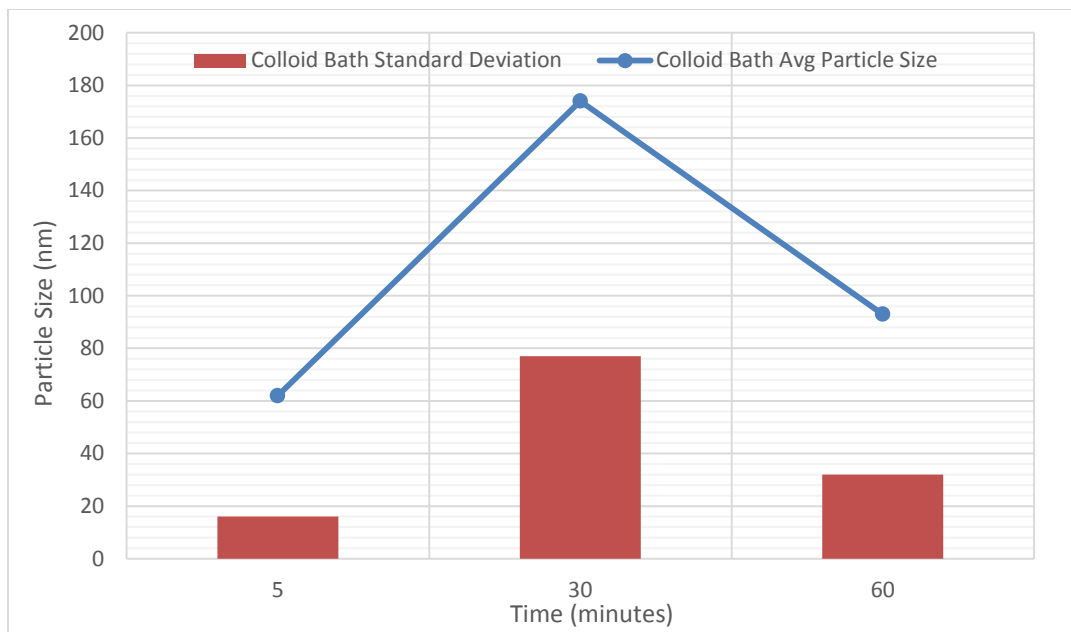


Figure 42: Plot of the average and standard deviation of nanoparticle sizes after processing in heated ultrasonic bath

From the plot above, it can be seen that at 5 min of the colloidal bath, the nanoparticle showed an average size of 60 nm, though there were deviations as large as 20 nm. At 30 min, the average particle sized increased to nearly 180 nm (i.e. conglomerations) with a substantial standard deviation of 75 nm indicating a high level of conglomeration of 20 nm nanoparticles. At 60 min, the average size and deviation reduced to approximately 90 nm and 30 nm, respectively. The reduction of particle sizes at 60 min is likely due to the colloid bonds with the pol-l-lysine and substrate deteriorating at longer heated ultrasonicated baths. However, there was still a significant level of conjoined gold colloids.

3.3.3 Spin Coated Colloid Application

A more standard approach was also taken by spin coating the colloidal solution on to substrate. Figure 43 shows the results of spin coating at 70, 170 and 300 RPM at a ramp up time of 15 seconds.

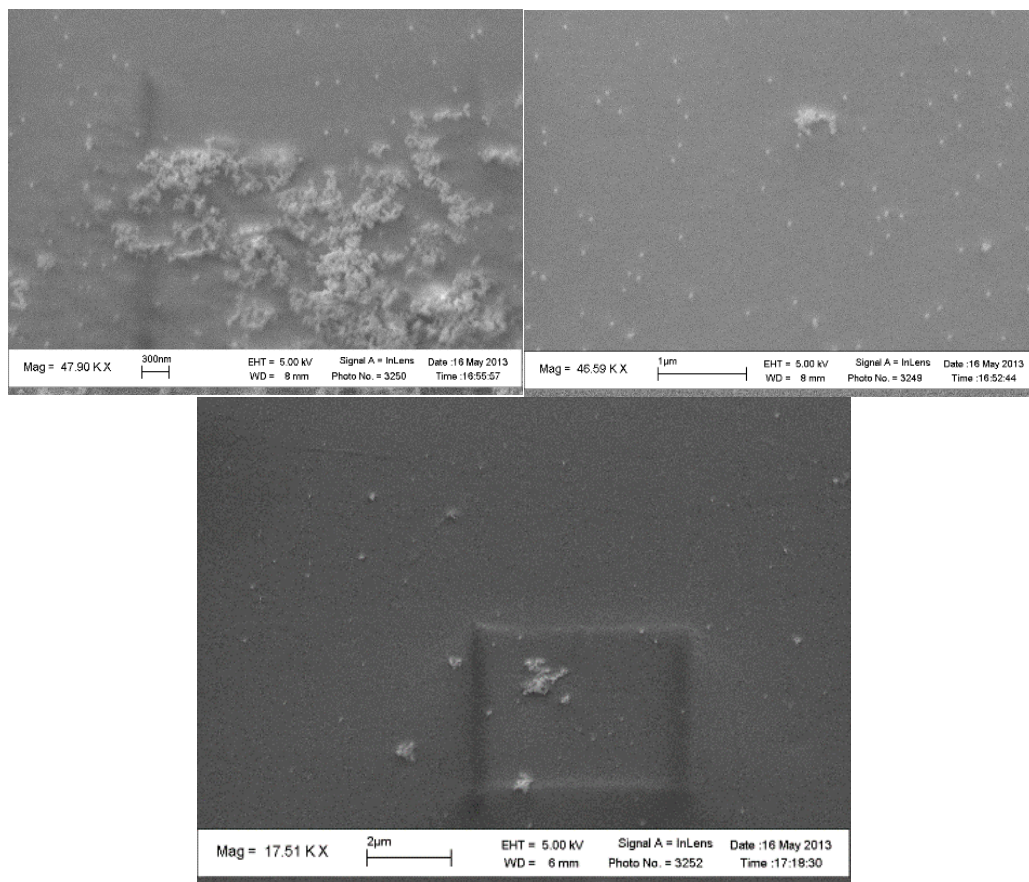


Figure 43: Results of spin coating with a ramp up time of 15 seconds at (left) 70 RPM, (center) 170 RPM, (right) 300 RPM.

The results show detrimental effects of spin coating colloidal solution on CeO_2 flexible substrates, with a high level of conglomeration at 70 RPM. This is because the solution disperses quickly even at low RPMs, leaving only high densities of conglomerated particles at the edges with almost no nanoparticles in the center. Because the wetting angle of CeO_2 is unfavorable for spin coating, the higher RPM tended to result in high levels of conglomeration at the edges but almost no nanoparticles in the center. At 500 RPM, the colloidal solution film on the substrate was non-existent due to the wetting angle. These results indicated that spin coating is not an effective method for reducing conglomeration with gold nanoparticles on flexible CeO_2 substrates.

3.3.4 Stirred Colloid Application

The last mechanical approach to reducing conglomeration was to stir the solution at 1 minute, 5 minute and 25 minute durations prior to depositing on the buffer. The SEM images in Figure 44 reveal stirring for any duration up to 5 minutes is effective in reducing conglomerations, but at 15 minutes, the particles have re-formed into bigger nano-conglomerates. Stirring at 1 and 5 min had a drastic improvement by eliminating all conglomerations larger than 200 nm. However, a small density of 100nm-sized nanoparticle bodies still existed. Stirring the solution for 25 min showed high conglomeration densities similar to the control sample, as seen previously in Figure 38. This is possibly due to the increased stirring time allowing nanoparticles to increase their likelihood of interacting with other nanoparticles and forming conglomerations, as seen in the ultrasonication samples heated for longer durations.

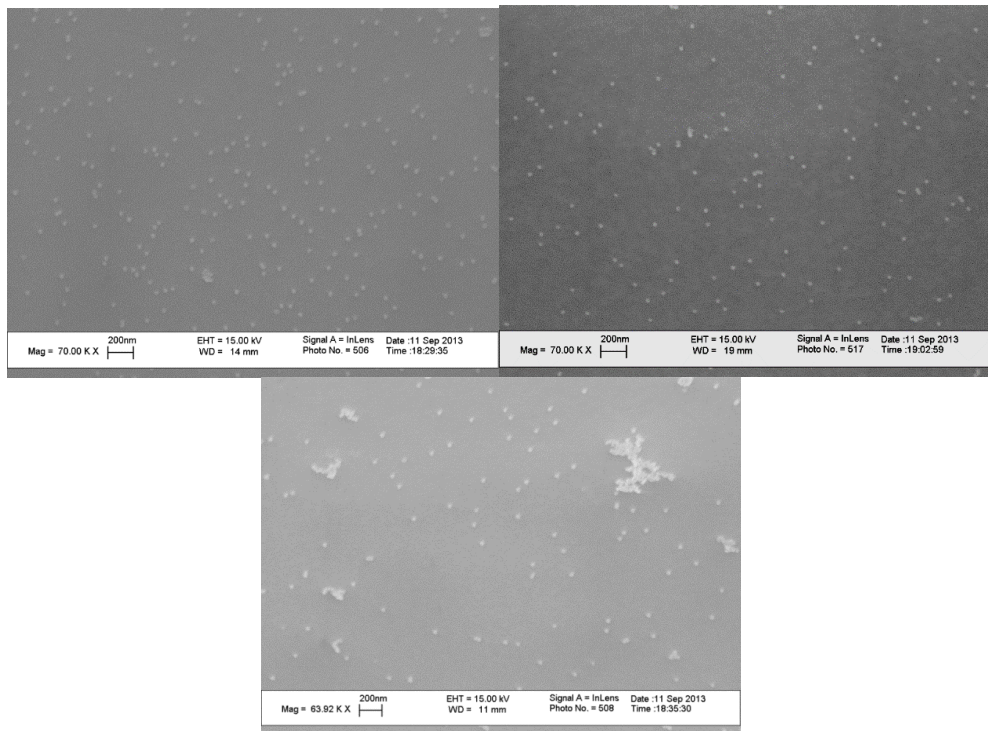


Figure 44: Results of magnetically stirring the colloidal solution for (top-left) 1 min, (top-right) 5 min, (bottom) 25 min.

3.3.5 Substrate Annealing

Annealing the substrate prior to nanowire growth was also explored in order to reduce conglomerations. It was found that annealing the samples after seeding at temperatures above 400 °C on the CeO₂ buffers, the conglomerations would dissociate and re-form into larger colloids, thereby, eliminating patches of nanowires. The Au nanoparticles are in a semi-molten state above 400 °C, and the free Au atoms and nanoparticles attach themselves to adjacent gold particles in order to form larger and more stable gold colloids [31]. For the annealing process, the sample was placed in the same CVD system and heated in the sample holder for the set amount of time at 630 °C. Several annealing times were explored in order to determine how long a sample was to be annealed in order to create a uniform bed of nanoparticles. Figure 45 shows the results from annealing 0.30 mL of 40 nm Au colloids for 10min, 20 min, and 40 min.

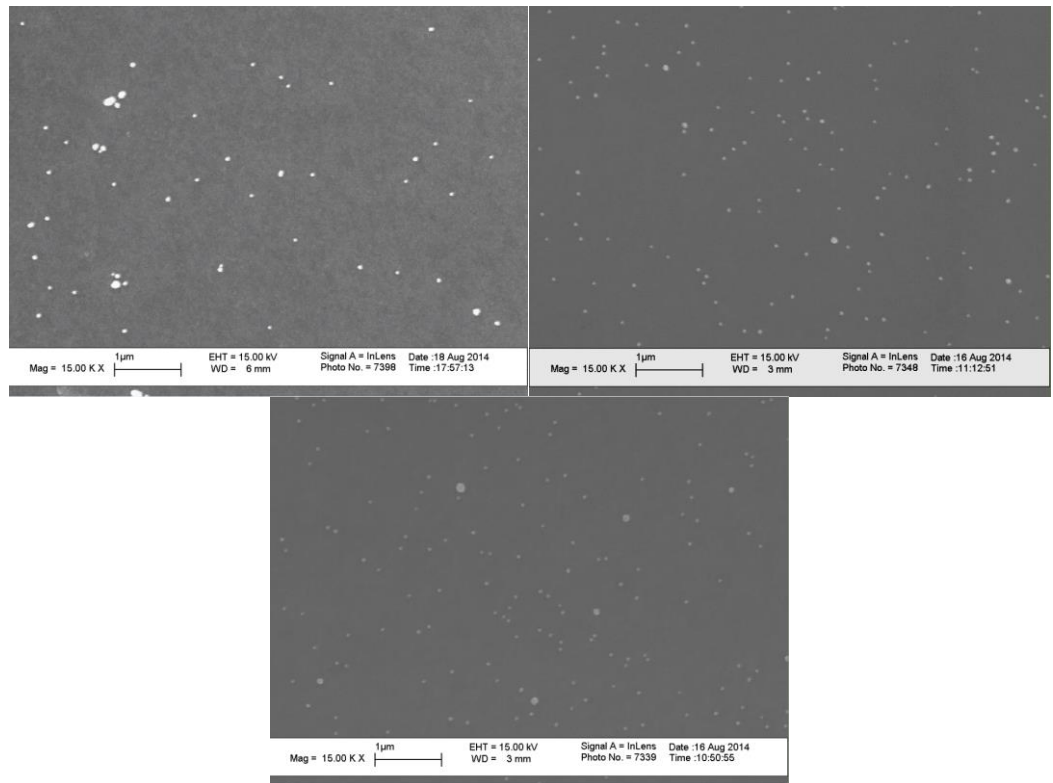


Figure 45: Results of annealing samples after gold colloid deposition at 630°C for 10, 20, and 30 min

As seen in the figures above, all annealing times showed marked improvements in reducing conglomerations of the nanoparticles. After 20 min and 40 min of annealing, the results showed equivalent and dramatic reductions in nanoparticle conglomerations. At 20 min and greater, some of the Au colloids dissociated and re-formed nanoparticles as large as 100 nm in diameter. Additionally, at those annealing times, the samples showed a near ideal uniform array of nanoparticles from edge to edge. After 10 min annealing, there were significant reductions in nanoparticle conglomerations, however, some minor conglomerations were still found with indiscriminate SEM scans along the sample surfaces. The reduced annealing time was insufficient in reducing conglomerations in comparison to the reduction amounts in the 20 and 40 min annealed samples.

3.3.6 Carrier Gas Flow Direction and Rate

Chemical vapor deposition growth dynamics for SnO₂ nanowire arrays are primarily controlled by mass transport phenomena. Thus, the carrier gas flow direction and rate were explored in order to create more uniform and repeatable nanowire growth arrays. The carrier gas was composed of ultra-high purity (99.99%) inert Argon gas. Initially, CVD growths were completed with the standard forward gas flow direction, where the carrier gas can carry the evaporated tin powder directly towards the substrate surface. However, forward gas flow created high levels of non-uniformity, low repeatability and excess tin powder on the surface. This was largely due to the inhomogeneity of the gas flow in the forward direction. In the current CVD system setup, there was approximately 10 cm (the distance between the tin powder boat and the sample holder) for the evaporated tin to form a homogenous vapor. However, at even low carrier gas flow rates, the center of the nanowire samples was often 20%-30% more dense than the edges, indicating large inhomogeneity in the incoming gas flow. Some CVD batches even resulted in visible excess tin powder rings at the center of the surface.

Figure 46 illustrates some of the issues found with using forward gas flow. As seen in the figure, the samples showed a wide variance in nanowire densities from the right-edge to center to left-edge. Additionally, excess tin-powders were found along the center of the nanowire array. The samples were also highly unrepeatable since the gas was inhomogeneous, leading to unpredictable results from one sample run to the next.

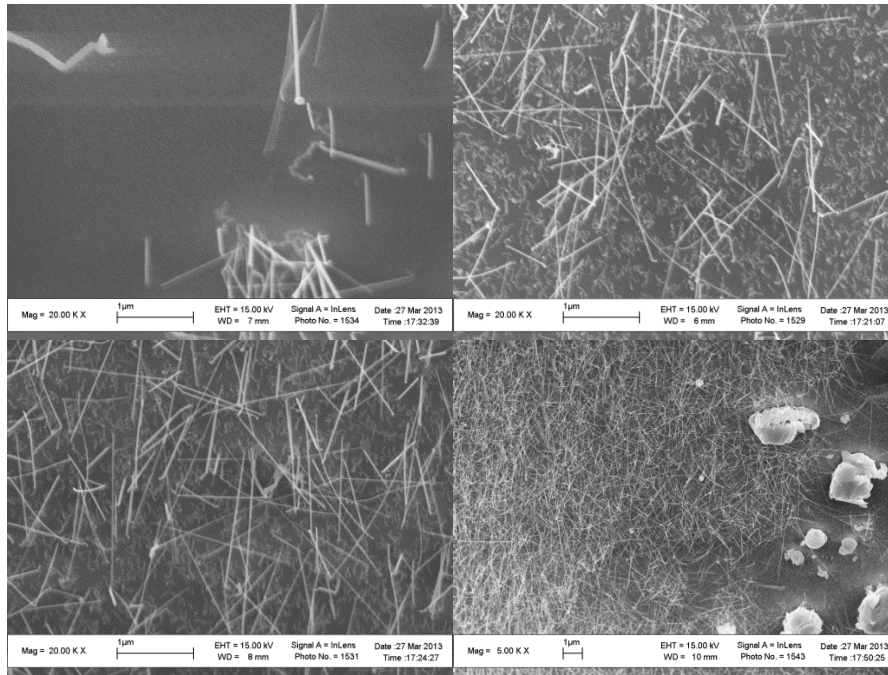


Figure 46: SEM images of the nanowire sample grown in forward gas flow direction showing wide variance in the (top-left) right edge, (top-right) center, and (bottom-left) left edge. (Bottom-right) Excess tin powders were also found near the center of the sample.

To alleviate the non-uniformity, surface defects, and inhomogeneity, the gas flow direction was reversed in the CVD system. As seen in Figure 22a, the reverse gas flow direction forced the evaporated tin to flow down a significantly longer length (2 m) and reach the sample holder from the back. In this setup, the gas flow was far more homogenous and allowed itself to spread evenly by curving from the back to the front surface of the substrate. Various carrier flow rates were tested to examine its effects on nanowire morphology as seen in Figure 47.

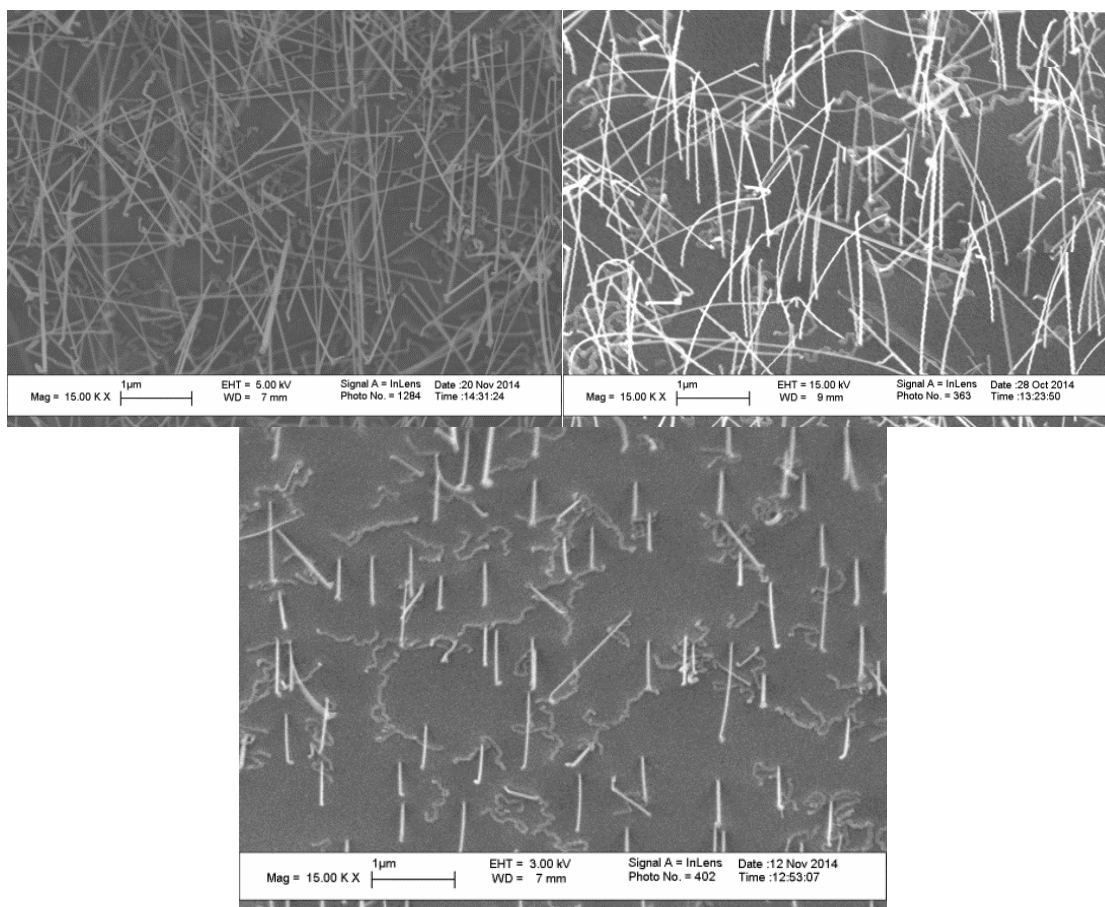


Figure 47: Results of various reverse gas flow rates with (top-left) 10 sccm, (top-right) 20 sccm, and (bottom) 40 sccm.

As seen in the figures, the gas flow rates affected the resulting nanowire densities and lengths. At 10 sccm, the nanowires were fairly dense with 0.30 mL of 40 nm Au colloids. This density was noticeably reduced at the standard 20 sccm flow rate and then further reduced at the 40 sccm flow rate. The nanowire heights were also reduced: 10 sccm resulted in lengths >1 μm, 20 sccm resulted in approximately 1 μm and lastly, 40 sccm resulted in nanowires at about 300 nm. This is likely due to the fact that at higher flow rates, the evaporated tin powder has a shorter time to interact with the substrate surface. Additionally, higher flow rates might induce excess turbulence when the gas hits the substrate in from the back, thereby, lowering the chance for Sn to interact with the Au-seeded substrate. Nevertheless, all the reverse gas flow

rates resulted in highly repeatable, and uniform arrays with no discernable excess tin powders found along the surface. Growths using the reverse gas flow direction showed no obvious variance (<5%) in nanowire density from edge to edge. Further discussion of the uniformity and repeatability due to the carrier gas flow dynamics are found later in the chapter.

3.3.7 Substrate Quenching

In addition to growing the samples directly after annealing, air quenching prior to growth was also investigated. Samples that were annealed and air quenched prior to growth showed a marked reduction in in-plane nanowire growths. To air quench, the CVD system was vented, and the sample holder was immediately pulled out of the furnace and left to cool. Figure 48 shows the nanowire arrays with and without air quenching after annealing.

All samples were synthesized with 40 nm colloids with 30 min of annealing under 20 sccm of reverse carrier gas. In the non-air-quenched sample, significant amounts of in-plane nanowires uniform along the sample can be seen. Conversely, in the air-quenched samples, the nanowire morphologies showed wide-spread reduction in in-plane nanowire growths. Repeated testing showed similar improvements in nanowire arrays in all nanowire densities, as seen in Figure 48. The results seem to indicate that the in-plane nanostructures are forming during the cool down stage and their formation is avoided by quenching.

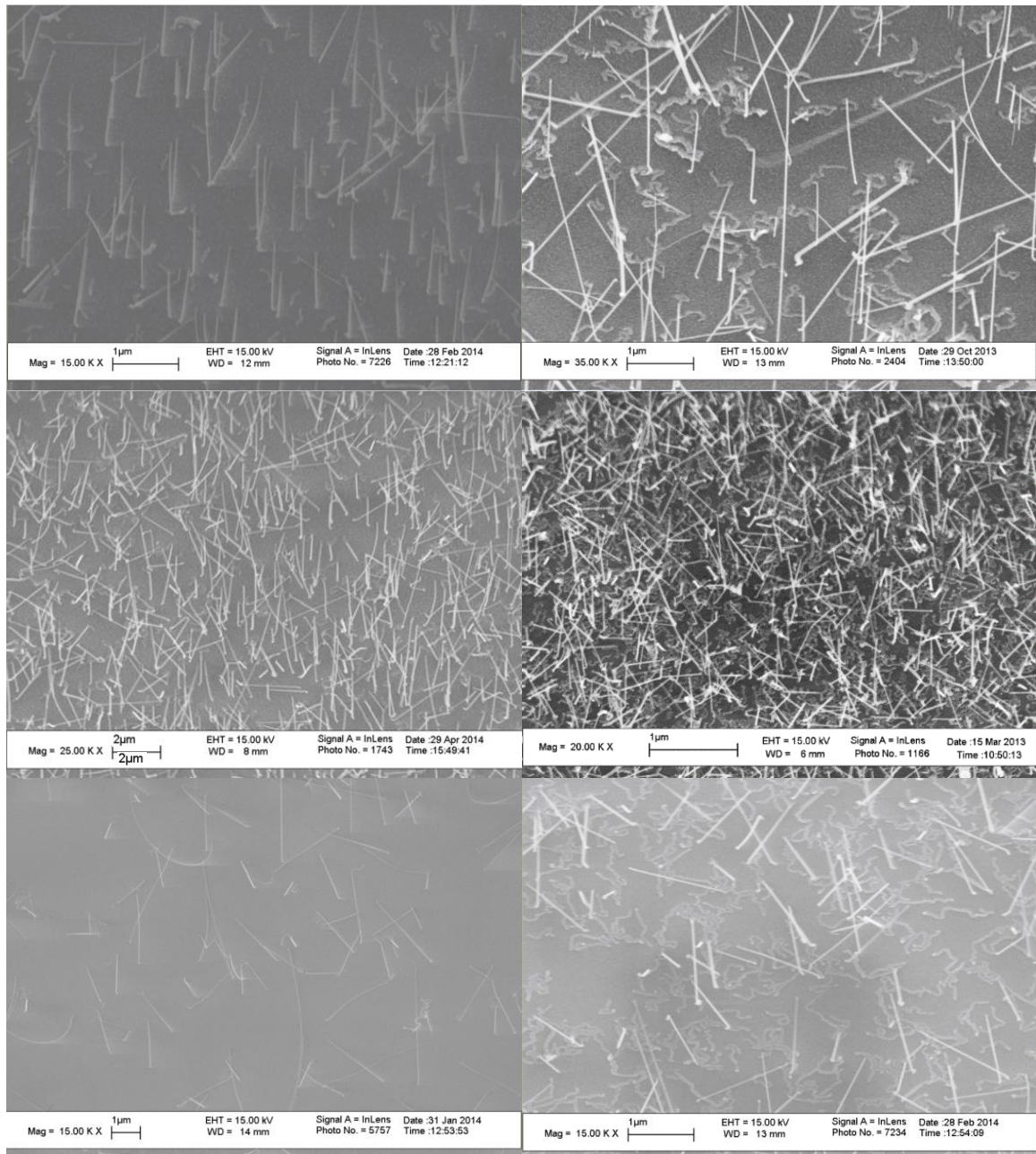


Figure 48: Comparison of various densities of nanowires (left) with and (right) without air quenching. (Top) 25% NW density, (center) 35% NW density and (bottom) 5% NW density

3.4 Colloidal Nanowire Array Uniformity and Repeatability

Comprehensive testing was performed in order to create uniform and repeatable SnO₂ nanowire arrays for thin film deposition applications. As seen in the prior section, several factors were explored including annealing, carrier gas flow rate and direction, and air quenching that resulted in highly reliable nanowire growths. In addition, these optimized factors resulted in massive reduction in surface defects such as in-plane nanowires and conglomerations. The optimized conditions are as follows:

- 1) The colloid solution is stirred for 1 minute and seeded on the substrate.
- 2) The seeded substrate is annealed for 30 min and air quenched.
- 3) The seeded substrate is then re-heated after cooling down and is grown under 20 sccm of reverse flown Ar carrier gas at a substrate temperature of 630 °C and system pressure of 0.50 mTorr for 20 min.

Figure 49 highlights the improvements made from the initial and currently-optimized nanowire growth conditions. When aiming for a moderately dense nanowire array (30-35% effective nanowire density), the optimal conditions led to substantial improvements in nanowire array uniformity along the surface whereas the initial conditions showed wide variances in nanowire density along the length of the sample. Additionally, the optimized samples showed dramatically-reduced deviations in the nanowire densities, with the highest standard deviation at 2.87%. This is due to the improvement in uniformity as well as reduction in surface defects such as conglomerations, excess tin powders and in-plane nanowires. The initial conditions again showed a wide standard deviation range for the nanowire density, up to 11.51%, indicating a lack of sample reliability, and repeatability.



Figure 49: Results from optimized conditions versus initial where (top) optimal conditions show improved reliability and repeatability when targeting NW densities around 30-35% as well as (bottom) reduced growth deviations

With the optimized conditions indicating a high level of nanowire reliability and repeatability, testing was done to determine the effective nanowire density for the amount of colloidal solution for varying colloid sizes. Figure 50 shows a near-linear trend, indicating effective control over the SnO₂ nanomaterial array.

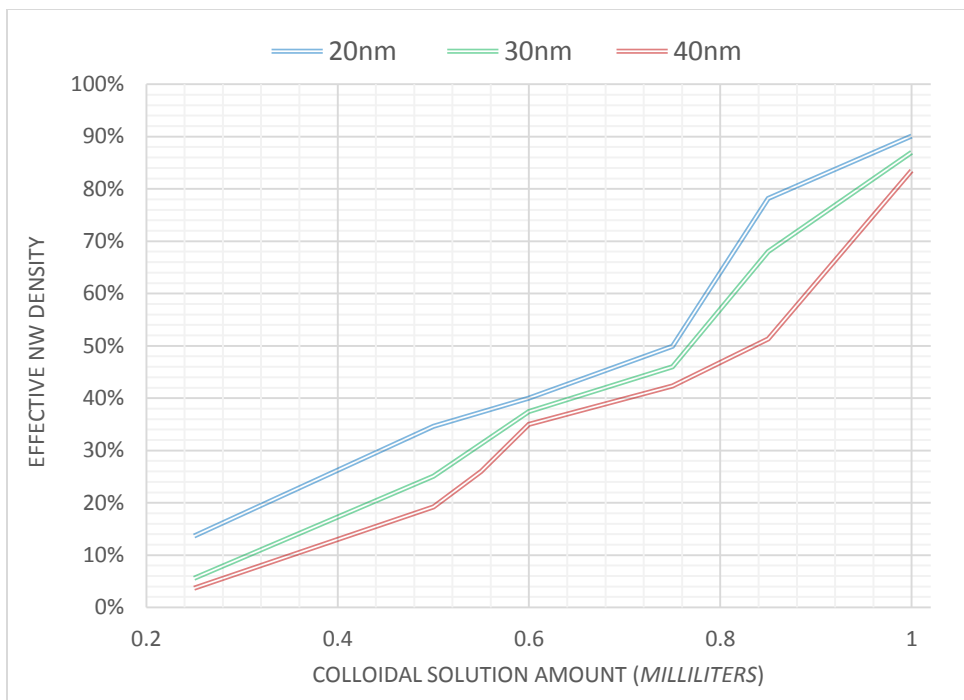


Figure 50: Plot of the effective nanowire density due to colloidal solution amount at various colloid sizes. The optimal conditions allowed for reliable and predictable nanowire growths

3.5 Sputter Coated Nanowire Growth Factors

Sputter coating was investigated as an alternative to colloidal seeding for nanowires. An Au/Pd target was used to form Au/Pd nanocatalysts for the CeO₂ buffers in place of the Au colloids. It is hypothesized the Au/Pd alloy will have lower mobility at high temperatures compared to Au, and thus, reduce the growth of in-plane nanowires. However, sputtering proved difficult in controlling the final morphology of the nanowires since the growths were often too dense for subsequent YBCO thin film growth. The following section explores several growth factors in order to create a proper nanowire material array for YBCO deposition.

3.5.1 Sputtering Time

Differing sputtering times were explored to determine their effects on the nanomaterial morphology and density. However, without a shutter, sputter deposition time was challenging to control. The sputtering times used were 2 s, 4 s, 6 s and 10 s. Figure 51 shows the measured

nanowire density at different deposition times. As expected, the nanowire density increases with higher deposition time, reaching approximately 68% effective nanowire density at 10 s deposition. Interestingly, the nanowire growth at the lowest deposition time of 2 s showed only a 10% drop in nanowire density compared to 4 s of deposition. Additionally, the 4 and 6 s deposition times result in nearly the same nanowire density. Even with extremely short deposition times, sputter coating was unable to create below 30% nanowire densities and usually led to highly dense growths. The corresponding SEM images in Figure 52 verify the density data. Significant in-plane nanowires were also witnessed among all samples whose density increased with increasing deposition time.

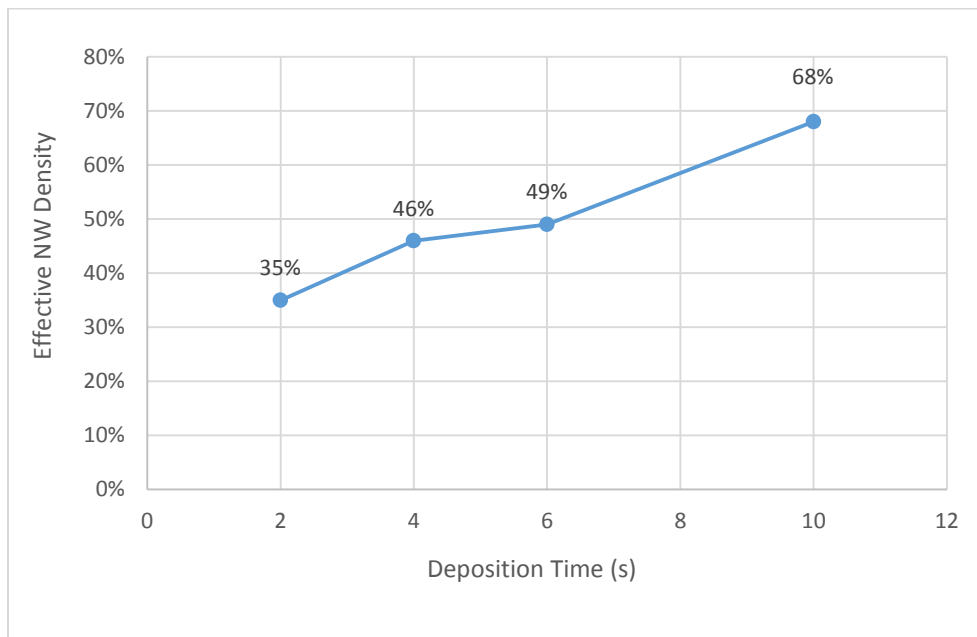


Figure 51: Plot of the densities of nanowire growths at various sputtering lengths

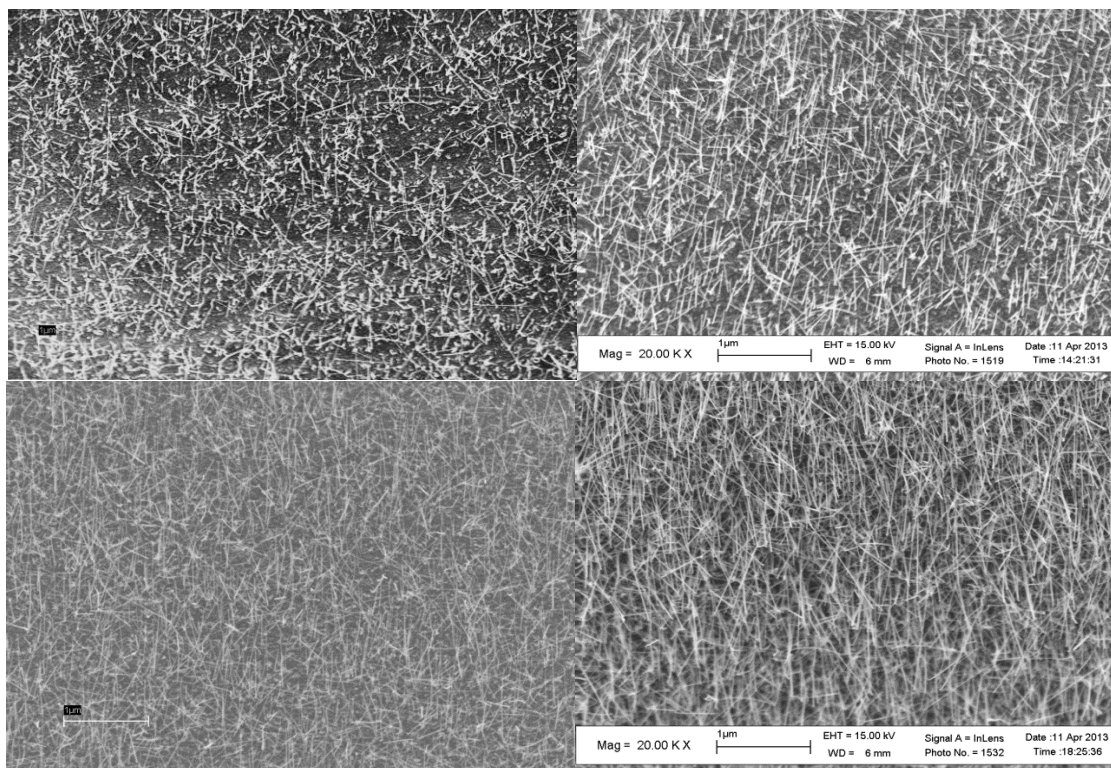


Figure 52: Results of nanowire growth with sputtering times of (top-left) 2 s, (top-right) 4 s, (bottom-left) 6 s, and (bottom-right) 10 s.

3.5.2 Sputter Coat System Pressure

The system pressure during sputter coating was varied, as well, to alter the nanocatalysts deposited on the buffer surface. Modifying the system pressure during sputter deposition directly alters the Ar gas content within the system as increasing the inner system pressure increases the gas partial pressure. Figure 53 shows the SEM images of nanowire grown on samples sputtered with Au-Pd at different pressures for 2 seconds.

At 80 mTorr and higher pressures, the samples showed high nanowire densities with nanowires around 0.5 μm in length and approximately 30 nm in thickness. Lowering the pressure to 60 mTorr resulted in a discernable change in nanowire morphology. The nanowires exhibited an average height of 200 nm and a thickness of 10 nm. Additionally, there was also a 10% drop in the effective nanowire density when compared to samples made at 80 and 100

mTorr. This change in morphology is due to the reduction in the nanocatalysts amount and size, at lower sputter coating pressures. As a result, increased system pressure results in no obvious changes in nanowire morphology and density, but, the lowered sputter coating system pressure leads to shorter and thinner nanowires.

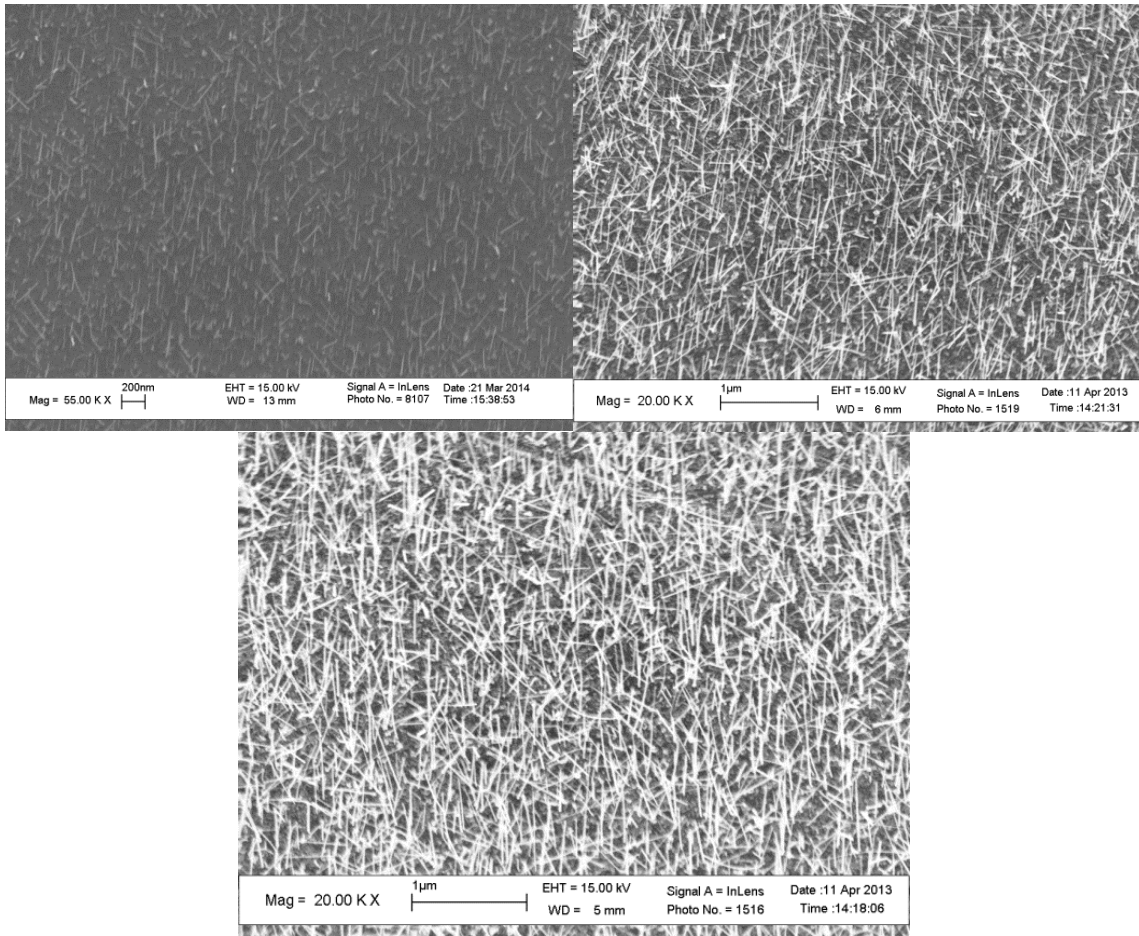


Figure 53: Results of nanowire growths in samples gold sputter coated at pressures of (top-left) 60 mTorr, (top-right) 80 mTorr, and (bottom) 100 mTorr

3.5.3 Growth Time

As in the case of colloid-based nanowire samples, growth time was also investigated for sputter-coated nanowires to determine its effects on nanowire length. Figure 54 shows the results for samples coated with two nanocatalyst morphologies and grown in CVD for 10, 30, and 40 min.

The increase in CVD growth times had the expected effect on increased nanowire length. The samples sputtered at 60 mTorr system pressure showed short (150 nm long) nanowires with an average diameter of 10 nm at 10 min of growth. Increasing the growth time simply increased the nanowire length, with an average length of 300 nm at 40 min of growth. Similar results were seen in the 80 mTorr sputtered samples.. At 10 min of growth, the nanowires averaged at 300 nm in length and a 20 nm in diameter. Increasing the growth to 40 min time saw the nanowire lengths average at 1 μm while remaining at the same diameter.

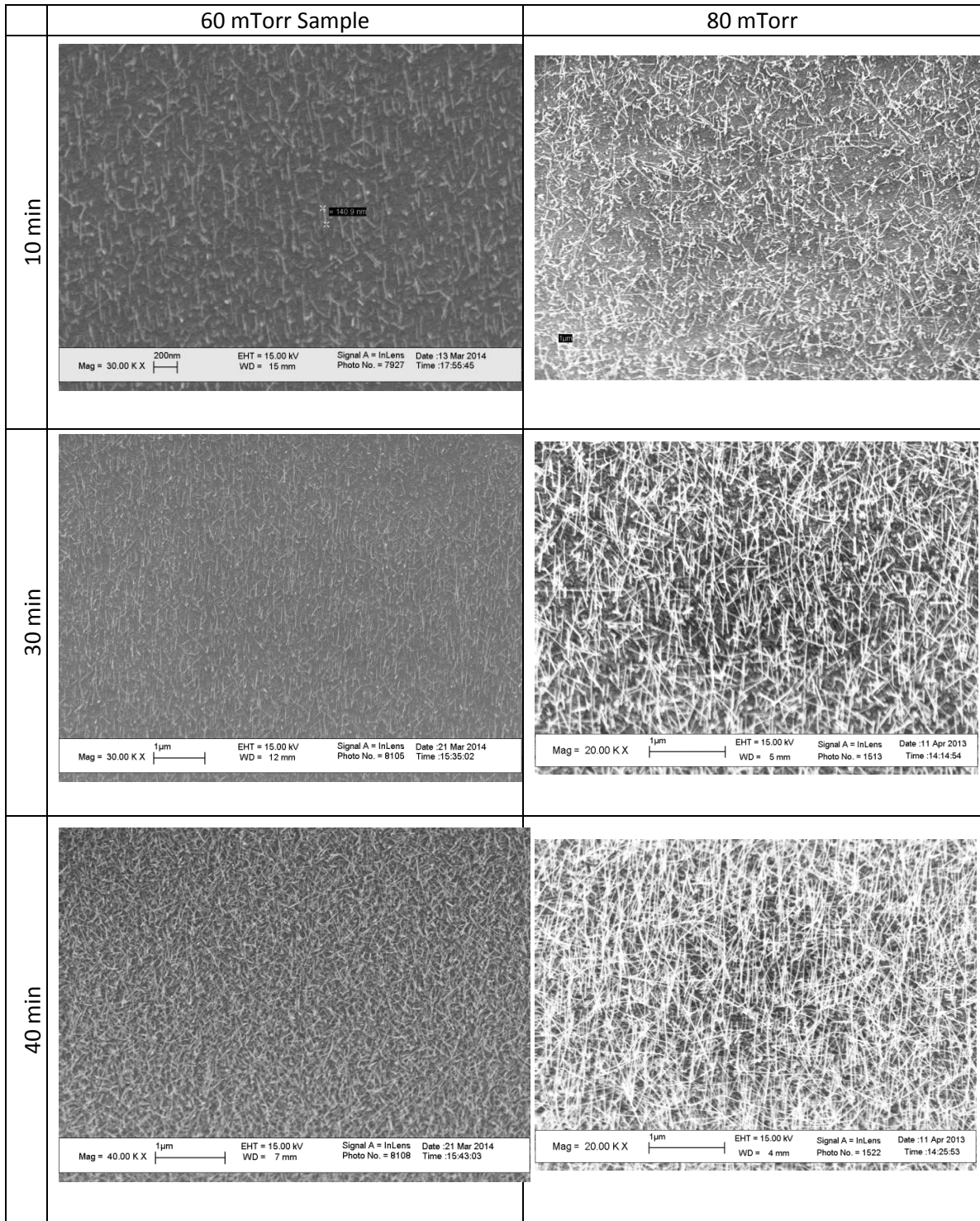


Figure 54: Results of nanowire growth from sputter-coated catalysts at 60 mTorr and 80 mTorr and different growth durations

3.6 Structure Modification by Ion Bombardment

Structure modification by ion bombardment was mainly explored in order to align multi-directional nanowires as well as remove in-plane nanowires. As discussed in Chapter 2, the custom IBAD system using Argon ions was used to explore the viability of post-processing nanowire growths since ion bombardment can provide repeatable and well-regulated density control for the nanowire arrays. Figure 55 shows an example of the effective nanowire densities after ion-bombardment from an optimized run. It is seen that significant amounts of multi-directional nanowires have been removed in a highly predictable method. The factors controlling the ion bombarded nanowire morphologies are discussed in the following sections.

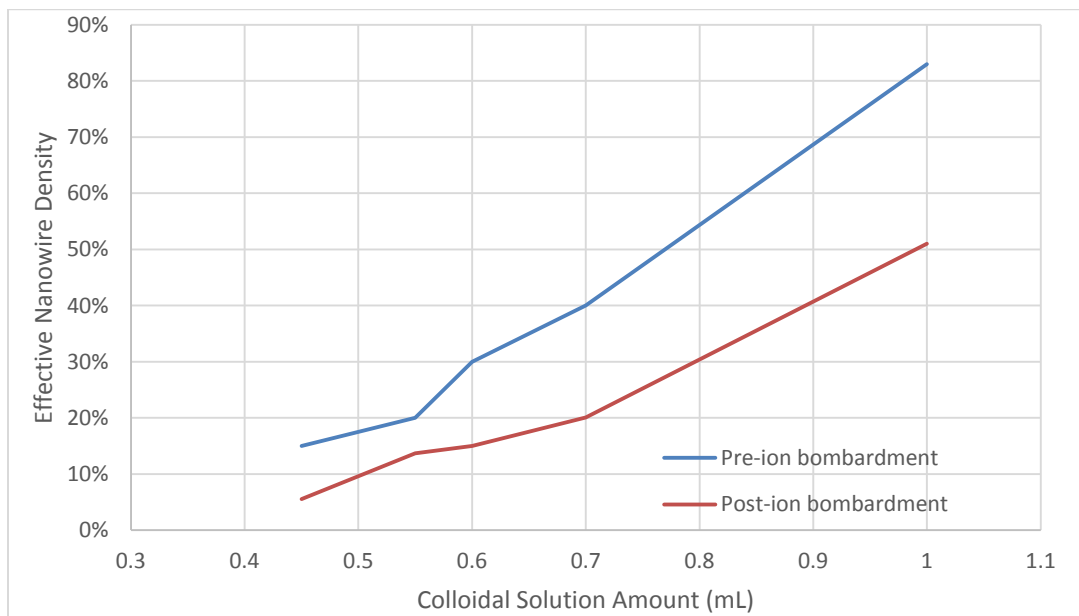


Figure 55: Effective nanowire densities before and after ion-bombardment showing high level of reliability

3.6.1 Beam Energy

One of the primary factors for controlling the nanostructure modification by ion beam bombardment is the applied forward beam energy. Three different energy levels were tested, 30, 40, and 50 W, where 30 W is the minimum energy required to apply the beam and 50 W is the maximum the system can handle before burning the tungsten filament used to create the ion beam. Figure 56 shows the SEM image results for samples with 30% effective nanowire densities bombarded at a reel speed of 22 mm/min.

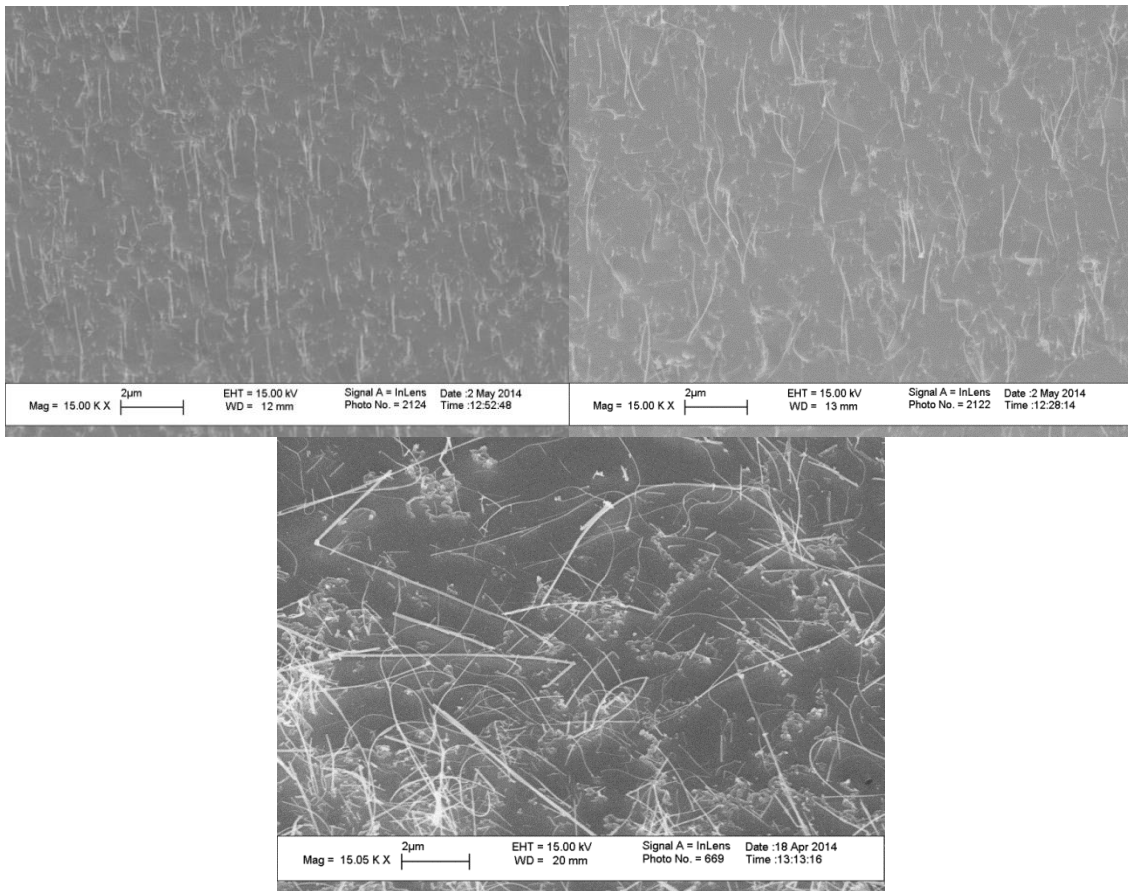


Figure 56: Results from ion-bombardment of samples with nanowires using a forward beam energy of (top-left) 30 W, (top-right) 40 W, and (bottom) 50 W

At 30W, most of the nanowires remaining were aligned vertically, while significant amount of in-plane nanowires were removed. Some out-of-plane nanowires were also removed,

leaving behind a slightly lower density of vertical nanowires. Increasing the beam energy to 40W, the in-plane nanowires saw a similar reduction in density, but, the out-of-plane nanowires experienced bending along the length of the nanowire. The density of vertical nanowires remained similar to the 30W samples; however, some of the nanowires were bent in multiple directions, and formed 'root-like' conjoined nanostructures. Figure 57 shows a close-up SEM image of the 'root-like' structure. At 50W, the entire nanowire array along the sample bent from the base towards the surface of the buffer. While there was in-plane nanowire reduction, most of the vertical nanowires were bent to the surface, resulting in undesired nanomaterial modification.

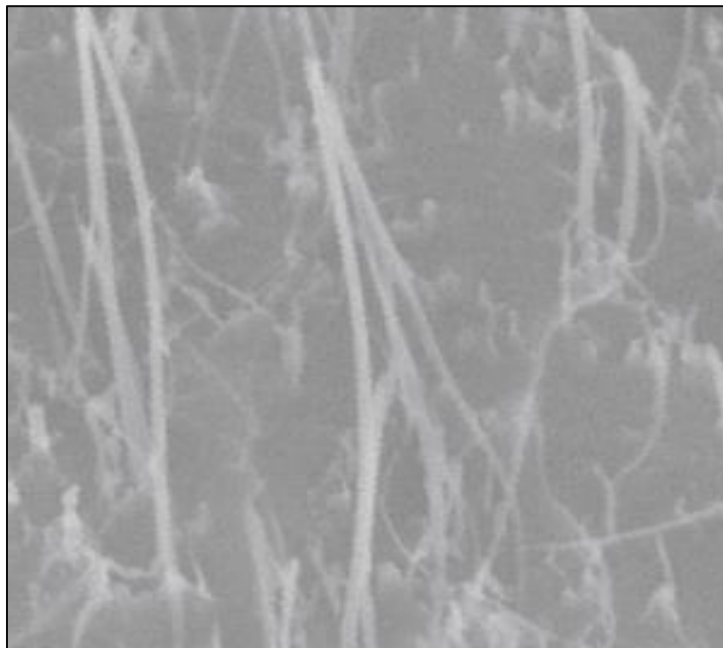


Figure 57: A root-like nanowire formation due to ion-bombardment

Furthermore, the ion bombardment also showed signs of damaging the buffer layer. From 30W to 50W, the buffer layer that was originally green showed a purple tint along the surface after bombardment. XRD analysis was performed to confirm surface layer damage after

bombardment. As seen in Figure 58 below, the intensity of the CeO_2 (200) peak diminished with increasing power levels at 30, 40, and 50W; a significant amount of the buffer layer was removed at 50 W.

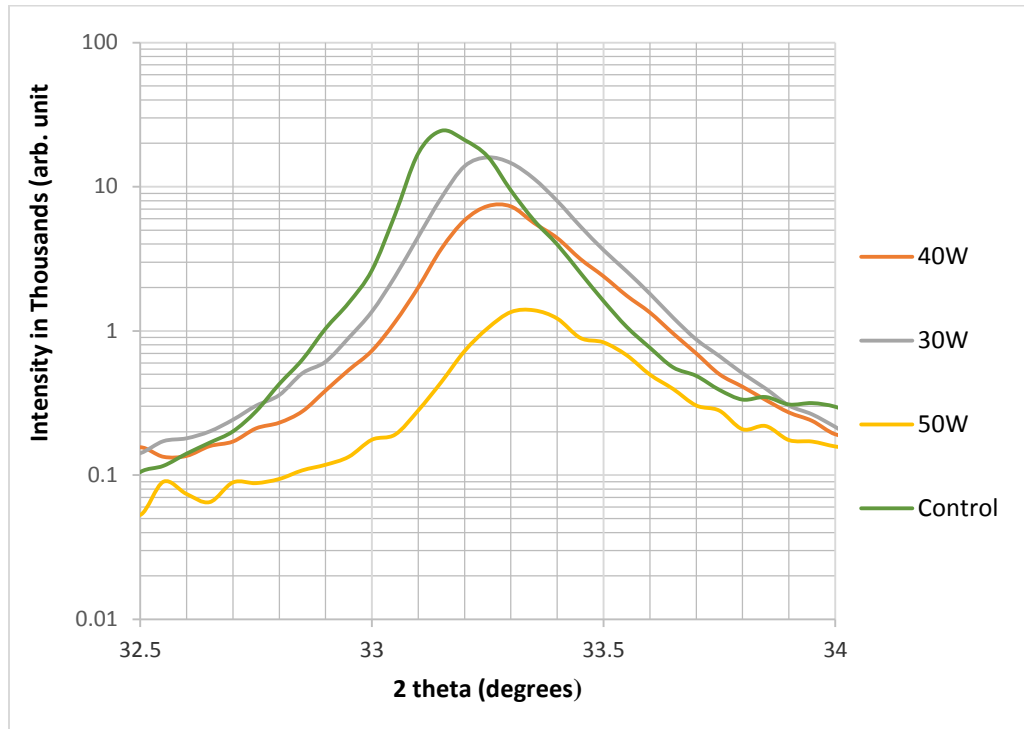


Figure 58: XRD scan of (200) CeO_2 peak showing intensity reduction due to ion-bombardment

3.6.2 Tape Speed

The second major factor controlling the nanowire modification is the tape speed which determines the duration of time the sample is ion bombarded. Sputter-coated and colloidal-coated nanowire samples were both bombarded with 40W of forward energy at speeds of 17 mm/min, 22 mm/min, and 25 mm/min. Figure 59 shows the results for both the sputter-coated and colloidal samples.

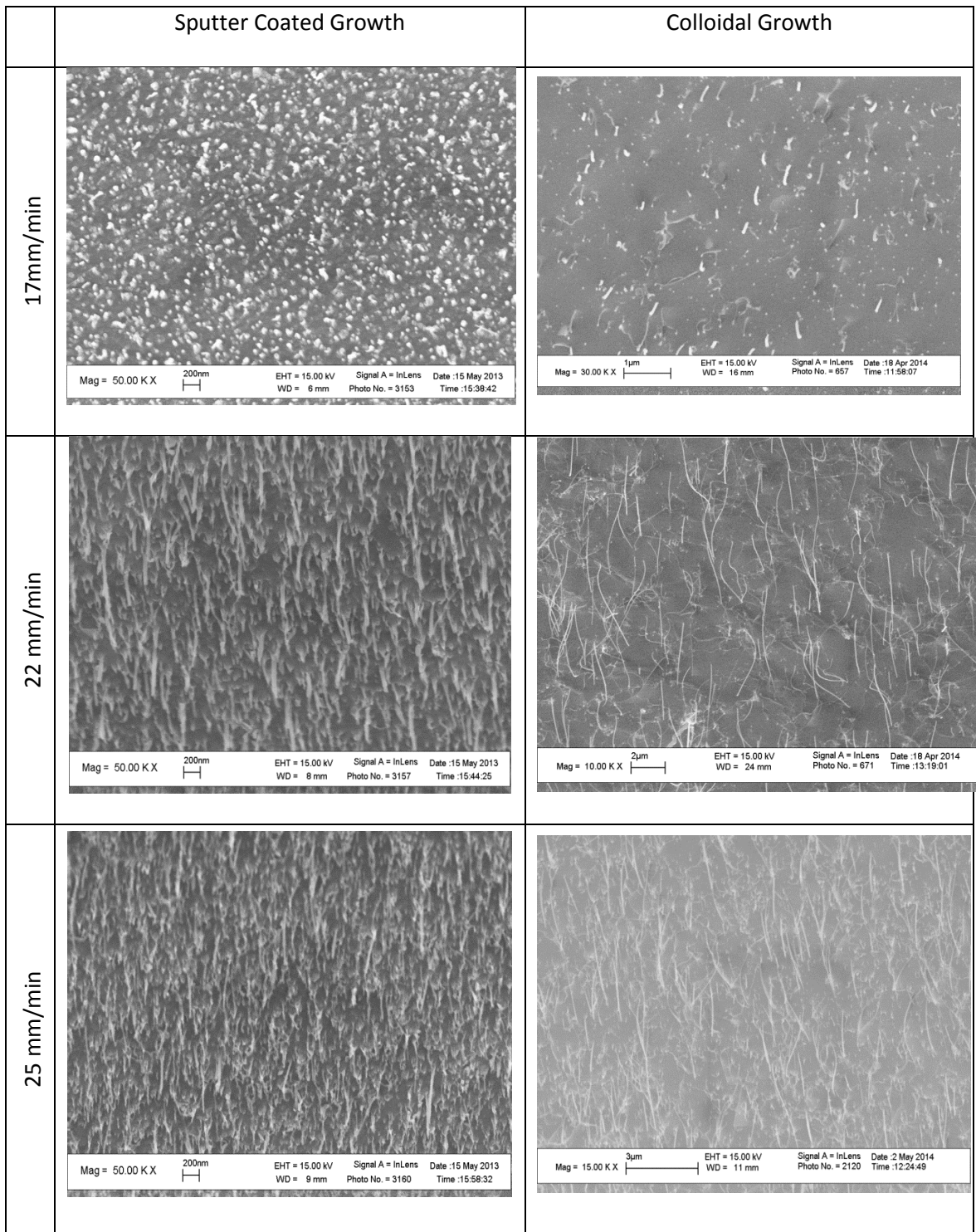


Figure 59: Results of differing nanowire morphologies speeds in colloidal and sputter coated samples after ion bombardment at various tape speeds

At the slowest rate of 17 mm/min, SEM images of both the sputter-coated and colloidal samples showed near complete eradication of all nanowires leaving 100 nm nanodots where the nanowires were once attached. In the colloidal sample, most nanowires were destroyed leaving behind small nanowires that were bent to the surface. The sample surface also showed massive color change going from the original green to deep purple. At a moderate rate of 22.3 mm/min, the sputter-coated and colloidal samples showed significant in-plane nanowire reduction, with adequate nanowire vertical alignment. The sputter-coated sample showed thick nanorods with a substantial amount of shortened nanorods and nanodots due to the ion beam shaving down the nanowires. The colloidal sample showed comparable results under the same conditions. The vertical nanowires were at the same density, but, some experienced bending along the length. Some of the vertical nanowires were also completely bent towards the surface, and others had formed 'root-like' conjoined nanostructures. At the fastest rate of 25 mm/min, the sputter-coated and colloidal samples showed expected results. The sputter-coated sample had a higher density of aligned vertical nanorods, and a lowered density of shaved-off nanodots. The colloidal sample showed highly-aligned nanowires with minimal nanowire bending. Additionally, the in-plane nanowire density was higher than in the 22.3 mm/min sample and fewer 'root-like' structures formed.

As seen in Figure 60, surface damage the different tape speeds was also investigated. At the fastest rate of 25 mm/min, damage was still observed by XRD scans through reduction of the CeO₂ (200) peak intensity. At the slowest rate of 17 mm/min, the SEM image results were confirmed by the significant reduction in the peak intensity in the XRD scan.

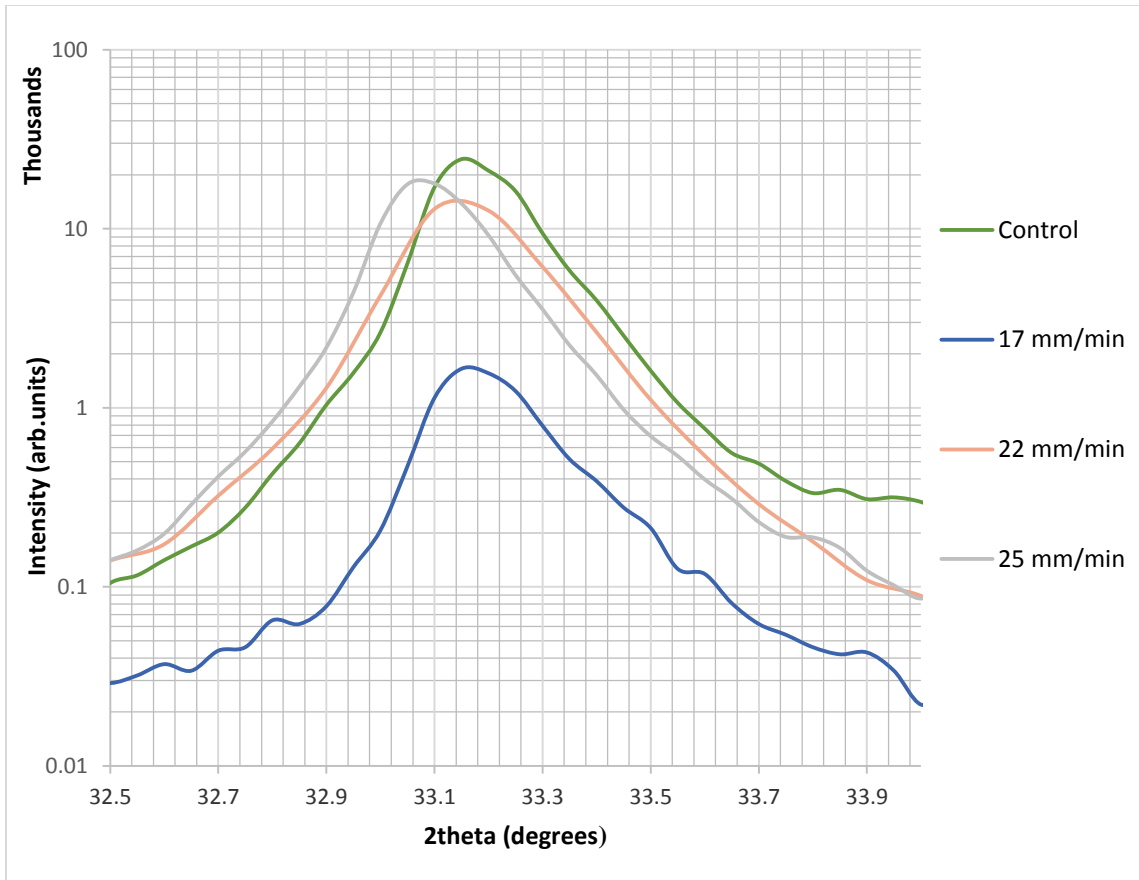


Figure 60: XRD scans of the (200) CeO₂ peak of nanowire samples ion bombardment at 40 W showing material damage at various tape speeds

3.6.3 Microstructure Variance between Sputter-Coated & Colloidal-grown Nanowires after Ion Bombardment

The microstructures of the sputter-coated and colloidal-grown nanowire samples were observed to have discernible differences after ion bombardment. Figure 61 shows the differences between sputter-coated and colloidal-grown samples with similar starting nanowire densities.

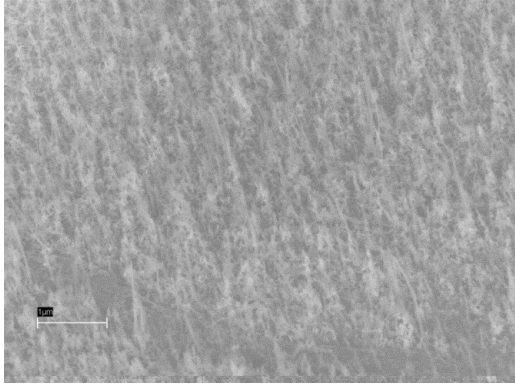
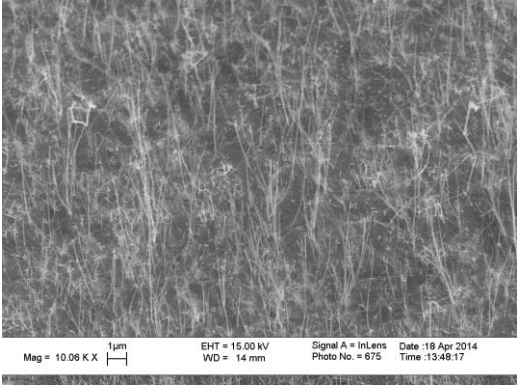
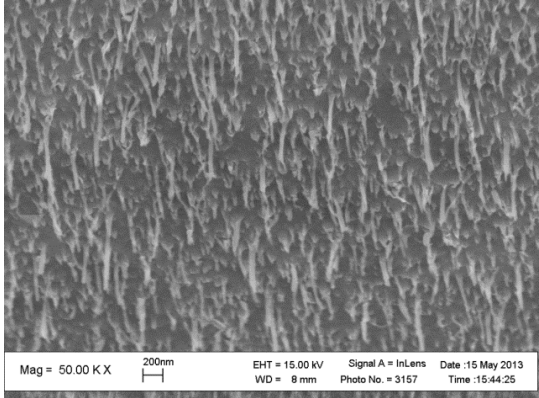
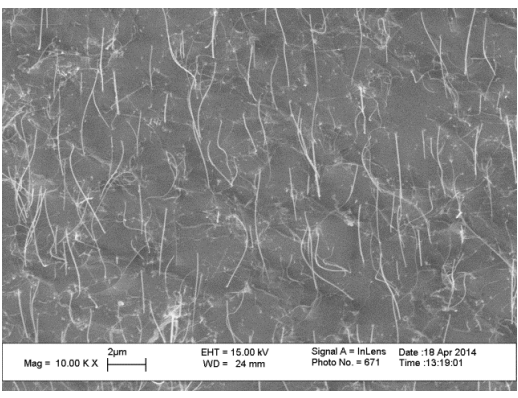
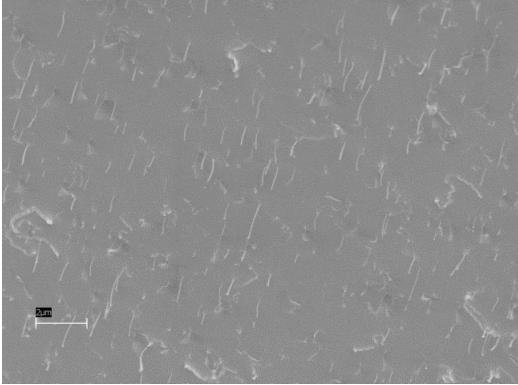
	Sputter Coated Sample	Collidal Sample
83-88%		
38-40%		
15-20%	N/A	

Figure 61: Results of ion bombardment at 40 W on sputter coated and colloidal samples at the same starting densities

With a starting density of 83-88%, the nanowires in the sputter-coated samples converted to thick nanocolumns after ion bombardment. Additionally, the post-bombardment morphology also showed a dense field of 50 nm tall nanostructures that are remnants of removed nanowires. In the colloidal sample at a similar starting density, the nanowire morphology was mostly transformed into a dense field of tip-conjoined 'root-like' nanostructures after ion bombardment. This is likely due to the highly dense nanowire array bending during ion bombardment and joining at the tips. The remaining nanowires were removed or bent along the surface. At a lower starting density of 38-40%, the sputter-coated samples formed a more cohesive array of 80nm vertically-aligned thick nanocolumns, with all in-plane nanowires removed. Some nanowires were removed, leaving behind thick nanodots. In colloidal samples, a significant amount of the nanowires were removed. The surviving nanowires were vertically-aligned, but, experienced bending along the length. Some 'root-like' nanostructures were found, but at much lower densities when compared to the 83-88% colloidal sample.

At 15-20% starting densities, no comparisons could be made since the sputter-coated samples had no starting densities at 15-20%. The colloidal samples were vertically aligned with nearly all in-plane nanowires removed.

3.7 TFA-MOD YBCO Thin Film Synthesis

Superconducting YBCO thin films were successfully synthesized by the TFA-MOD method on flexible CeO₂ buffer tapes using the standard Araki procedure [43]. This work used two TFA-MOD systems to deposit the YBCO thin films on bare substrates and prefabricated nanowire substrates. The following section explores the fundamental processes and optimizations in TFA-MOD YBCO thin film synthesis.

3.7.1 Precursor Synthesis

As detailed previously, to prepare the coating solution for TFA-MOD, hydrated acetates of Y, Ba, Cu were mixed in a 1:2:3 stoichiometric ratio with a 1:1 volume ratio of TFA acid at room temperature. The solution was refluxed for approximately 4 hours under decompression to create a viscous blue liquid. Additionally, methanol was added to create a total metal concentration of 1.52 mol/L. For example, 5 mL of fully refluxed solution will require 25 mL of methanol. The methanol plays an integral part of the final solution composition and YBCO thin film performance. Firstly, it allows for control of the precursor viscosity. It was observed that using more than 25 mL of methanol for a 5 mL of evaporated solution decreased the viscosity of the solution resulting in thinner YBCO films. Correspondingly, at methanol amounts less than 25 mL, the precursor viscosity was increased. Since the crystallized film thickness is proportional to the square-root of the viscosity, the final film thickness was also increased [44]. The thicker films were problematic due macro-cracking issues. Figure 62 shows the cracking that was observed in the final YBCO films due to lowered methanol content. Crack-free films were successfully obtained at 1.52 mol/L precursor concentrations.

Methanol also determined the impurity content within the precursor solution. In the evaporation process, the viscous blue solution is refined multiple times with methanol. The

refluxed solution confines impurities of water and acetic acid (by-products of the TFA reaction with hydrated acetates), thus, methanol was added to replace the impurities within the sticky salt solution. The added methanol was evaporated way in the refining process. In a starting solution containing 25 mL of TFA acid and hydrated acetates, 100 mL of methanol was added per evaporation stage. The final highly-purified coating solution had a strong concentration of metal trifluoroacetates and an impurity content of 0.20-0.40 wt% water and 0.50-1.80 wt% acetic acid. The precursor solution was spin coated on to a substrate for 120 s at 4000 RPM with a 12 s ramp up. The 4000 RPM spin rate resulted in a final crystallized film thickness of 200 nm. Lower spin rates were avoided since they led to thicker films and thus, film cracking.



Figure 62: Surface cracking due to thick YBCO films caused by lowering the methanol content in the final precursor solution

3.7.2 TFA-MOD YBCO Growth Mechanism

In the first heat treatment process, the TFA-MOD coated films are calcinated to form a Y-Ba-O-F film with CuO nanoparticles. As detailed in Chapter 1, during calcination, the metal trifluoroacetates are decomposed and nearly all carbon content is expelled to create a

transparent thin film layer on the flexible buffer. The Y and Ba atoms in the film form an amorphous matrix with the free oxygen and fluorine atoms, whereas Cu bonded only with the oxygen atoms. Figure 28 shows the standard Araki heating profile used during calcination. Initially, the samples are ramped up to 200 °C in a dry oxygen environment in order to absorb any residual moisture in the film. At shorter ramp up times (15-30 min), the samples often cracked. However, at lengthened ramp up times of up to 60 min, reliable crack-free growth was seen. In the second ramp, the sample was slowly raised to 400 °C in an approximately 18 hour process. The longer process time is typical of organic chemical reactions that are required to break covalent bonds. At above 200 °C, humidified oxygen was used in order to prevent Cu sublimation [44].

Careful attention was given to the length of the calcination process, as well. Calcination durations less than 18 hours in our MOD systems resulted in incomplete calcination of the film. The films resulted in poor YBCO growth performance, likely due to incomplete removal of carbon impurities in the film [45]. The poorly-calcinated film also took on a burnt surface appearance after crystallization, due to the burnt black oxide powders. Seen in Figure 63, at calcination durations much greater than 18 hours, excess CuO nanocrystallites start to form. This is because Cu TFA in the precursor film has ionic bonds with copper and oxygen. As the Cu TFA salt is removed in the calcination process, the copper will attach to oxygen, leading to large amounts of CuO nanocrystallites at longer calcination durations. During crystallization of the films calcinated for long durations, the CuO-rich film will agglomerate into large isolated CuO grains, vastly degrading the YBCO growth performance.

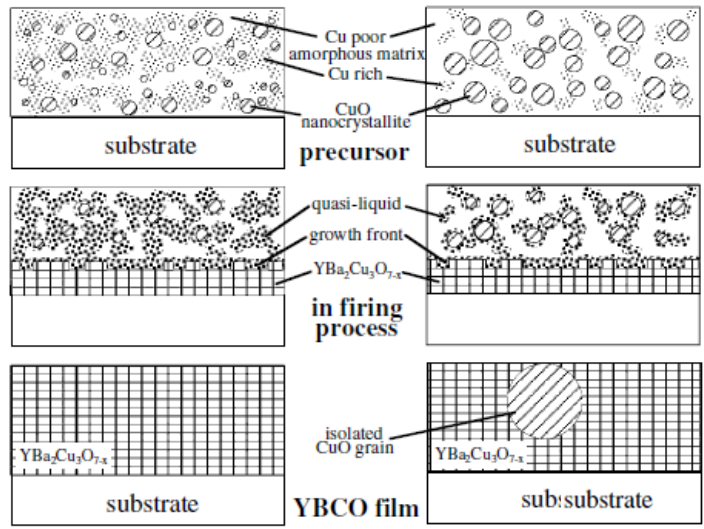


Figure 63: Diagram of (left) proper calcination duration leading to no CuO grains in the final crystallized film and (right) over-calcinated film lead to precipitation of large isolated CuO particles [43].

After cooling down to room temperature, the amorphous matrix of Y-Ba-O-F with CuO nanoparticles is re-heated for crystallization to form YBCO. The standard Araki crystallization profile used is seen in Figure 29. Instead of dry oxygen, a dry argon/oxygen gas mixture with 1000 ppm of oxygen is used in order to control oxygen content within the reaction zone. This is because the chemical reactions on the thin film interface need to stay rate-limited under mass transport mechanism where the amount of incoming oxygen determines the growth rate of the film. Excess oxygen will lead to growth that is rate-limited by chemical reaction rates and early precipitation of undesirable secondary phases such as $BaCu_2O_3$. In the first phase, the furnace is ramped rapidly above 750 °C where above 100 °C, humidified gas is again used. Without humidified gas, YBCO growth is nearly non-existent. This is due to the humidified gas' role in removing fluorine atoms and creating the quasi-liquid YBCO growth interface. In the quasi-liquid interface, a mixture of Y, Ba, Cu, O, H, F atoms move with high mobility. At high temperatures, water vapor attracts the fluorine atoms, creating HF gas that is exhausted out of the system. The remaining atoms, rate limited due to the oxygen content, form perfectly oriented c-axis YBCO grains from the bottom-to-top due to the quasi-liquid. Formation of misoriented (a/b axis)

grains begin due to any excess CuO nanoparticles, improper crystallization temperature and durations, and lastly, humidity. Once the a/b-axis grains form, the quasi-liquid interface promotes misoriented and the regular c-axis grain growth [43]. After 150 to 270 min of crystallization at 750 to 770 °C, dry gas is again used while the furnace cools down. The quasi-liquid interface starts to solidify and stably forming YBCO. Dry gas is used to prevent water vapor from attacking the surface and forming Ba(OH)₂ particles. Figure 64 shows the SEM image of a fully-formed YBCO thin film on a flexible CeO₂ buffer tape. The following sections explore the major factors controlling YBCO thin film performance.

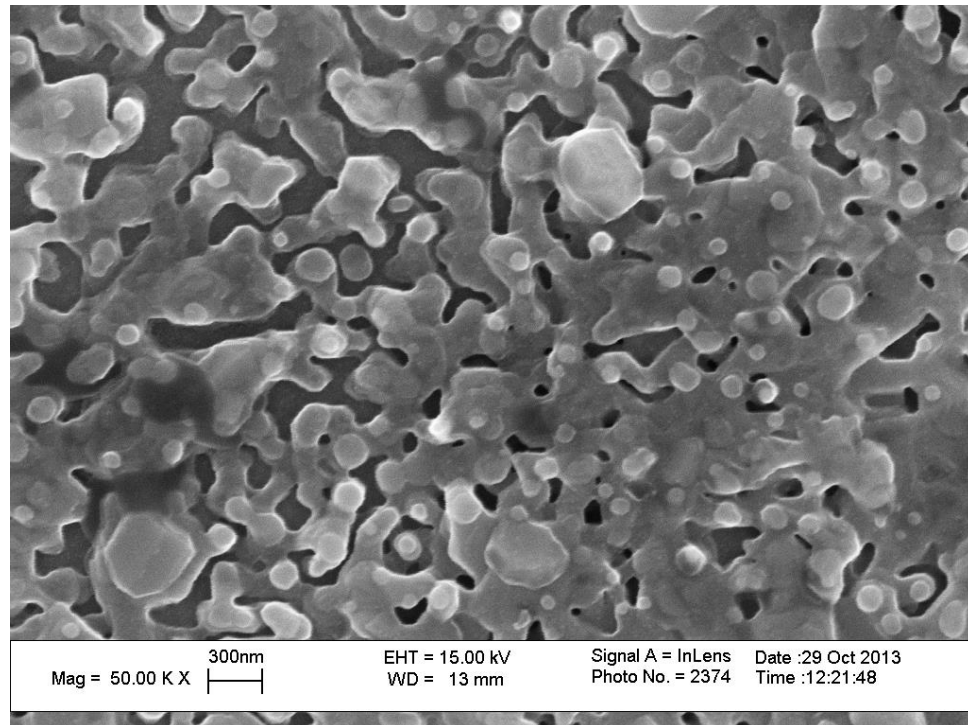


Figure 64: SEM image of a crystallized YBCO films on CeO₂ buffer tapes showing proper c-axis grain growth

3.7.3 Growth Factors

3.7.3.1 Barium Content

Standard TFA-MOD synthesis procedures use a 1:2:3 stoichiometric ratio of Y:Ba:Cu; however, deviations from the 1:2:3 ratio for barium during the precursor synthesis has been seen to yield higher T_c and I_c performance due to excess barium forming secondary phases prior to YBCO growth [49][46]. Table 3 summarizes the differing barium ratios used to grow the YBCO thin films.

Table 3. Barium Content in TFA-MOD Precursor

Sample		In Precursor		
Element		Y	Ba	Cu
101	Percent	16.7	33.3	50.0
	Ratio(Y=1)	1	2	3
102	Percent	18.2	27.3	54.5
	Ratio(Y=1)	1	1.5	3
103	Percent	17.2	31.0	51.7
	Ratio(Y=1)	1	1.8	3
104	Percent	18.9	24.5	56.6
	Ratio(Y=1)	1	1.3	3

In Figure 65, on average, the precursor compositions containing a stoichiometric ratio of 1:1.8:3 yielded the highest T_c . In I_c measurements, the films made with 1:1.8:3 precursor batches consistently performed at 6 to 8 A, whereas, the films with a standard 1:2:3 ratio showed an average performance of 2A.

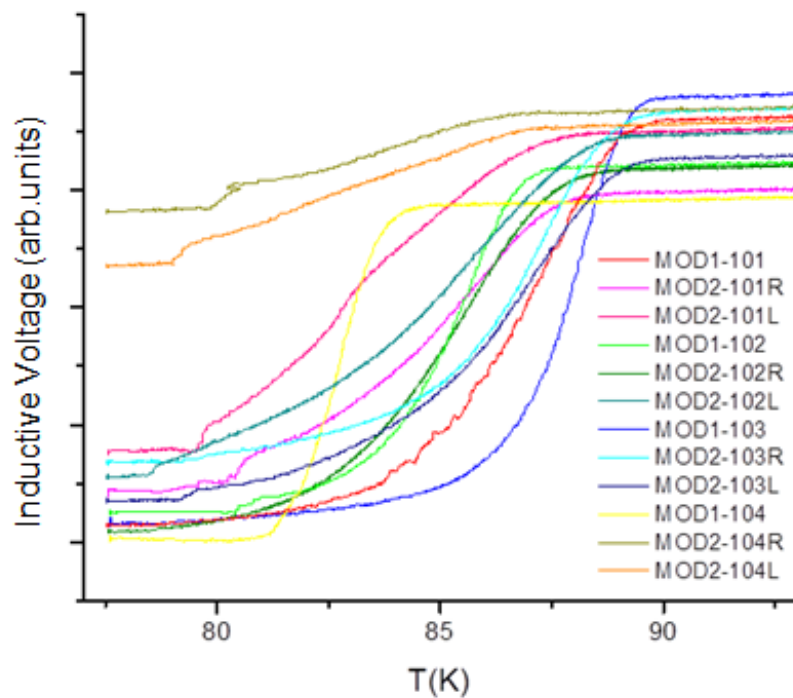


Figure 65: Critical temperature (T_c) measurements on MOD samples made with differing barium content in the precursor solution where a sample designated with R and L refer to the right and left positions, respectively, on the MOD 2 sample holder

Figure 66 shows the results from integrated GADDS data. The films made in MOD101 with standard precursor composition showed higher intensities of (001) and (005) YBCO peaks, but also displayed a strong BaCu_2O_3 peak, showing the existence of secondary phases due to excess barium. The MOD103 sample with the optimal barium ratio showed relatively strong YBCO peaks especially in (002) and (003), but had no BaCu_2O_3 secondary phases present.

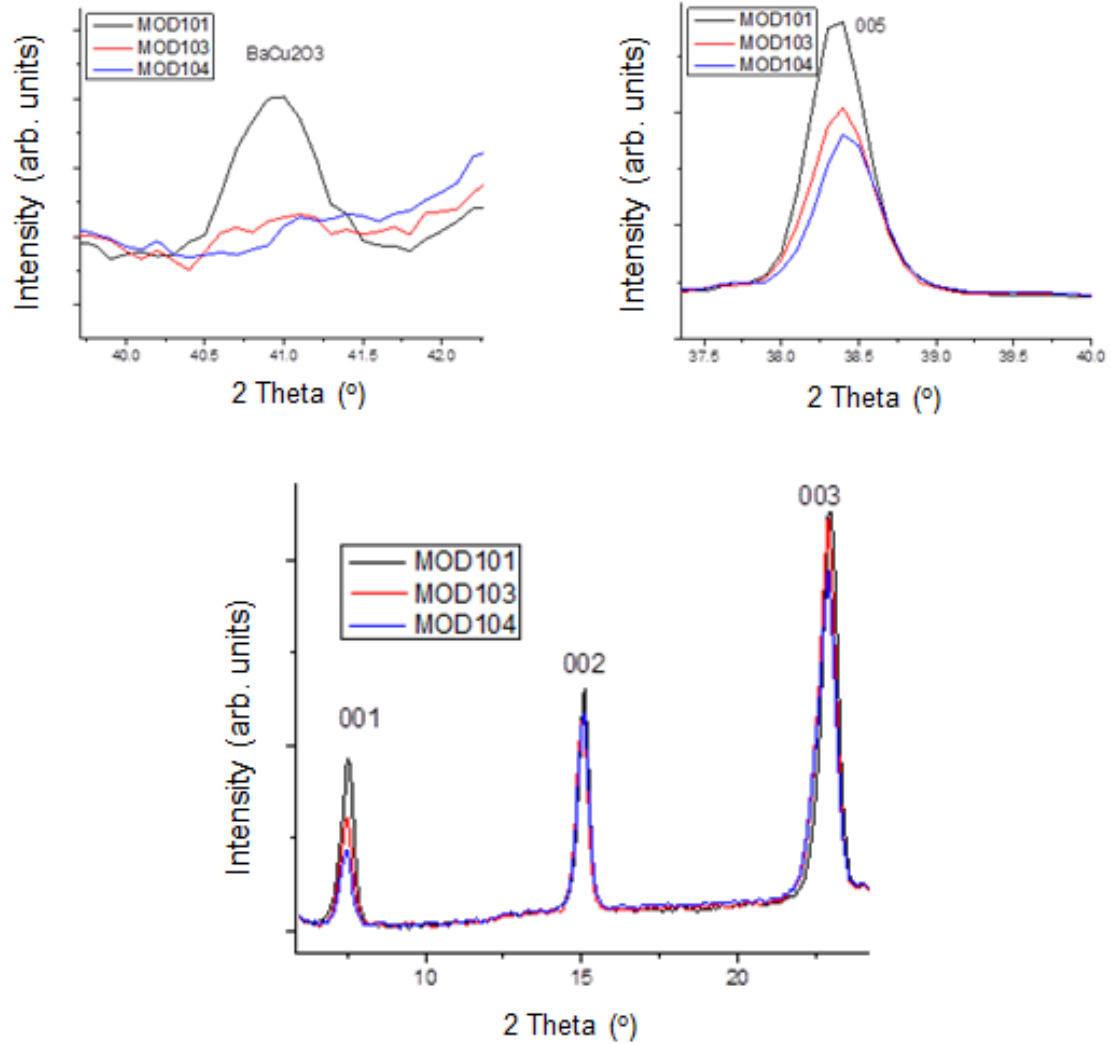


Figure 66: Integrated GADDs results obtained from MOD samples with various barium content

3.7.3.2 Crystallization Duration

Crystallization duration was explored in order to optimize YBCO formation from the decomposed amorphous precursor film after calcination. The standard 1:2:3 stoichiometric ratio was used for the precursor synthesis and was grown under 750 °C crystallization temperature and 4.2% relative humidity. As seen in Figure 67, among the crystallization durations of 270, 210, 180, 150 min tested, the films made at the shortest crystallization time exhibited the highest T_c values. The integrated GADDs measurement results reveal superior YBCO formation across all

peaks in the sample crystallized for 150 minutes. The 270 and 210 min samples showed the weakest YBCO peaks. It is important to note however that the low peak intensity in the 180 min sample, MOD 93-1, is probably due to the thinner film due to reduced viscosity of the precursor as a result of extra methanol used. Its T_c measurement value nonetheless follows the trend of reduced T_c with longer crystallization times, where it performs only slightly behind the 150 minute sample.

The crystallization time of 150 minutes yielded the highest I_c performance as well. The I_c measurements for other durations were $<5A$ while the 150 min duration resulted at $9A$. Figure 68 shows the microstructural differences between all the samples. The 150 and 180 min are virtual indistinguishable from the surface SEM scans. However, the 210 and 270 min samples show increased levels of film cracking due to thermal shrinkage as well as increased level of excess CuO nanoparticles, as noted by the white dots on both images. The excess CuO nanoparticles were caused by CuO agglomeration due to excess crystallization durations.

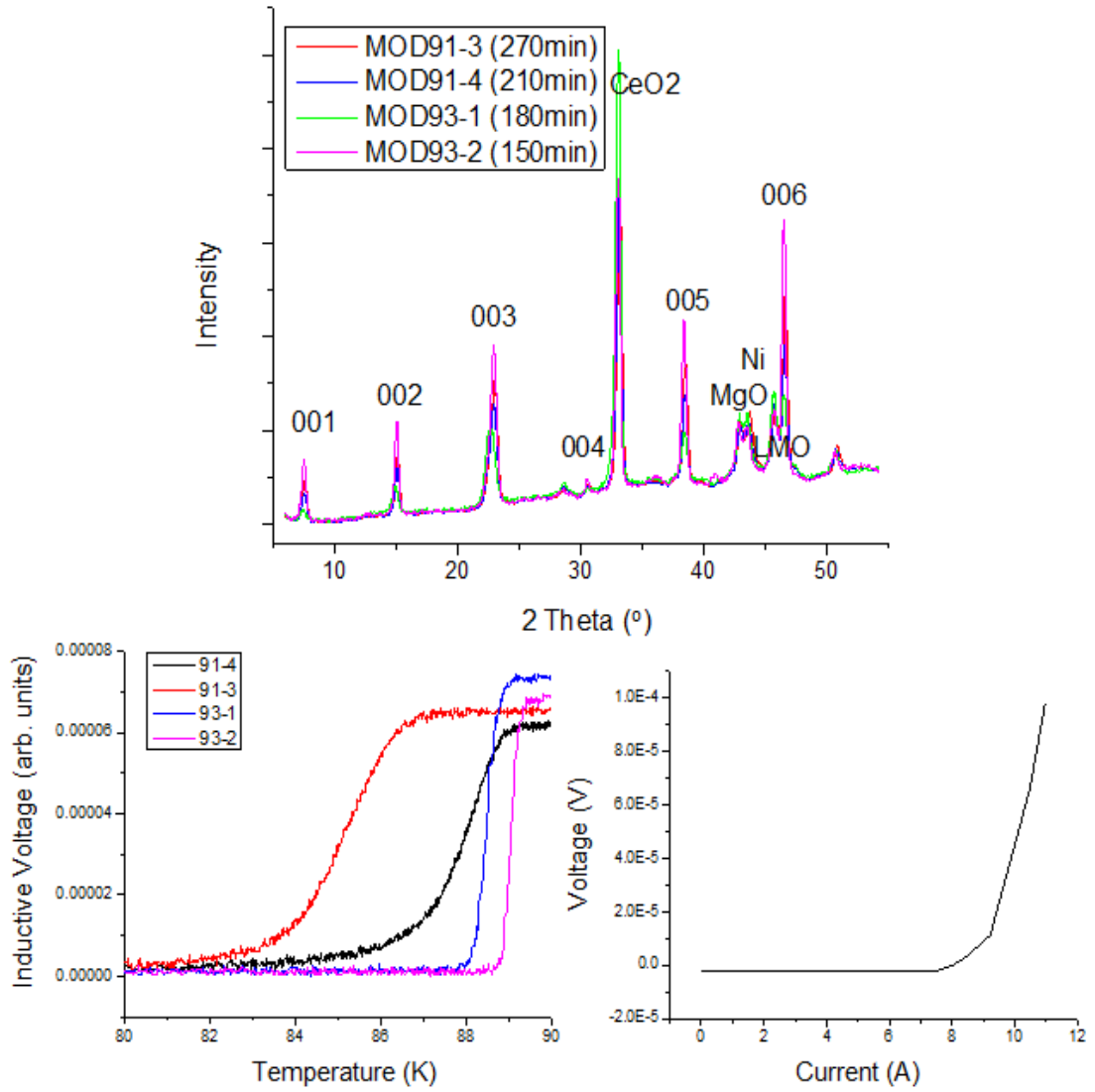


Figure 67: Integrated GADDS and T_c results from MOD samples with differing crystallization times along with a current-voltage curve from the 150 min crystallization duration sample

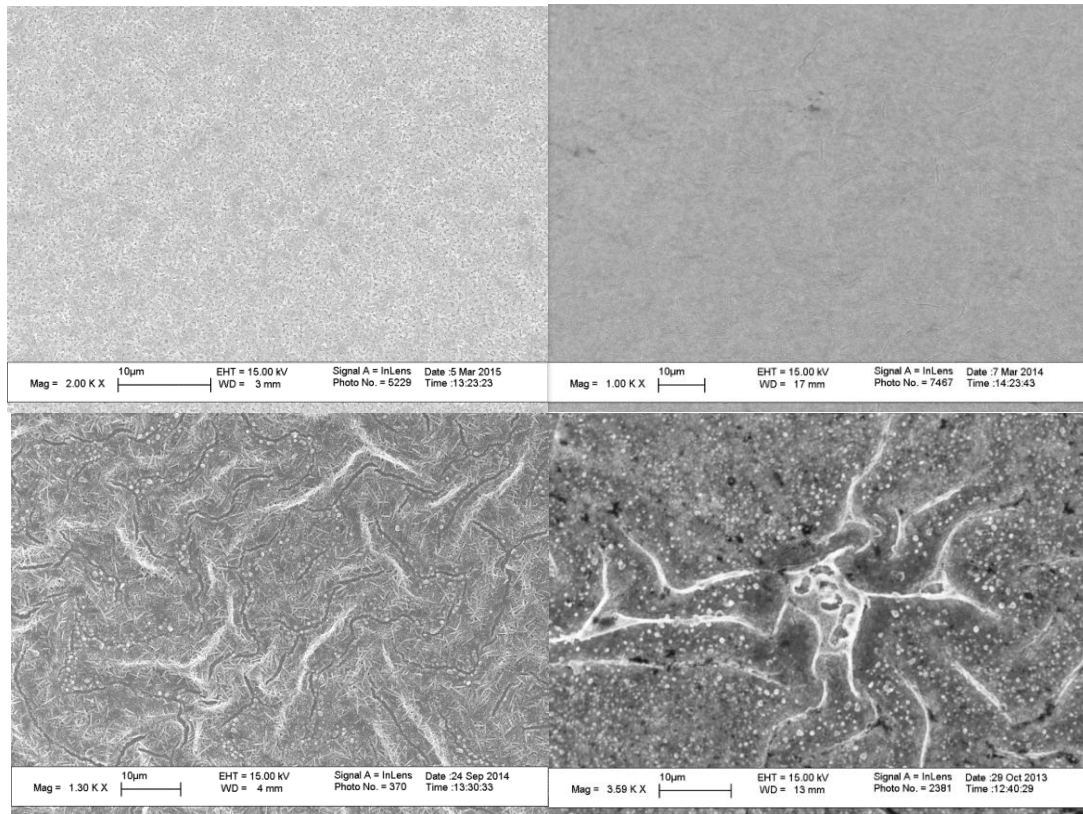


Figure 68: SEM results for MOD samples crystallized for (top-left) 150 min, (top-right) 180 min, (bottom-left) 210 min, and (bottom-right) 270 min.

3.7.3.3 Crystallization Temperature

Crystallization temperature was similarly tested in order to improve YBCO thin film performance, as it controls the growth of the unwanted *a/b*-axis grains, as well as, any secondary phases. TFA-MOD samples were created with the 1:1.8:3 precursor composition at crystallization temperatures ranging from 750 °C to 770 °C in MOD 2 under a crystallization time of 150 min and 9.4% relative humidity. Figure 69 shows the results of T_c measurements for the various samples.

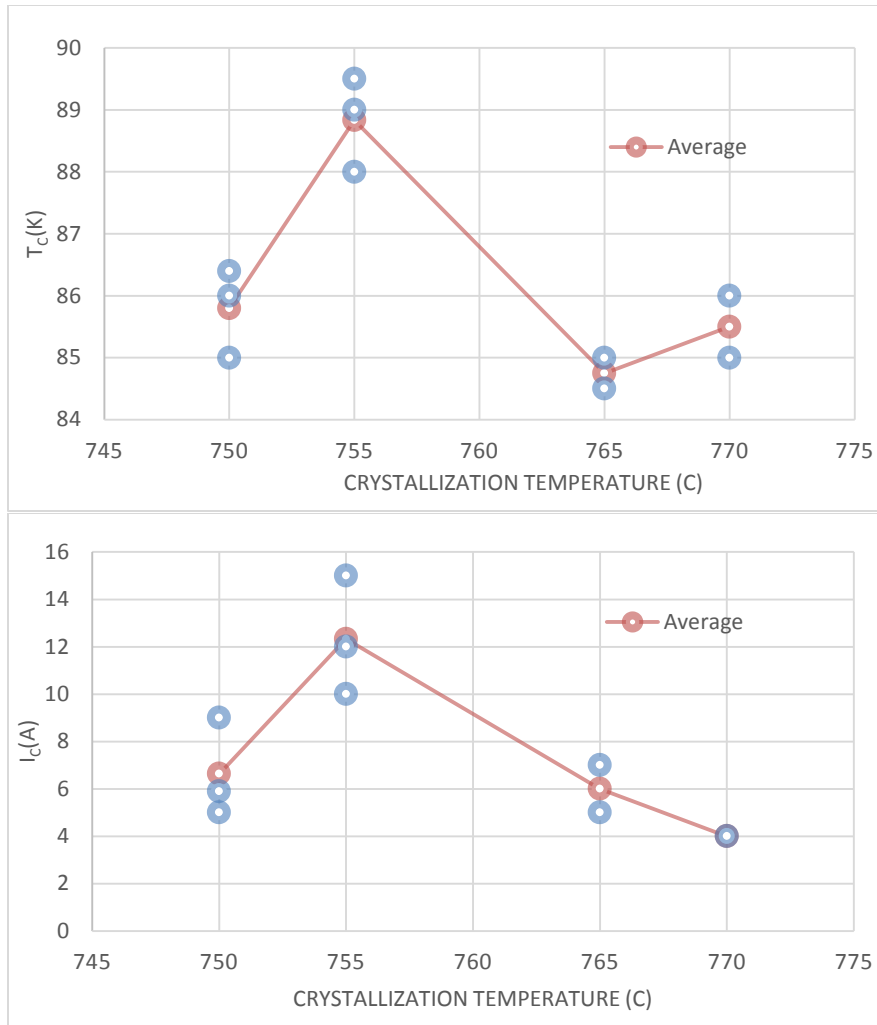


Figure 69: T_c and transport I_c performance of MOD films processed at various crystallization temperatures. The 755 °C samples consistently yield the best performance

As seen from above, TFA-MOD samples processed at a crystallization temperature of 755 °C consistently yielded higher T_c and I_c performance on the flexible CeO₂ buffers. The 755 °C samples yielded J_c of approximately 0.6 MA/cm². There was a drop off in performance at higher temperatures, especially at 770 °C. Figure 70 shows the microstructure of the films made at different crystallization temperatures.

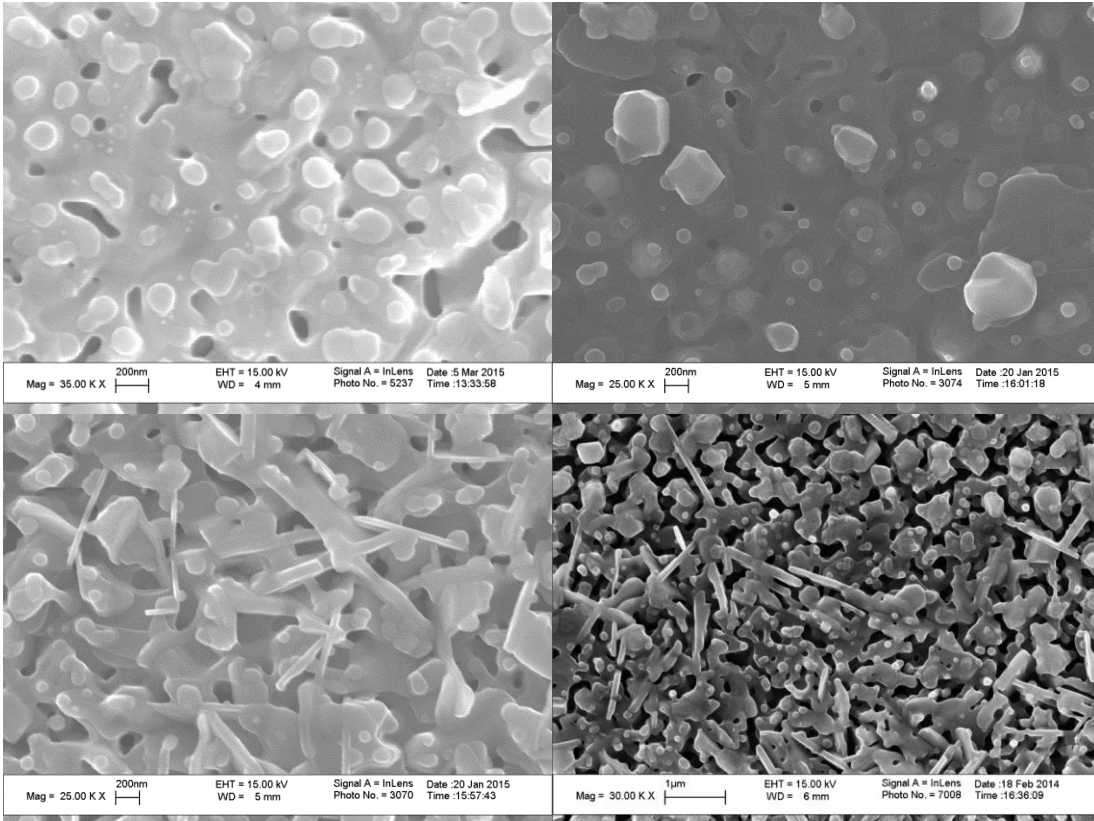


Figure 70: SEM scans of samples prepared at crystallization temperatures of (top-left) 750 °C, (top-right) 755 °C, (bottom-left) 765 °C, and (bottom-right) 770 °C

The SEM microstructure images of the 750 °C and 755 °C samples showed well-aligned c-axis YBCO grains indicative of higher performing YBCO films. The 755 °C sample distinctly showed enhanced grain growth due to reduction of porosity compared to the 750 °C sample. Increasing the crystallization temperature to 765 °C and 770 °C resulted in proliferation of a/b-axis grains. This is likely due to the higher crystallization temperatures increasing the a/b-axis grain growth rate higher than the quasi-liquid interface's reaction [43].

3.7.3.4 Relative Humidity

One of the more critical factors in proper YBCO thin film growth in TFA-MOD systems is the humidity content. Thus, using multiple humidity sensors, humidity content was investigated

within the furnace systems. Figure 71 shows an example relative humidity plot from the sample position.

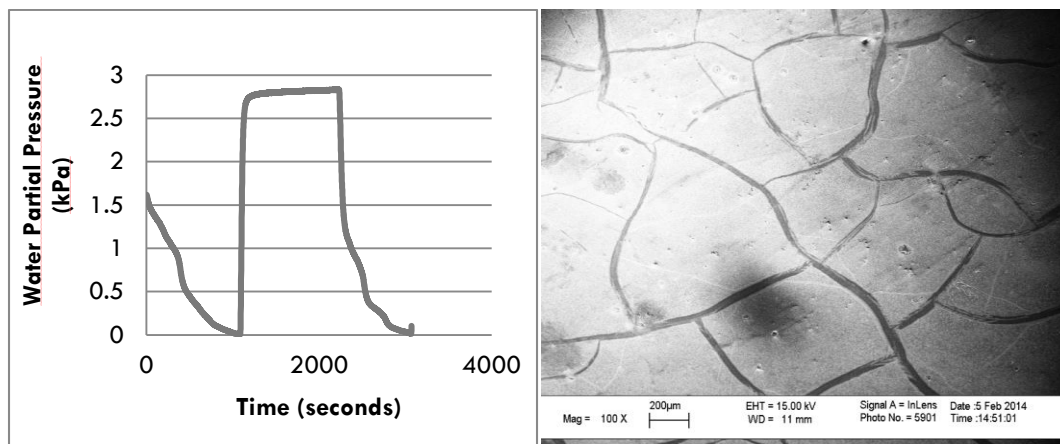


Figure 71: (Left) Example plot of humidity sensor measurements from the sample position. (Right) SEM image of cracked sample surface due to insufficient humidity content in the furnace system.

In the calcination stage, humidity content played a crucial role in eliminating film cracking. For instance, insufficient humidity levels resulted in large cracks along the surface of the film. In MOD2, the bubbler was set to 45-50 °C in order to provide 9.4%-12.3% relative humidity to the system. Figure 71 shows the images of cracked films grown at 4.2% relative humidity due to approximately 10 °C lower bubbler temperatures. Since MOD1 was a smaller system (2.54 cm quartz tube), its bubbler was set to 30 °C to provide 4.2% relative humidity for similar crack-free films. If bubbler temperatures were set to 20-25 °C (2.1-3.2% relative humidity) in MOD1, calcination led to cracked films. Increased bubbler temperatures during calcination in either MOD system had no apparent effect on thin film performance. However, it was undesirable to use higher humidity levels since water would condense in the exhaust end of the tubes.

Furthermore, during crystallization, humidity content as well as duration was vital in eliminating cracked films and reducing a/b-axis grain growth. Figure 72 shows the results of

MOD growths due to varied humidity durations during crystallization. To control moist gas durations, the moist to dry gas switch was either delayed or switched earlier in the crystallization cool down profile. For a longer duration, the moist gas was switched to dry was performed at 600 °C, leading to a 210 min crystallization duration.

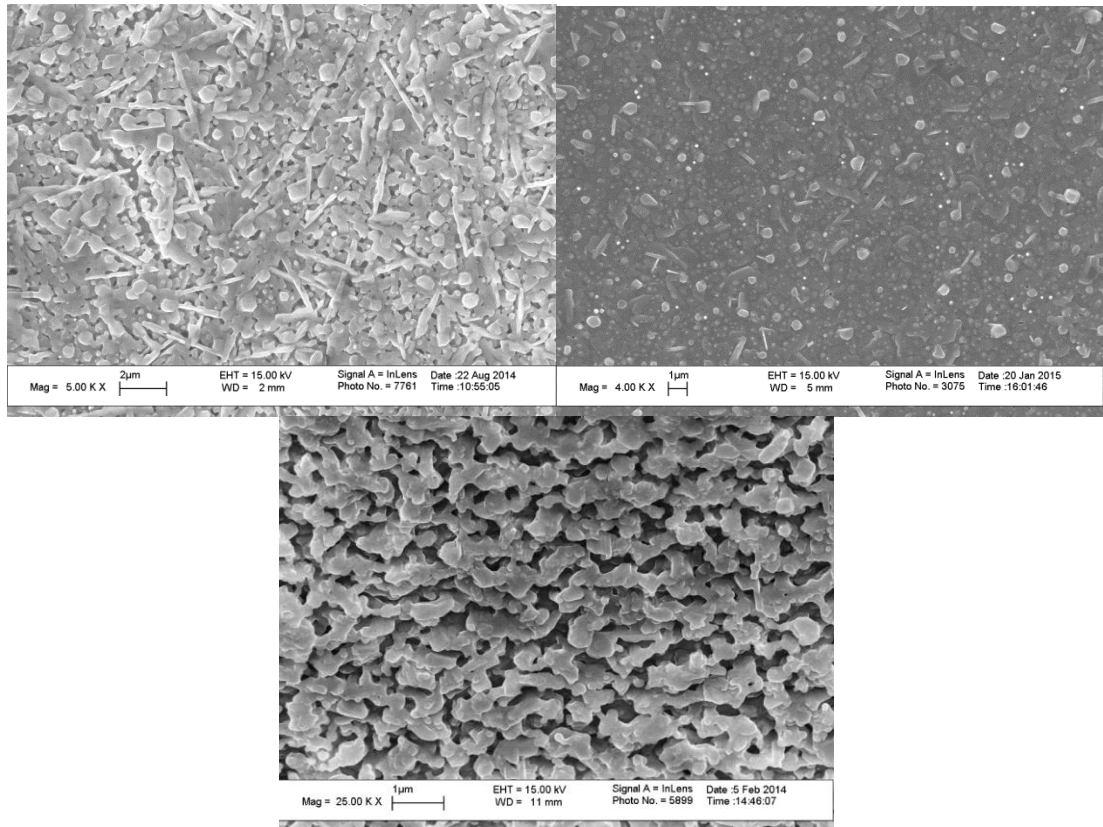


Figure 72: Results of varied humid condition durations of (top-left) 210 min, (top-right) 150 min, and (bottom) 90 min in crystallization of MOD films in MOD 1 at a 750 °C crystallization temperature and 4.2% relative humidity.

As seen in Figure 72, the MOD microstructure showed widespread proliferation of a/b-axis grains. In the optimized procedure, the moist gas switch was done right when the furnace was cooling down at 750 °C, resulting in a 150 min moist gas duration which is also the time length of the primary crystallization process. The MOD microstructures showed greatly reduced a/b-axis grains and well-grown c-axis grains. In shortened humidity duration, the moist gas switch was done 60 min prior to the furnace cool-down, resulting in a 90 min moist gas

duration. The SEM microstructure images showed incomplete YBCO formation due to insufficient water vapor for the quasi-liquid interface.

3.7.3.5 Sample Size

Samples were also shortened to squares in order to create more uniform YBCO thin films from the TFA-MOD process, as seen in some high-performing MOD systems [43] [45]. As seen in Figure 73, the standard 4cm by 1.2cm samples suffered from massive non-uniformity in growth due to uneven solution dispersion when spin coating the precursor. Samples were cut in to 1.2 cm squares in order to better evenly spread the solution during spin coating. Scanning hall probe results below shows a vast improvement in thin film performance and uniformity, with I_c values greater than 25 A in certain regions.

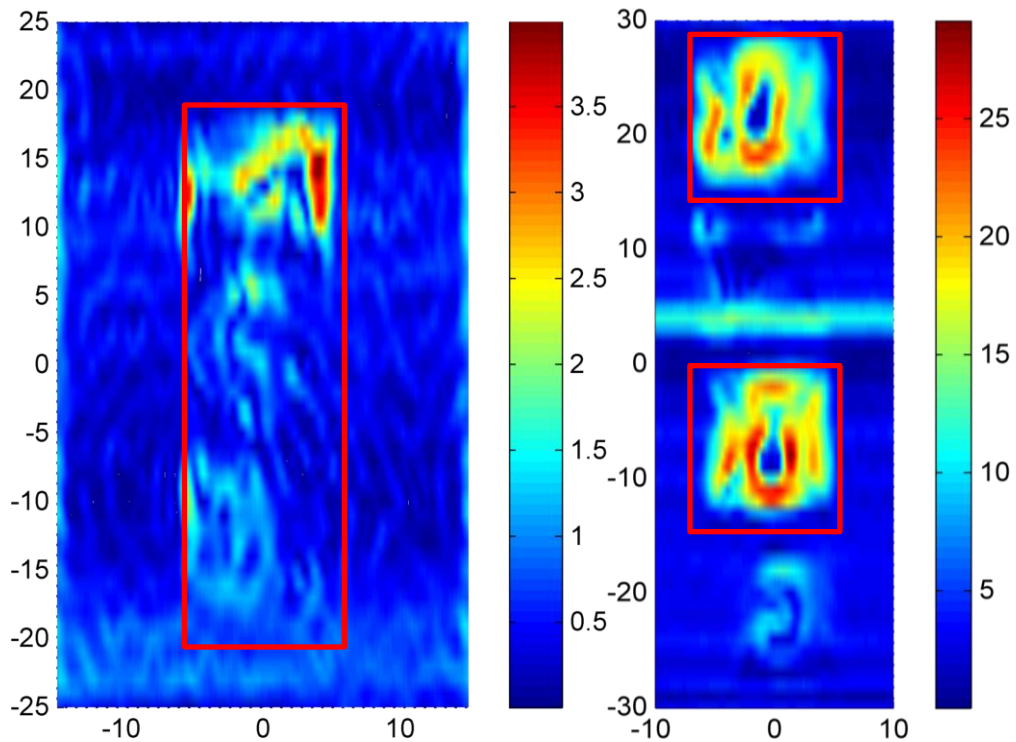


Figure 73: Scanning hall probe results showing the location of high performing superconducting material in (left) a 4 x 1.2 cm long sample and (right) 1.2 x 1.2 cm square samples.

3.8 Superconducting Properties of YBCO Films with Tin-Oxide Nanowires

3.8.1 TFA-MOD Films Embedded with Nanowires

Tin-oxide nanowire samples were cut into 1.2 by 1.2 cm squares and deposited with YBCO thin films through the TFA-MOD process. Moderately dense samples (approximately 30% effective nanowire density) were the first batch used for YBCO deposition. Figure 74 shows the nanowires embedded in the calcinated and crystallized YBCO thin film. The presence of the nanowires is easily seen in the transparent calcinated film, and within the gaps in the cracked film. However, after crystallization, only glimpses of the nanowires can most often be seen in the gaps of cracked films.

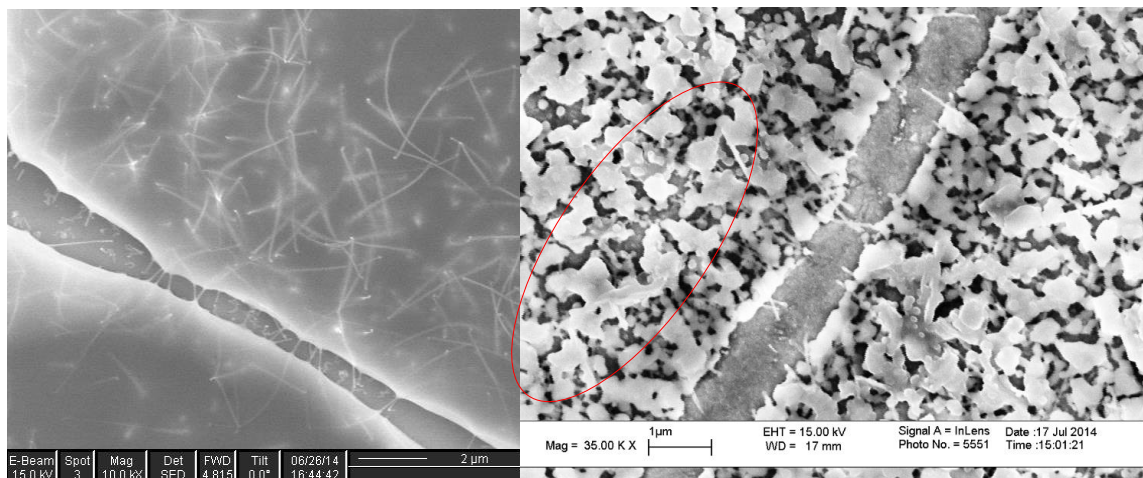


Figure 74: SEM microstructure of (left) calcinated thin film with visible embedded nanowires and (right) crystallized film with visible NWs in the gaps

Nevertheless, as seen in Figure 75, YBCO growth on the moderately dense nanowire samples proved to be ineffective. The T_c data showed broad or no clear transitions above 77K. The integrated GADDS results show no proper YBCO growth except for the (003) peak. There is also formation of secondary phases such as amorphous Ba-O-F clusters and an abundance CuO nanoparticles.

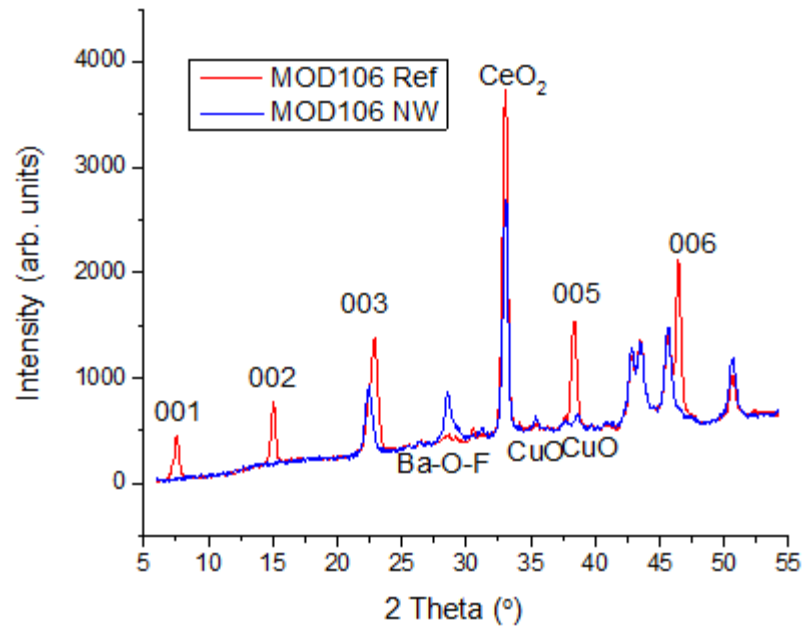


Figure 75: Integrated GADDs results revealing poor YBCO growth on moderately dense nanowire samples in the TFA-MOD process

In order to allow for proper YBCO thin film growth, lower density nanowire samples (10% to 15%) were used for deposition. As seen in Figure 76, these samples were far more successful in the formation of YBCO thin films, as well as, achieving near-reference T_c values. Similar results are seen in the transport I_c measurements where the nanowire-embedded samples exhibited relatively high current values compared to the reference. This is especially true in the MOD 118 sample which showed a critical current of nearly 13 A compared to 14 A of the reference. MOD 114 and 118 were processed in MOD 2 under a 755 °C crystallization temperature for 150 min at a relative humidity of 9.2%. However, MOD 114 had a slightly higher nanowire density of approximately 15%, compared to 10% on MOD118, which likely resulted in the lowered I_c performance in MOD 114.

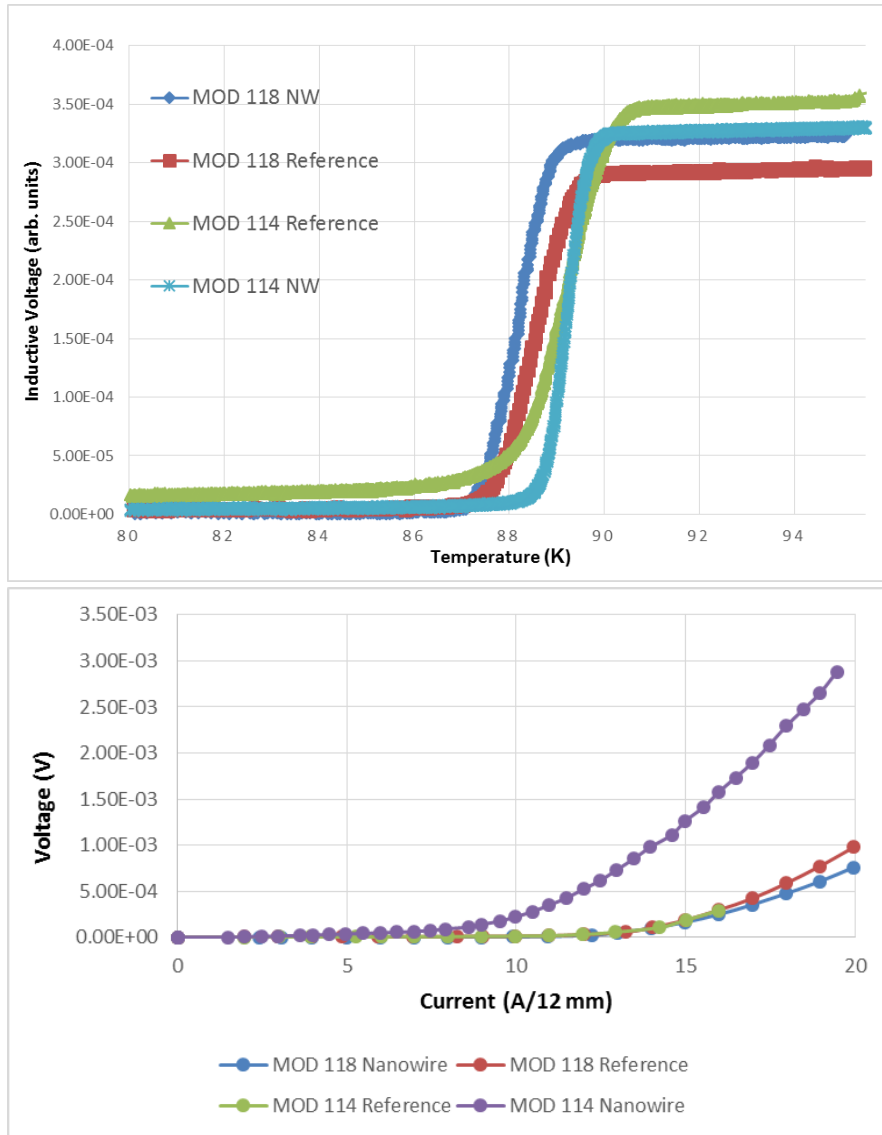


Figure 76: TFA-MOD nanowire embedded YBCO thin film samples compared to reference sample in (top) T_c and (bottom) I_c measurements

The higher current carrying sample was tested in magnetic fields up to 3.5 T at 77K and 65K. Figure 77 show the results from angular and field dependence measurements of critical current in various fields at 77K. In the angular dependence measurement, it is apparent the tin-oxide nanowire-embedded sample had lower I_c performance than the reference with no I_c increase at the $B \parallel c$ field direction (along the nanowire direction) at 1 T. However, at 3 T, the I_c values of the nanowire sample was comparable with that of the reference sample indicating the

pinning in the nanowire sample is more effective at the higher field. In the field dependence measurement, the reference sample showed overall better I_c performance compared to the nanowire sample at low fields.

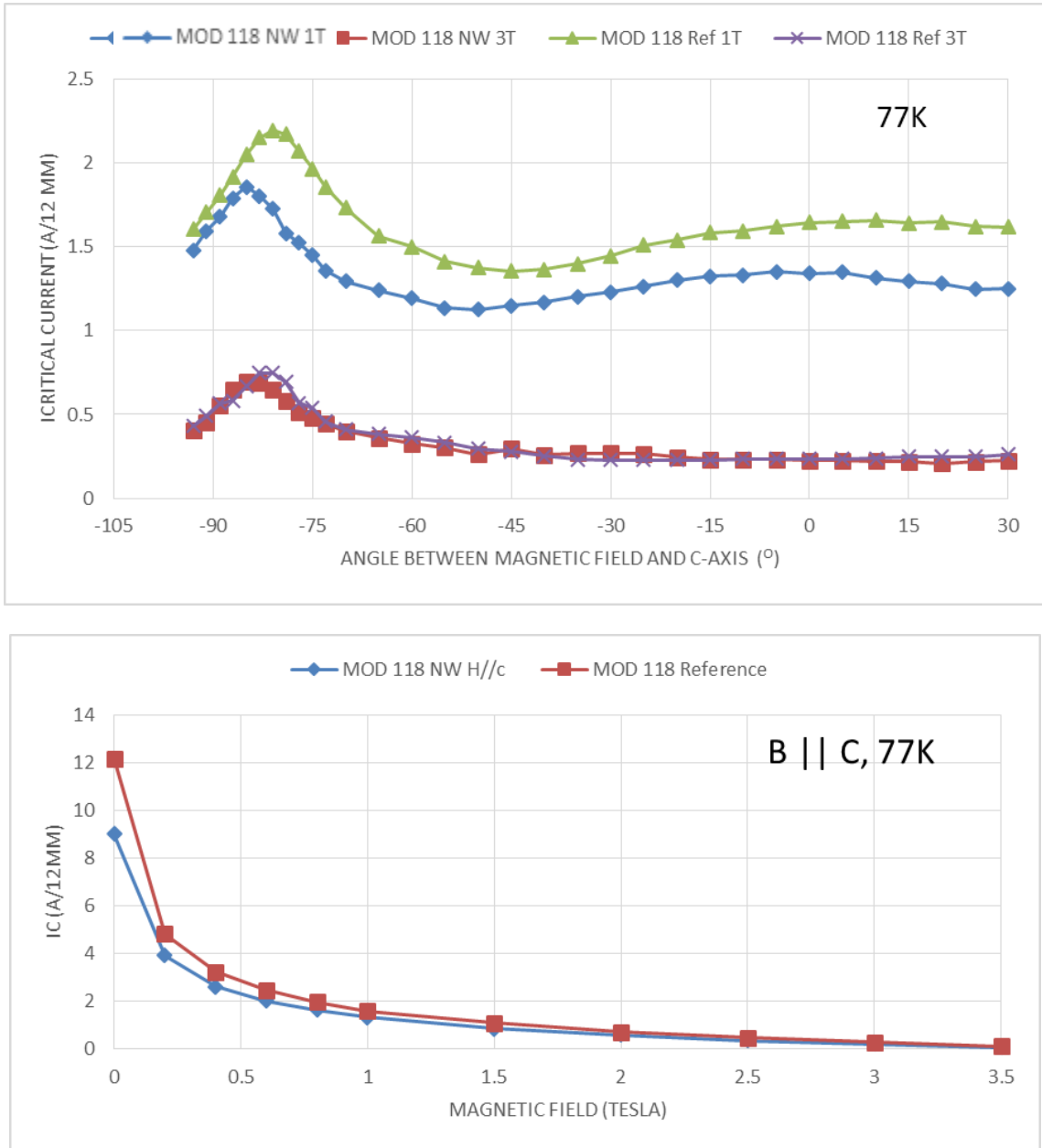


Figure 77: Angular dependence of I_c at 77K of NW and references samples at 1 and 3T (top) and magnetic field dependence of I_c at 77K along the c-axis of NW and references samples (bottom)

The samples were tested at 65K and the results are shown in Figures 78 and 79. In the angular dependence measurement, the critical current of the nanowire-embedded sample at 3 T is higher than that of the reference sample even though the reverse is true at 1 T. Hence, it appears that the pinning in the nanowire sample is more effective at higher fields. In the field dependence measurements at 65K, it is seen that the critical currents of the TFA-MOD reference and nanowire samples were able to reach 25A and 20A, respectively at zero field. At low fields, the critical current of the nanowire sample is lower. Nevertheless, at the higher fields, the nanowire sample is able to match the performance of the reference.

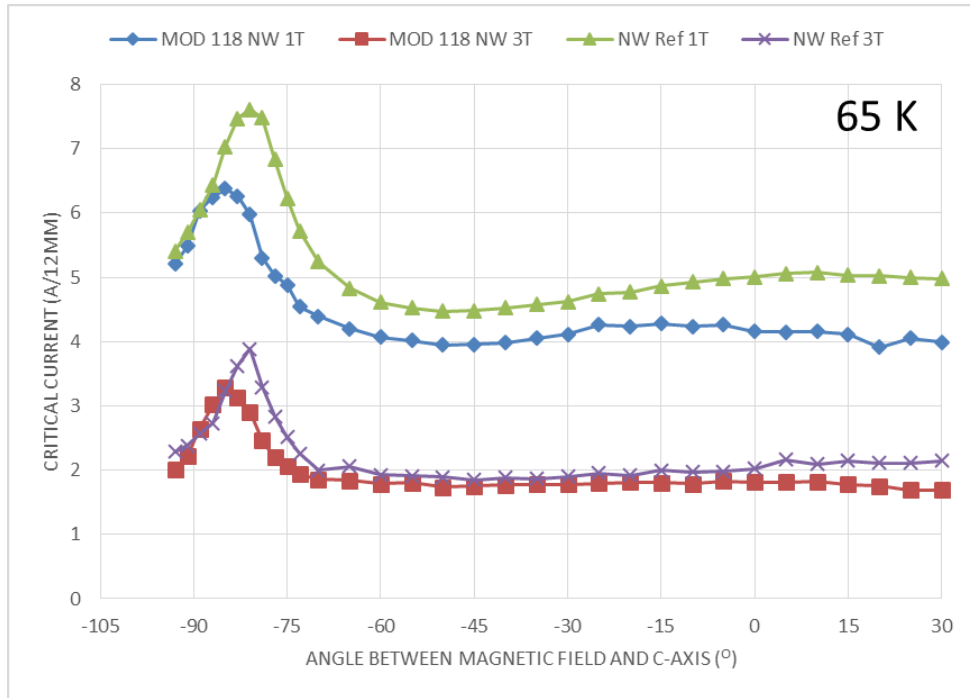


Figure 78: Angular dependence of I_c at 65K of NW and reference samples at 1 and 3 T

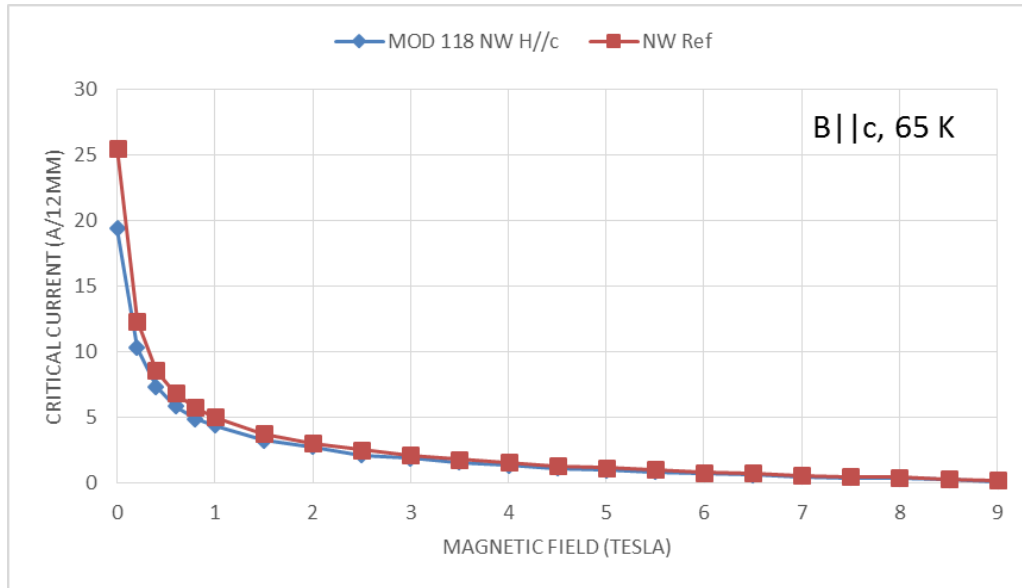


Figure 79: Magnetic field dependence of I_c along the c-axis of NW and reference samples at 65K

3.8.2 MOCVD Films Embedded with Nanowires

YBCO film was also deposited using an MOCVD system on the CeO_2 buffers with nanowires. Our current MOCVD system compared to the MOD system is far more developed, thus making it more feasible in achieving high performing samples. Prior to deposition, these samples were spot welded together on to leader tapes with side-strips and then wound in spools. The spooled samples were used for YBCO deposition inside a cold-walled reel-to-reel MOCVD system.

Initially, the bare CeO_2 buffer tapes required optimization for proper YBCO growth. Previous work on CeO_2 on our MOCVD system yielded reference samples with low critical currents (I_c). Figure 80 shows the optimization results for critical temperature measurements.

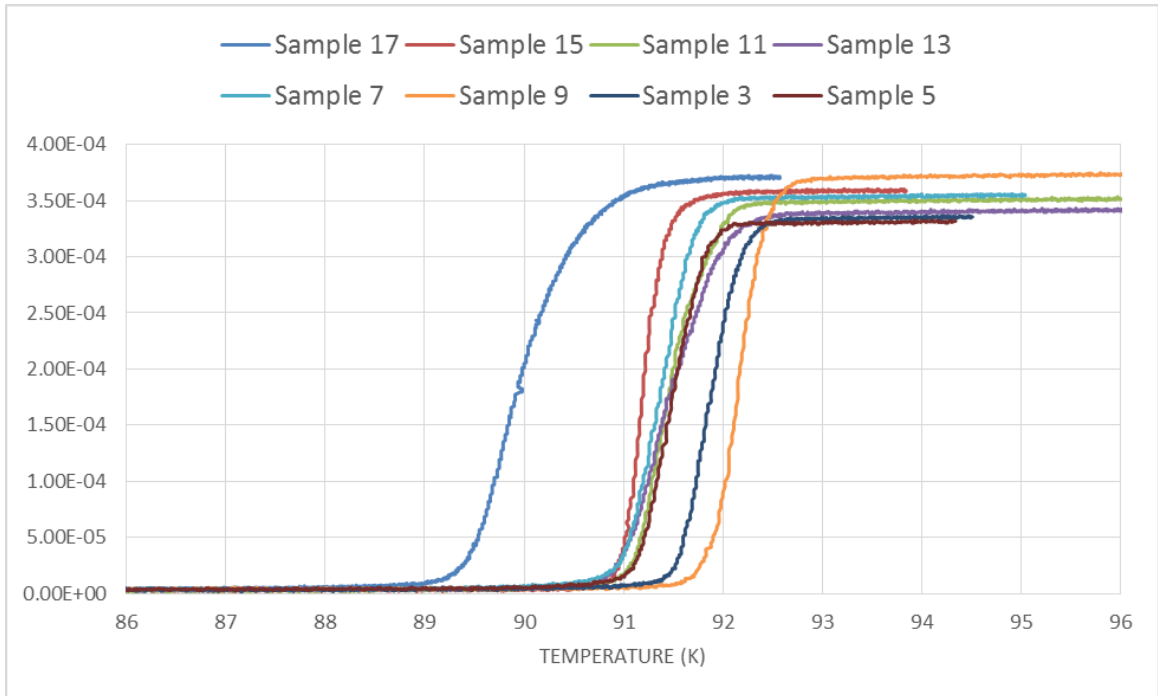


Figure 80: T_c optimization for bare CeO_2 buffers prior to nanowire testing

Our initial nanowire samples deposited with YBCO in MOCVD measured at 30% effective nanowire density. The moderately-dense samples resulted in poor performance due to degraded YBCO growth. Figure 81 shows an example GADDS result from the initial runs. The GADDS results revealed degradation in epitaxial YBCO growth in the nanowire sample, while the reference showed expected growth performance. The outcome of the degradation is indicated in Figure 81 where critical temperature measurements showed poor performance, as seen by the wide T_c transitions in the nanowire samples. The critical current values in these moderately dense nanowire samples were around 1 to 2 A.

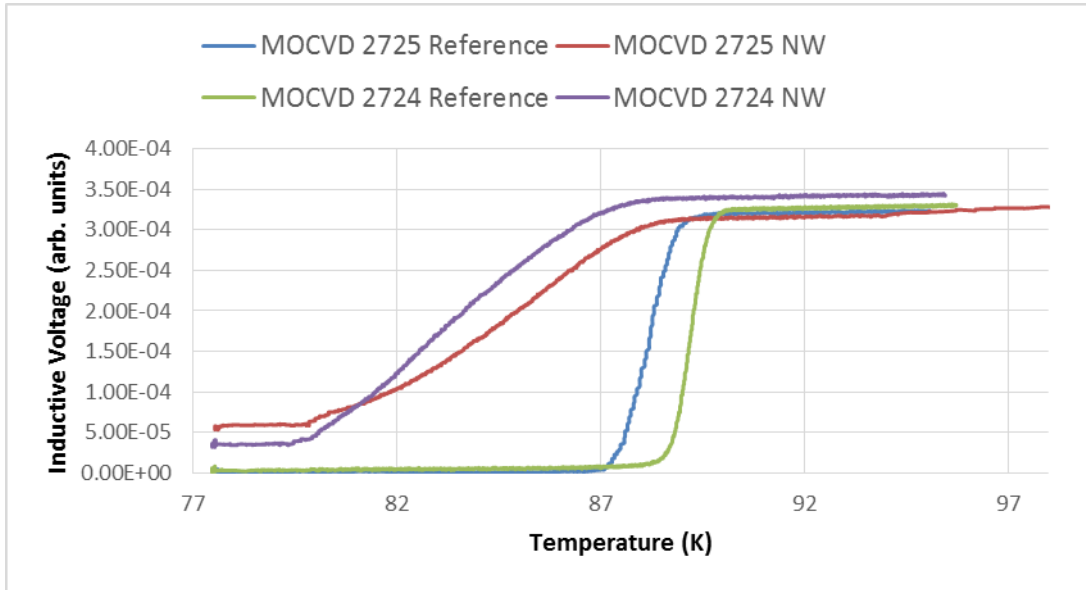
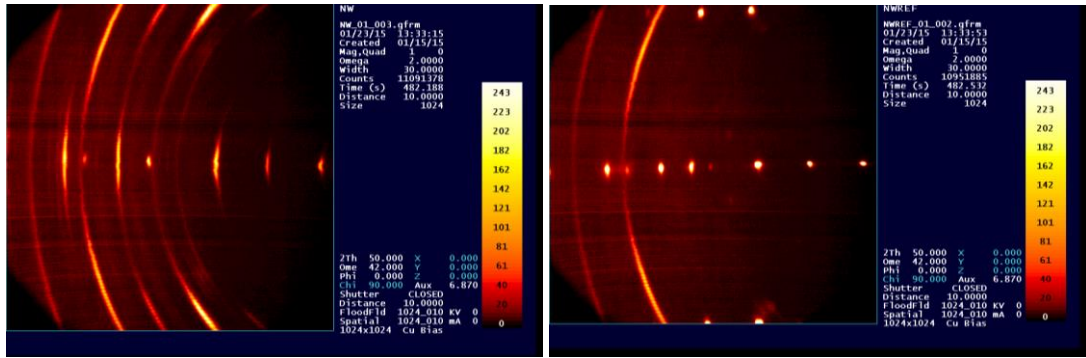


Figure 81: (Top) GADDS and (bottom) T_c results for moderately dense nanowires samples made by MOCVD compared to the reference indicating degradation in epitaxial YBCO

The effective nanowire density was reduced to 10% to 15% in subsequent nanowire samples in order to eliminate degradation in epitaxial superconductor growth. Figure 82 shows the favorable T_c and I_c data. The reduction in nanowire density by half has a dramatic effect on YBCO performance. The T_c measurements revealed sharp superconducting transitions, and the I_c measurements showed acceptable current carrying performance for the first time. Sample MOCVD 2727 NW showed exceptional performance with a transition at 90K and an I_c of 140 A. The MOCVD samples had a thickness of 1.1 μm , and were made using a precursor of composition $\text{Y}_{0.6}\text{Gd}_{0.6}\text{Ba}_2\text{Cu}_{2.3}$.

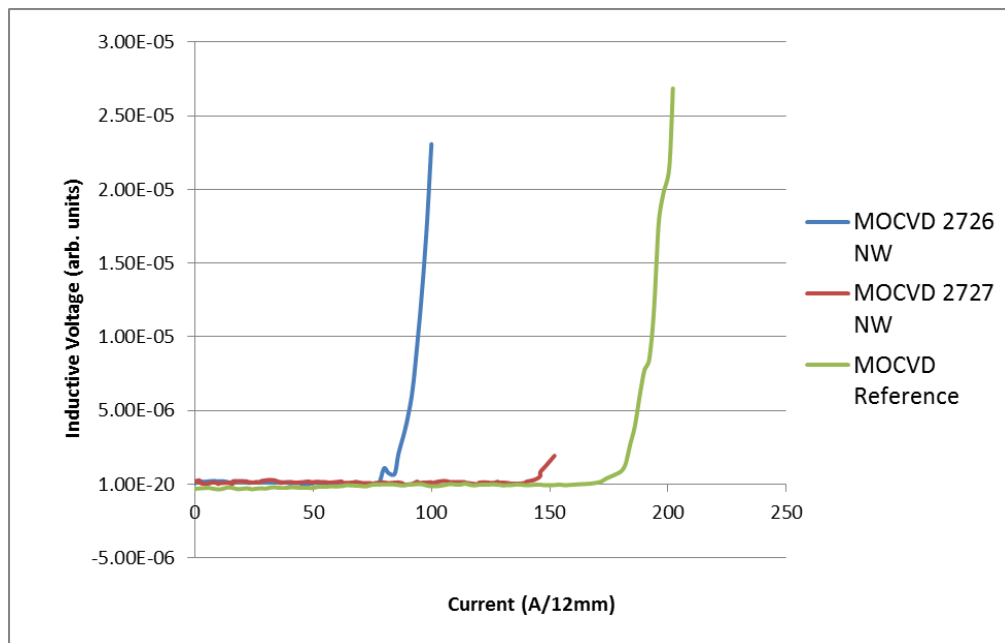
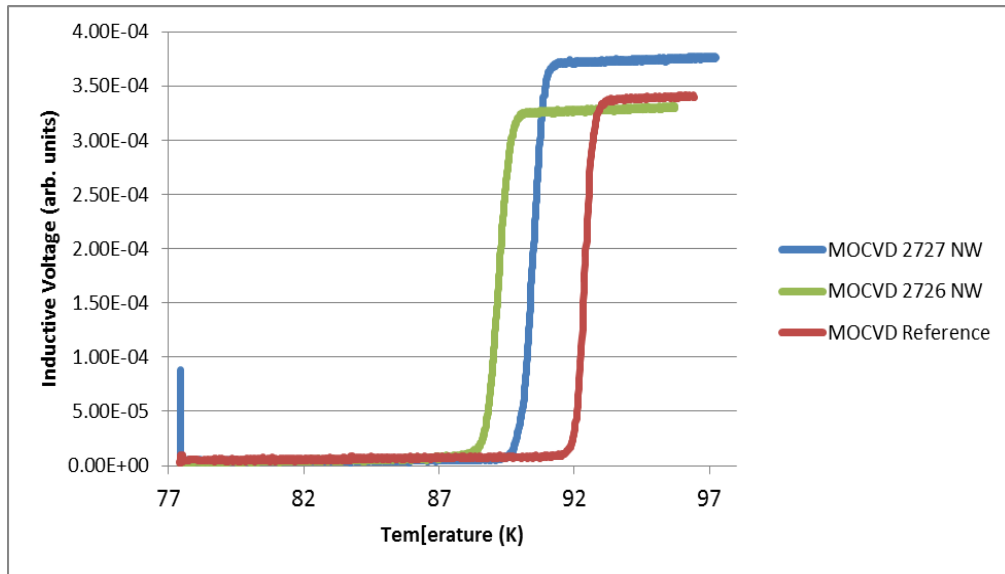


Figure 82: T_c and I_c results from low density nanowire samples made MOCVD compared to the

In-field testing was performed at 77K and 65K on bridged nanowire-embedded samples. Figure 83 shows the angular and field dependence of I_c of the MOCVD 2727 NW sample and reference at 77K. At 1 T, the nanowire-embedded sample showed impressive critical current in the $H||c$ field direction, which outperformed the reference sample. The nanowire-based sample again outperformed the reference sample at 3T, though at a lower magnitude. The field

dependence plot shows that the nanowire-based sample provided stronger pinning at nearly all fields up to 5T at 77K indicating the nanowires are effective.

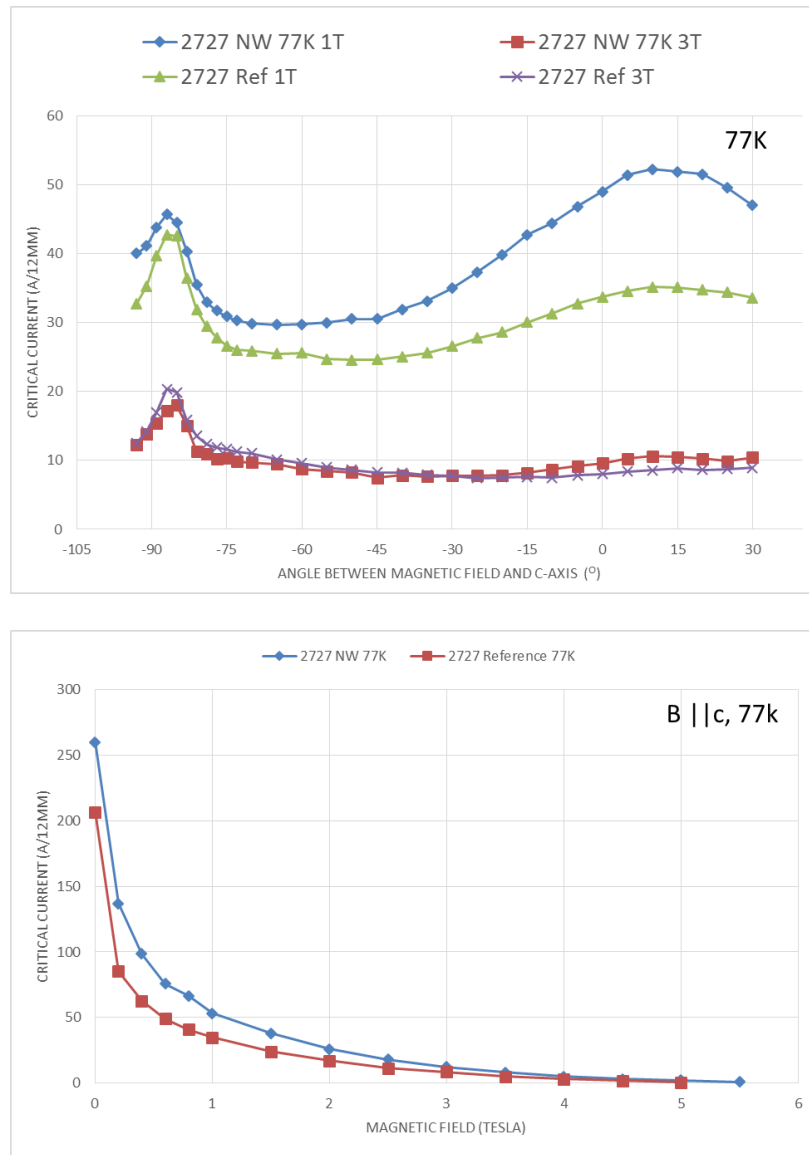


Figure 83: Angular and field dependence measurements from nanowire and references samples at 77K

Figure 84 shows the angular and field dependence of I_c of MOCVD 2727 and reference samples at 65K. As in the 77K measurements, the nanowire-embedded sample again outperforms the reference sample at $B || c$ field direction, indicating strong pinning potential. At 3T and 65K, the nanowire based sample shows impressive I_c performance with higher current

magnitudes when compared to the 77K, 3T measurements. The $B \parallel c$ field dependence at 65K shows the MOCVD 2727 nanowire sample outperforming the reference sample at all fields up to 7T.

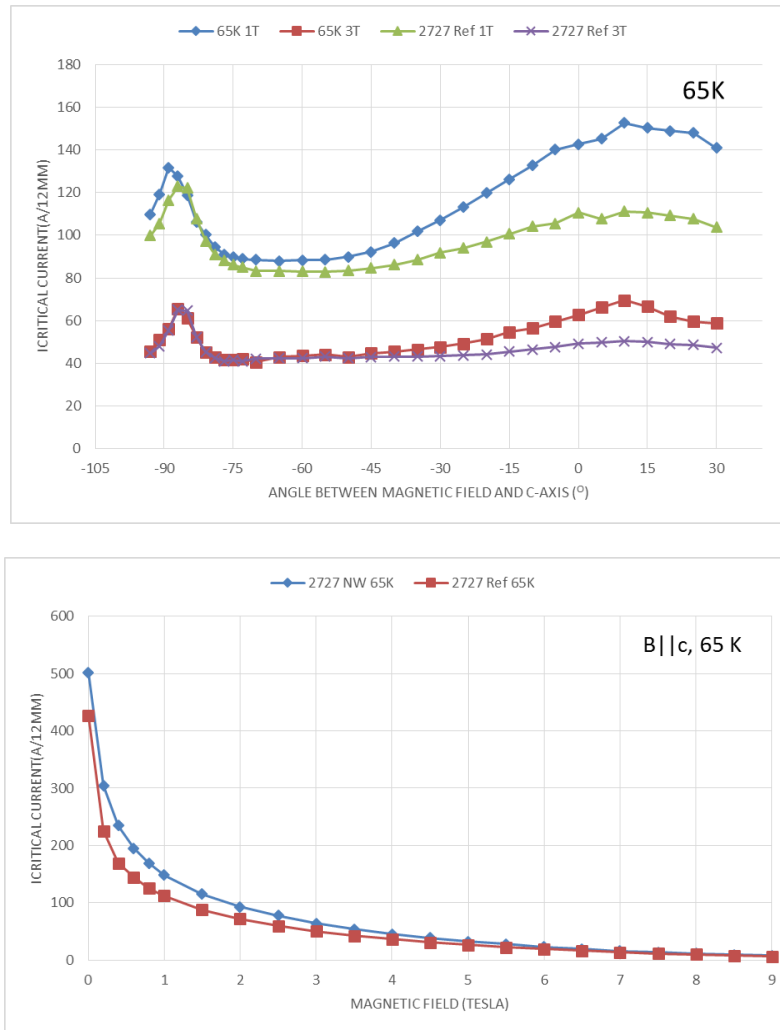


Figure 84: Angular and field dependence measurements from nanowire and reference samples at 65K

Chapter 4: Summary and Future Work

4.1 Summary

Metal-oxide nanowires have enjoyed a rich variety of applications since their inception, especially in gas sensing and semiconductor industries. Our work involved creating a novel application for use of nanowires in 2nd generation high temperature superconducting tapes. Prior research in 2G HTS materials capitalized on the self-assembly of various types of nanorods during superconducting to improve critical current densities in high magnetic fields. However, the self-assembled morphologies proved difficult to control and distribute. In this thesis, we explored the pre-fabrication of SnO₂ nanowires on CeO₂ buffer tapes by VLS growth mechanism that allowed for meticulous control of its density, distribution and overall morphology. Additionally, TFA-based MOD deposition was explored in order to deposit YBCO superconducting thin films on the buffers with pre-fabricated nanowires to study their effects on flux pinning.

The SnO₂ nanowires were successfully synthesized primarily on CeO₂ buffered tapes using VLS mechanism in a CVD system. The catalyst seeding mainly involved Au colloids and alternatively, sputter-coated Au/Pd nanoparticles. In colloidal samples, initial process conditions resulted in growth of nanowires on the buffer tape, but lacked proper uniformity and repeatability. The nanowire arrays also included various degrees of defects including in-plane nanowires, conglomeration of nanowires, excess tin powders and overall lack of growth reliability. Reduction in in-plane nanowires was critical for this work since their presence can obstruct the deposition of superconducting film on the buffer surface. Thus, several growth factors were investigated including substrate annealing, growth temperature, carrier gas flow, and system pressure in order improve the nanomaterial array.

Investigations resulted in optimized process conditions that allowed for significantly reduced surface defects such as in-plane nanowires, as well as vastly improved SnO₂ nanomaterial uniformity and repeatability. In the optimized conditions, the stirred colloidal solution was seeded on the substrate surface and annealed to melt and re-form conglomerated nanoparticles into large radii colloids. The annealed substrate was air quenched after 30 min resulting in a massive reduction in in-plane nanowires. This resulted in a higher density of preferential vertical nanowire growth too. The samples were grown under 630 °C and 0.50 Torr for 20 min, resulting in a field of 1 μm long out-of-plane nanowires.

A reverse carrier gas flow direction was used during growth to homogenize the incoming evaporated Sn vapor leading to improved uniformity of nanowire densities along the length of the sample. In sputter-coated samples, the sputter coating pressure and duration was varied in order to alter the morphology of the Au/Pd nanocatalysts. Lowering the coating pressure to 60 mTorr for a 2 s coating time resulted in unique 10 nm thick and 200 nm tall nanowires that was typically too challenging to re-create in colloid-based nanowires. Optimized growth conditions led to highly repeatable and controllable nanowire morphologies. The optimal growth conditions allowed for highly uniform growths, showing a maximum deviation of 2.8% in the nanowire densities along the substrate surface.

Ion bombardment was also explored in order to align mis-aligned nanowires as well as to eliminate any in-plane defects. However, all levels of ion bombardment resulted in damage to the buffer layer making it undesirable for thin film deposition. The ion bombarded samples did show unique morphologies including 'root-like' colloidal nanowires and fields of thick sputter coated NWs.

In addition to CVD nanowire growth, synthesis of superconducting thin films was also investigated. The standard Araki model for TFA-based MOD was used to create YBCO thin films

on the bare buffer surfaces, as well as, buffers with prefabricated nanowires. Certain process optimizations were also performed in order to improve the YBCO thin film performance. The standard precursor ratio of Y, Ba, Cu hydrated acetates was reduced from 1:2:3 to 1:1.8:3 leading to higher-performing thin films due to a reduction in secondary phases caused by excess barium. Methanol content was also investigated to reduce the chance of film cracking due to highly viscous coating solutions. Optimization of crystallization temperature at 755 °C resulted in reliable J_c values of approximately 0.5 MA/cm² in the 200 nm thick samples. The crystallization time was also reduced to 150 min, leading to a dramatic improvement in YBCO microstructure as well as a reduction in misoriented a/b-axis grains. With a relative humidity of 9-12% and 3-4% in MOD 2 and MOD 1 respectively, crack-free YBCO thin films were fabricated. Additionally, setting the humidity gas duration to 150 min (the duration of crystallization) resulted in a marked reduction in a/b-axis grains and porosities in the microstructure.

The TFA-MOD samples showed clear indications of nanowires embedded in the YBCO film. However, moderately dense nanowire-embedded depositions showed poor YBCO peaks and non-epitaxial growth. Low density samples (10-15%) were created in order to allow for proper YBCO deposition. The low density nanowire-embedded YBCO films resulted in I_c values of 13-14 A, which was only 1-2 A lower than those of the reference tape. However, no improvement in in-field performance was observed in the nanowire-embedded samples. Higher performing YBCO thin films might be required in order to discern the potential of nanowires in flux pinning. Low critical currents were observed in MOCVD samples also with moderately dense nanowire-based buffers. Samples with a low density of nanowires deposited with YBCO yielded I_c values up to 140 A, whereas the reference samples reached approximately 170 A. In angular and field dependence measurements at both 77K and 65K, the nanowire-embedded sample showed 50% higher I_c values relative to the reference, at the B || c orientation. At the same

orientation, the nanowire-embedded sample had enhanced I_c values at all magnetic fields up to 7.5 T. These results strongly indicate improved flux pinning by the nanowire-embedded YBCO thin film.

4.2 Future Work

With recent results indicating strong flux pinning potential in nanowire-embedded YBCO thin films, more focus will be placed on synthesizing films with various nanowire morphologies. Sufficient work has been completed on understanding the process and growth conditions that can create a wide range of SnO₂ nanowire morphologies. Further investigation into other types of nanowires including TiO₂ and indium-doped SnO₂ will be worth exploring as they are far more chemically stable than SnO₂ in harsh chemical environments [12] [1].

Additionally, more focus will be required for enhancing the TFA-based MOD thin films. As the TFA-MOD is a bottom-to-top growth mechanism for thin films, it has a significant potential to create better-performing nanowire-embedded YBCO tapes than MOCVD. Future work will focus on optimizing the calcination of the precursor solution in order to reduce CuO nanoparticle density and to reach J_c values of 1 MA/cm². Furthermore, in order to create more uniform films, investigation of dip-coating techniques will be beneficial, since spin-coated films tend to suffer from high levels of non-uniformity. Films coated in multiple layers will also be useful in reaching a J_c performance of 1 MA/cm². In regards to MOCVD films, process conditions will need to be optimized in order to deposit epitaxial YBCO on higher density nanowire substrates.

References

1. A. Crisan, V.S. Dang a, G. Yearwood, P. Mikheenko, H. Huhtinen, P. Paturi C.
"Investigation of the bulk pinning force in YBCO superconducting films." *Physica C* (2014).
2. A. Ichinose , H.Kai b, M.Mukaida, S.Horii, R.Kita d, K.Matsumoto, Y.Yoshida.
"Growth mechanism of nanorods in REBCO films ." *Journal of Crystal Growths* 312 (2010): 2914-2918.
3. A. Sreekumaran Nair, Zhu Peining, V. Jagadeesh Babu, Yang Shengyuan.
"Anisotropic TiO₂ nanomaterials in dye-sensitized solar cells." *Physcial Chemistry* 13 (2011): 21248-21261.
4. A.M. Morales, C.M. Lieber. *Science* (1998): 208.
5. AGoyal, S. Kang, K J Leonard, PMMartin, A. Gapud,. "Irradiation-free, columnar defects compromised of self-assembled nanodots and nanorods resulting in strongly enhanced flux-pinning in YBCO films." *Superconductors Science Technology* 18 (2005): 1533-1538.
6. Alexandra Tischner, Anton Köck, Thomas Maier, Christian Edtmaier. "Tin Oxide Nanocrystalline films and nanowires for chemical sensors." *Microelectronic Engineering* 86 (2009): 158-1261.

7. Ayan Kar, Michael A Stroschio, Mitra Dutta, Jyoti Kumari. "Growth and properties of tin oxide nanowires and the effect of annealing conditions." *Semiconductor Science Technology* 25 (2010): 1-9.
8. Aytug, T. "Enhanced flux pinning in mocvd-ybco films through zr additions: systematic feasibility." *Superconductor science and technology* (2010).
9. Dadras, S. "Increase of critical current density with doping carbon nanotubes in YBCO." *Physica C* 469.1 (2009): 55-59.
10. Dinga, Hongwei Gua, Teng Zhanga, Hongyan Wanga, Fei Qua. "Strong enhancement flux pinning in Mod-YBCO films with self-assembled BaTiO₃ nanocolumns." *Applied Surface Science* 314 (2014): 622-627.
11. Elena. Shevchenko, Dmitri Talapin, Christopher Murray, Stephen Obrien. "Structural Characterization of Self-Assembled Multifunctional Binary Nanoparticle Superlattices." *Journal of American Chemical Society* 128.11 (2006): 3620-3637.
12. Elisabetta Comini, Camilla Baratto, Isabella Concina, Guido Faglia, Matteo Falasconi, Matteo Ferroni, Vardan Galstyan, Emanuela Gobbi, Andrea Ponzoni, Alberto Vomiero, Dario Zappa, Veronica Sberveglieri, Giorgio Sberveglie. "Metal Oxide Nanosciences for Chemical Sensors." *Sensors and Actuators B: Chemical* 179 (2013): 3-20.

13. F. Shao, J. Sun, L. Gao, S. Yang and J. Luo. *Journal of Physical Chemistry* 1819 (2011): 115.
14. Foltyn, S.R., L. Civale, J.L. Macmanus-Driscoll, Q.X. Jia, B. Maiorov, H. Wang, and M. Maley. "Materials science challenges for high-temperature superconducting wire." *Nature Materials* 6.9 (2007): 631-642.
15. Funda Aksoy Akgul, Gumus, Ali O. Er, Ashraf H. Farha, Guvenc Akgul. "Structural and electronic properties of SnO₂." *Journal of Alloys and Compounds* 579 (2013): 50-56.
16. G. K. Mor, O. K. Varghese, M. Palouse, K. Shankar and C.A. Grimes. *Solar Energy Materials and Solar Cells* 2011 (2006): 90.
17. Goyal, C. Cantoni and A. *Nanotechnologies to enable high-performance superconductors*. Oak Ridge, Tennessee, 2008.
18. Hirabayashi, Takeshi Araki and Izumi. "Review of a chemical approach to YBa₂Cu₃O_{7-x} coated superconductors-metal organic deposition using trifluoroacetates." 16 (2003).
19. M. Araki. "Review of a chemical approach to YBa₂Cu₃O_{7-x} -coated superconductors—metalorganic deposition using trifluoroacetates." *Superconductor Science Technology* 16 (2003): 71-94.
20. Howe, Saka. *Materials Research Society Bulletin* 29 (2004): 951.

21. Irene Gonzalez-Valls, Monica Lira-Cantu. "Vertically-aligned nanostructures of ZnO for excitonic solar cells: a review." *Energy and Environmental Science* 1 (2008): 19-34.
22. J. X. Wang, X. W. Sun , Y. Yang , H. Huang , Y. C. Lee , O. K. Tan ,. "Gas Responses to ZnO Based Sensors." *Nanotechnology* 17 (2006): 4995-4998.
23. Jeffrey B. Fortin, Toh-Ming Lu. *Chemical Vapor Deposition Polymerization: The Growth and Properties of Paralene Thin Films*. Kluwer Academic Publishers, 2004.
24. K.J. Song, R.K. Ko, Y.S. Lee a, J.S. Yang a, Y.M. Park, Manglesh Dixit, H.S. Kim. "The flux pinning enhancement of YBCO film prepared by PLD using composite targets doped with BZO nanopowders." *Physica C* (2005): 656-659.
25. Luping Lia, Shikai Chena, Jung Kima, Cheng Xua, Yang Zhaoa, Kirk J. Ziegler. "Controlled synthesis of tin-doped indium oxide (ITO) nanowires." *Journal of Crystal Growth* Volume 413 (2014): 31-36.
26. M Haruta, T Fujiyoshi, T Sueyoshi, K Dezaki, D Ichigosaki. "Flux pinning properties of ErBa₂Cu₃O_y thin films with BZO nanorods." *Superconductor Science Technologies* 19 (2006): 803-807.
27. M. Zacharias, J. Heitmann, R. Scholz, U. Kahler, M. Schmidt, J. Blasing. *Applied Physics Letter* 80 (2002): 661.

28. M.K. BenSalema, n, E.Hannachia, Y.Slimania, A.Hamritaa, M.Zouaouia, L.Bessaisb. "SiO₂ nanoparticles addition effect on microstructure and pinning properties in YBCO." *Ceramics International* 40 (2014): 4953-4962.
29. Martin W. Rupich, Darren T.Verebelyi. "Metalorganic deposition of YBCO films for second-generation high temperature superconductors." *MRS Bulletin* (2004).
30. Matt Law, Joshua Goldberger, Peidong Yang. "Semiconductor Nanowires and Nanotubes." *Annual Review Material Research* (2004): 83-122.
31. Matt Law, Lori Green, Justin Johnson, Richard Saykally. *Nanowire dye-sensitized solar cells*. Berkley, California: Department of Chemistry, University of California, Berkeley, 2005.
32. Matthias Batzill, Ulrike Diebold. "The Surface and Materials Science of tin oxide." *Progress in Surface Science* 79 (2005): 47-154.
33. N.Wang, Y.F. Zhang, Y.H. Tang, C.S. Lee, S.T. Lee. *Applied Physics Letter* 73 (1998): 3902.
34. Ozaki, Yoshida, Ichino, Takai, Ichinose, Matsumoto, Horii, Makaida, Takano. "Flux pinning properties and microstructure of SmBaCuO thin films with systematically controlled BZO nanorods." *Journal of Applied Physics* 108 (2010).
35. Park, Jong-Hee. *Chemical Vapor Deposition*. Materials Park, OH: The Materials Information Society, n.d.

36. Pierson, Hugh O. *Handbook of Chemical Vapor Deposition: Principles, Technology, and Applications*. Albuquerque, NM : Noyes Publications, n.d.
37. Q. Kuang, C. S. Lao , Z. L. Wang , Z. X. Xie , L. S. Zheng. *Journal for the American Chemical Society* 129 (2007): 6070-6071.
38. Ramgir, Datta, Kaur, Debnath, Aswal, Gupta. *Nanowires: Properties, Synthesis, and Applications*. Mumbai, India: Nova Science Publishers, 2012.
39. Rupesh Devan, Ranjit Patil, Jin-Han Lin, Yuan-Ron Ma. "One-Dimensional Metal-Oxide Nanostructures: Recent Developments in Synthesis, Characterization, and Applications." *Advanced Functional Materials* 22 (212): 3326-3370.
40. S. H. Park, S. H. Kim , S. W. Han. *Nanotechnology* (2007): 18.
41. S. Kang, A. Goyal, J. Li, P. Martin, A. Ijaduola, J.R. Thompson, M. Paranthaman. "Flux-pinning characteristics as a function of density of columnar defects compromised of self-assembled nanodots and nanorods in epitaxial YBCO films for coated conductor applications." *Physica C* 457 (2007): 41-46.
42. S. Xu, C. Xu , Y. Liu , Y. F. Hu , R. S. Yang , Q. Yang , J. H. Ryou, H. J. Kim , Z. Lochner, S. Choi , R. Dupuis , Z. L. Wang. "Ordered Nanowire Array Blue/Near-UV Light." *Advanced Materials* 22 (2010): 4749 – 4753.
43. Seung-Yi Lee a, Seul-A Song a, Byeong-Joo Kim a, Jin-A Park a, Ho-Jin Kim a,. "Effect of precursor composition on Jc enhancement of YBCO." (2006).

44. Soumyadeep Misra, Linwei Yu, Martin Foldyna, Pere Rocai Cabarrocas. "High efficiency and stable hydrogenated amorphous silicon radial junction solar cells built on VLS-grown silicon nanowires." *Solar Energy Materials & Solar Cells* 118 (2013): 90-95.
45. T Puig, J C González, A Pomar, N Mestres, O Castano, M Coll. "The influence of growth conditions on the microstructure and critical currents of TFA-MOD on YBCO films." 18 (2005).
46. T. Honjo, Y. Nakamura, R. Teranishi, Y., Tokunaga. "Fabrication and growth mechanism of YBCO coated superconductors by TFA-MOD process." (2002).
47. Takeshi Araki, Haruhiko Kurosaki, Yutaka Yamada. "Coating Process for YBCO superconductor by metalorganic deposition method using trifluoroacetates." 14 (2001).
48. Tao, Xin. *Fabrication of Nanowires by Chemical Vapor Deposition for Flux Pinning in Superconducting Films*. Houston, TX: University of Houston, 2012.
49. Venkat Selvamanickam, Yimin Chen, Xuming Xiong, Yiyuan Y. Xie, Maxim Martchevski, Andrei Rar. "High Performance 2G Wires: From R&D to Pilot-scale Manufacturing." *Applied Superconductivity* 19.3 (2009).
50. Wang, Cai, Zhang. "Growth of nanowires." *Reports* 60 (2008): 1-51.
51. Wei Lu, and Charles Lieber. "Semiconductor Nanowires." *Journal of Physics D: Applied Physics* 39 (2006): 387-406.

52. William S. Rees, Jr. *CVD of Nonmetals*. New York: VCH Publishers, 1996.
53. Xianping Chen, KY Wong, A. Yuan, Guoqi Zhang. "Nanowire Based Gas Sensors." *Sensors and Actuators B: Chemical* 177 (2013): 178-195.
54. Zhengdao Li, Yong Zhou, Ruzhong Sun, Yan Xiong, Haiquan Xie, Zhigang Zou. "Nanostructured SnO₂ photoanode-based dye sensitized solar cells." *China Science Bulletin* 59.12 (2014): 2122-2134.